

Chemical Structures and Performance of Perovskite Oxides

M. A. Peña and J. L. G. Fierro*

Instituto de Catalisis y Petroleoquímica, CSIC, Cantoblanco, 28049 Madrid, Spain

Received September 28, 2000

Contents

I. General Characteristics of Perovskites as Catalysts	1981
II. Structure of Perovskites	1982
A. Crystal Structure	1982
B. Nonstoichiometry in Perovskites	1983
1. Oxygen Nonstoichiometry	1983
2. Cation Nonstoichiometry	1984
C. Physical Properties	1985
D. Adsorption Properties	1986
1. CO and NO Adsorption	1986
2. Oxygen Adsorption	1987
E. Specific Surface and Porosity	1987
F. Thermal Stability in a Reducing Atmosphere	1989
III. Acid–Base and Redox Properties	1990
A. Acidity and Basicity	1990
B. Redox Processes	1991
1. Kinetics and Mechanisms	1992
2. Reduction–Oxidation Cycles	1993
C. Ion Mobility	1993
1. Oxygen Transport	1993
2. Cation Transport	1994
IV. Heterogeneous Catalysis	1995
A. Oxidation Reactions	1995
1. CO Oxidation	1995
2. Oxidation of Hydrocarbons	1996
B. Pollution Abatement	2001
1. NO _x Decomposition	2001
2. Exhaust Treatment	2002
3. Stability	2004
C. Hydrogenation and Hydrogenolysis Reactions	2004
1. Hydrogenation of Carbon Oxides	2004
2. Hydrogenation and Hydrogenolysis Reactions	2006
D. Photocatalysis	2007
1. Photodecomposition of Water	2007
2. Other Photocatalytic Reactions	2009
E. Chemical Sensors	2009
F. Electrocatalysis	2010
1. Oxygen Reduction	2010
2. Solid Oxide Fuel Cells	2011
G. Structure–Activity Relationships	2012
V. Future Perspectives	2013

VI. Acknowledgment	2014
VII. References	2014

I. General Characteristics of Perovskites as Catalysts

The vast majority of catalysts used in modern chemical industry are based on mixed metal oxides. The preparation of specific tailor-made mixed oxides able to perform complex functions is one of the main topics of research in the field of heterogeneous catalysis. Achieving complex catalytic reactions requires a polyfunctional catalyst with appropriate solid state, surface, and morphological properties. The extensive background knowledge in solid state-surface chemistry carried out in the field of heterogeneous catalysis may be usefully applied in the design of catalyst and the engineering of new high performance materials. A wide cross-fertilization bridges heterogeneous catalysis and materials science in the fields of physicochemical characterization, solid-state chemistry, and routes of synthesis.^{1–3}

Among the mixed metal oxides, perovskite-type oxides remain prominent. The perovskite oxides have the general formula ABO₃ (A cation of larger size than B). Although the most numerous and most interesting compounds with the perovskite structure are oxides, some carbides, nitrides, halides, and hydrides also crystallize in this structure. This review will focus only on the study of oxides and their relevance in heterogeneous catalysis and surface chemistry. It will not cover physical properties such as the electric, magnetic, and optical properties of the perovskites. Comprehensive studies on these properties have been summarized in our previous book review.⁴ The broad diversity of properties that these compounds exhibit is derived from the fact that around 90% of the metallic natural elements of the Periodic Table are known to be stable in a perovskite-type oxide structure and also from the possibility of synthesizing multicomponent perovskites by partial substitution of cations in positions A and B, giving rise to substituted compounds with formula of

* To whom correspondence should be addressed. Fax: +34 91 585 4760. E-mail: jlgfierro@icp.csic.es.



Miguel A. Peña received his M.Sc. in chemistry in 1985 from the Complutense University of Madrid, Spain. He obtained his Ph.D. in chemistry in 1990 at the same university, working under the supervision of Dr. L. González Tejuca and Prof. J. L. G. Fierro at the Institute of Catalysis and Petrochemistry (CSIC). From 1990 to 1993, he was working under contract in a project of oxidative coupling of methane funded by REPSOL (the largest Spanish oil and petrochemistry company). At the end of this period, he got a staff position of researcher in the Institute of Catalysis and Petrochemistry, that is his current status. In 1996–1997, he was a Visiting Scholar in the group of Prof. A. Varma, at the University of Notre Dame (USA). He has been the Head of the Department of Structure and Reactivity of the Institute of Catalysis and Petrochemistry since 1998. His research interests are focused mainly in catalytic processes for clean energy production, specifically in catalytic applications of perovskite oxides (Ph.D. dissertation), natural gas conversion, catalytic combustion, C_1 chemistry, catalytic membrane reactors, hydrogen production, and fuel cell catalysts. He has published 30 papers and 3 patents and made 22 presentations at symposia and conferences.



Jose L. G. Fierro was born in 1948 in Leon, Spain. He received his Bachelor's degree in Chemistry at the University of Oviedo in 1973. Then he started his research on surface chemistry and catalysis at the Institute of Catalysis and Petrochemistry of the National Council of Scientific Research in Madrid in 1976. He has been studying heterogeneous catalysis and surface chemistry for over 27 years. His first appointment was a tenure scientist position at the Institute of Catalysis and Petrochemistry in 1978 and then research scientist and professor in 1985 and 1988, respectively. He spent two years from 1981 as a postdoctorate with Prof. J. Cunningham at University College Cork in Ireland, and then with Prof. B. Delmon at the Université Catholique de Louvain in Belgium. His research interests are natural gas conversion, catalytic combustion, petrochemistry, oil upgrading, C_1 chemistry, hydrogen production, surface chemistry and design of metal oxides for catalytic purposes. He is coordinator of Science and Chemistry Technology and member of the Scientific Committee Board of the National Council of Scientific Research. He has published 440 papers and 10 patents and made 130 presentations at symposia and conferences.

$A_{1-x}A'_x B_{1-x}B'_x O_3$. These characteristics account for the large variety of reactions in which they are used as catalysts. Other important aspects of perovskites

are related to the stability of mixed oxidation states or unusual oxidation states in the crystal structure. This is illustrated by the discovery of a metallic Cu^{2+} - Cu^{3+} mixed valence La-Ba-Cu oxide, which greatly favored the development of perovskites showing high-temperature superconductivity.⁵ Besides this, because of their controllable physical and chemical properties these isomorphous compounds offer excellent models for chemists not only for catalytic reactions but also for establishing correlations between reactivity and surface and/or bulk properties.

In this review, we have attempted to avoid overlapping with our previous review,⁴ but the minimum fundamental aspects are given to provide a sound overview about the subject addressed. Although perovskite materials have not yet found application as commercial catalysts, their importance in efforts to correlate solid-state chemistry with catalytic properties, their properties as they depend on the preparation methods, and the fact that they can be tailored for specific catalytic needs make these oxides prototype models for heterogeneous catalysts.

In section II, perovskite and other related structures are briefly summarized. Section III refers to the acid–base and redox properties of the perovskites, which will facilitate an understanding of the catalytic action of these systems. Section IV reviews the reactions in which perovskite oxides have been used as catalysts. Emphasis is placed not only on reactions that have been studied in depth in recent years but also on the relationship between catalytic performance and solid-state properties. Finally, in last section, based on the whole work, some prospective lines of research are suggested.

II. Structure of Perovskites

A. Crystal Structure

The ideal perovskite-type structure is cubic with space group $Pm\bar{3}m-O_h^1$. In the unit formula of perovskite-type oxides ABO_3 , A is the larger cation and B is the smaller cation. In this structure, the B cation is 6-fold coordinated and the A cation is 12-fold coordinated with the oxygen anions. Figure 1 depicts the corner sharing octahedra that form the skeleton of the structure, in which the center position is occupied by the A cation. Alternatively, this structure can be viewed with the B cation placed in the center of the octahedron and the A cation is in the center of the cube. The perovskite structure is thus a superstructure with a ReO_3 -type framework built up by the incorporation of A cations into the BO_6 octahedra. The significance and role of the ReO_3 -type framework as a host structure for deriving numerous structures of metal oxides has been emphasized by Raveau.⁶

In the ideal structure, where the atoms are touching one another, the B–O distance is equal to $a/2$ (a is the cubic unit cell parameter) while the A–O distance is $(a/\sqrt{2})$ and the following relationship between the ionic radii holds: $r_A + r_O = \sqrt{2}(r_B + r_O)$. However, it was found that the cubic structure was still retained in ABO_3 compounds, even though this equation is not exactly obeyed. As a measure of the deviation from the ideal situation, Goldschmidt⁷

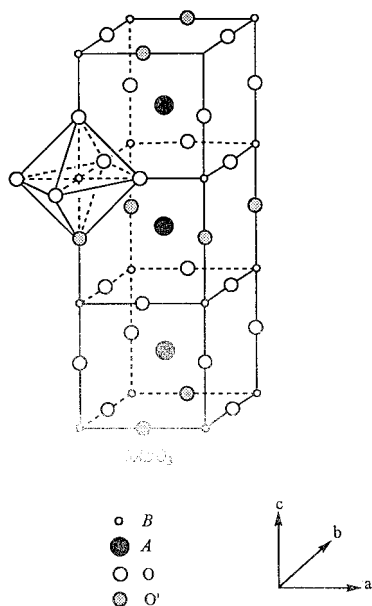


Figure 1. ABO_3 ideal perovskite structure showing oxygen octahedron containing the B ion linked through corners to form a tridimensional cubic lattice.

introduced a tolerance factor (t), defined by the equation:

$$t = (r_A + r_O) / \sqrt{2}(r_B + r_O) \quad (1)$$

which is applicable at room temperature to the empirical ionic radii. Although for an ideal perovskite t is unity, this structure is also found for lower t -values ($0.75 < t < 1.0$). The ideal cubic perovskite structure appears in a few cases for t -values very close to 1 and at high temperatures. In most cases, different distortions of the perovskite structure appear. The naturally occurring compound $CaTiO_3$ was originally thought to be cubic, but its true symmetry was later shown to be orthorhombic.⁸

The simple perovskite structure may be appropriately modified by incorporating two types of B ions with suitable different size and charge. The most frequent substitutions are the equiatomic proportions of the two ions at the B-site, for which the general formula of the perovskite is $A_2BB'O_6$ (or $AB_{0.5}B'_{0.5}O_3$). The resulting unit cell may be viewed as doubled along the three axes, regarding the primitive cell of ABO_3 . If the charge of B and B' is different, in the ordered structure the oxygens are slightly shifted toward the more charged cation although the octahedral symmetry of B and B' cations is preserved.

Deviations from the ideal structure with orthorhombic, rhombohedral, tetragonal, monoclinic, and triclinic symmetry are known, although the latter three ones are scarce and poorly characterized.^{9–11} The distorted structure may exist at room temperature, but it transforms to the cubic structure at high temperature. This transition may occur in several steps through intermediate distorted phases. These deviations from the cubic perovskite structure may proceed from a simple distortion of the cubic unit cell, or an enlargement of the cubic unit cell, or a combination of both.

B. Nonstoichiometry in Perovskites

Besides the ionic radii requirements, another condition to be fulfilled is electroneutrality, i.e., the sum of charges of A and B equals the total charge of oxygen anions. This is attained by means of appropriate charge distribution of the form $A^{1+}B^{5+}O_3$, $A^{2+}B^{4+}O_3$, or $A^{3+}B^{3+}O_3$. In addition to this, partial substitution of A and B ions is allowed, thus yielding a plethora of compounds while preserving the perovskite structure. However, deficiencies of cations at the A- or B-sites or of oxygen anions are frequent, which results in defective perovskites. The nonstoichiometry in perovskites has been widely discussed in several reviews.^{12–14}

Oxygen vacancies are more common than those involving cationic vacancies. The best-known example of perovskite oxide with ordered anion vacancies is the brownmillerite structure exhibited by $Ca_2Fe_2O_5$ ¹⁴ and $La_2Ni_2O_5$.¹⁵ The former composition can be considered as an anion-deficient perovskite with one-sixth of the oxygen ions being vacant. Oxygen vacancies are ordered in alternate (001) BO_2 planes of the cubic structure such that alternate [110] rows of oxide anions are missing. Ordering of oxygen vacancies appears more complex in O-deficient $La_2Ni_2O_5$ perovskite. Since tetrahedral coordination of Ni^{2+} is unlikely, it has been suggested that oxygen vacancies ordering in $La_2Ni_2O_5$ is accommodated by means of disordered intergrowths of octahedral and square-planar layers. The review by Rao et al.¹² covers these aspects with several examples. Until now, only a few examples with an apparent oxygen excess are known. This can be achieved by the introduction of cation vacancies at the A- and/or B-site. Structural features of this type of compound can be found in the reviews by Rao et al.¹² and Smyth.^{13,14}

1. Oxygen Nonstoichiometry

Oxygen excess nonstoichiometry in perovskite oxides is not as common as anion-deficient nonstoichiometry probably because introduction of interstitial oxygen in perovskite structure is thermodynamically unfavorable. A few systems display apparent oxygen excess, including $LaMnO_{3+\lambda}$, $Ba_{1-\lambda}La_\lambdaTiO_{3+\lambda/2}$ and $EuTiO_{3+\lambda}$. The best-characterized perovskite showing oxidative nonstoichiometry is $LaMnO_{3+\lambda}$. This sample, prepared by calcination of the individual oxides in air at 1473 K, proved to have a composition of $LaMnO_{3.12}$.¹⁶ Similar λ values for lanthanum manganite were reported by Voorhoeve et al.,¹⁷ Vogel et al.,¹⁸ Taguchi et al.,¹⁹ and Kamegashira et al.²⁰ Neutron diffraction studies revealed that oxygen excess in $LaMnO_{3.12}$ is accommodated by vacancies at the A- and B-sites with partial elimination of La (as La_2O_3), the composition of the perovskite being $La_{0.94}Mn_{0.98}O_{3.02}$ (blank space is a cation vacancy). The nonstoichiometry in $LaMnO_{3+\lambda}$ can also be modified by partial substitution of A and B cations.^{21–23} Thus, in $Sr_xLa_{1-x}MnO_{3+\lambda}$ perovskites ($x = 0.0–0.5$) Mizusaki et al.²³ found oxygen nonstoichiometry in the temperature range from 873 to 1273 K. For $x \leq 0.4$, the plot of $3+\lambda$ vs $\log P(O_2)$ [$P(O_2)$ is the oxygen partial pressure] showed two pla-

teaus: one around the stoichiometric point ($\lambda = 0.0$) and the other at low temperatures and high $P(\text{O}_2)$ at which $3+\lambda$ was saturated. The plot of $3+\lambda$ vs $\log P(\text{O}_2)$ was rationalized in terms of a defect model, which is based on the following assumptions: (i) Because the trivalent cation vacancies cause a large electronic imbalance and local lattice distortion, they do not stay close to each other. (ii) with the formation of cation vacancies, a nonbonding O2p level is formed by the oxide ions around the vacancies. This nonbonding O2p level serves as the hole-trap. Applying this structure, nonstoichiometry of the oxygen-deficient composition was explained by the random distribution of oxide-ion vacancies. However, analysis based on the defect equilibrium did not allow the identification of the cation vacancy site, whether it is a La site or a Mn site, or both, because the results were almost identical whatever the cation vacancy site. Fortunately, a detailed neutron diffraction analysis was conclusive, placing the cation vacancies predominantly on the La site.

Many oxygen-deficient perovskites can be described on the basis of complex perovskite-related superstructures of general formula $A_nB_n\text{O}_{3n-1}$, in which the stacking manner depends on the size, electronic configurations, and coordination numbers of A and B cations.²⁴ Although most of the 3d cations have led to the formation of these $A_nB_n\text{O}_{3n-1}$ phases, the nickel family has been less studied due to the difficulty in stabilizing this element with two oxidation states. Pioneering work by Crespin et al.²⁵ revealed that the $\text{La}_2\text{Ni}_2\text{O}_5$ phase, where Ni shows a 2+ formal oxidation state, is monoclinic showing a brownmillerite-type structure, i.e., with one octahedral layer alternating with one tetrahedral layer along the *b* axis. However, Rao et al.²⁶ described this material on the basis of a tetragonal cell, the oxygen vacancies giving rise to square-planar and octahedral coordination for Ni^{2+} . A detailed description of the microstructure of LaNiO_{3-y} ($y = 0.50, 0.33, 0.25$, and 0.20) perovskites was done by Sayagués et al.¹⁵ using high-resolution electron microscopy (HREM) and selected area electron diffraction (SAED).

For the $\text{La}_2\text{Ni}_2\text{O}_5$ stoichiometry, the most likely structural model can be described as formed by an octahedral layer alternating, in an ordered way, with a square-planar layer along the $[100]_c$ direction. However, the cell symmetry is, according to Crespin et al.,²⁵ monoclinic probably due to a tilt of the octahedra. In $\text{La}_4\text{Ni}_4\text{O}_{11}$ unoccupied oxygen positions are located on the octahedral apex of the perovskite superstructure leading to square-planar coordination for the 50% of Ni^{2+} . Finally, oxygen nonstoichiometry in both $\text{LaNiO}_{2.8}$ and $\text{LaNiO}_{2.67}$ is accommodated by disordered intergrowth of octahedral and square-planar layers along $[100]_c$. According to the structural models,¹⁵ it appears that the square-planar coordination layers are coincident in each *n* planes. However, for odd members, the periodicity range is longer since the square-planar layers only coincide every $2n$ planes, suggesting that different thermodynamic conditions would be necessary to stabilize them.

$\text{LaCuO}_{3-\delta}$ perovskite is stable over a remarkably wide oxygen stoichiometry range, i.e., $0.5 \geq \delta \geq 0.0$.²⁷

The stabilization of the highly oxidized rhombohedral LaCuO_3 is only achieved under a very high oxygen pressure of 6.5 GPa and 1670 K.²⁸ This stoichiometric perovskite, containing 100% Cu^{3+} , loses oxygen upon heating under ambient oxygen pressure, yielding several $\text{LaCuO}_{3-\delta}$ oxygen deficient phases as intermediates. Thus, the tetragonal, monoclinic, and orthorhombic forms of oxygen-deficient $\text{LaCuO}_{3-\delta}$ can be isolated as pure phases by annealing in Ar at 573, 673, and 773 K, respectively.²⁹ It was found that the presence of a large number of ordered oxygen vacancies in the bulk structure and the ability to form a surface shell of CuO_6 polyhedra, with Cu^{3+} , containing very labile oxygen ions, account for the high catalytic activity in CO oxidation in the most oxygen-defective materials.³⁰

2. Cation Nonstoichiometry

An oxygen excess can also readily be achieved in perovskites that are structurally deficient in oxygen because of cation nonstoichiometry. For example, it has been shown that CaTiO_3 can accept excess TiO_2 in solid solution up to 1%, and it is assumed that this is accommodated by the formation of calcium and oxygen vacancies.³¹ The resulting oxygen vacancies enhance the oxidation of the material. The minimum value in the equilibrium conductivity shifts to lower oxygen activities with increasing excess TiO_2 in the same way that it shifts with increasing acceptor contents.^{31,32} TiO_2 -rich compositions can be considered to be stoichiometric with respect to the oxygen content, i.e., with respect to oxidation–reduction equilibria, when they are composed of a combination of the stoichiometric binary oxides, $(1-x)\text{CaO} + \text{TiO}_2$ or $\text{Ca}_{1-x}\text{TiO}_{3-x}$. On the other hand, they are obviously nonstoichiometric with respect to the cation ratio.

B-site vacancies in perovskite oxides are not so common, although a few examples displaying this type of defect are known. This is a consequence of the fact that the B-site vacancies are not thermodynamically favored because of the large charge and the small size of the B cations. B–B interactions, which can be regarded as a compensating factor, are favored by the hexagonal stacking of AO_3 layers. Thus, a number of hexagonal perovskites containing B-site vacancies has been described.¹² These vacancies are usually ordered between h–h layers, where the BO_6 octahedra share faces, in agreement with the Pauling's rules for the sharing of coordination polyhedra. According to this rule, corner-sharing is more favorable than face-sharing polyhedra in *quasi*-ionic crystals. Thus, $\text{Ba}_5\text{Ta}_4\text{O}_{15}$ displays a five-layer sequence in which the octahedral site between the h–h layers is vacant. Such an ordering gives rise to isolated clusters of four octahedra that share each two opposite corners $[\text{Ta}_4\text{O}_{15}]^{10-}$.

Other perovskites exhibit A-site vacancies. This is because the BO_3 array in the perovskite structure forms a stable network, the large A cation at 12 coordinated sites can be partially missing. One interesting example of A-site defective perovskite is the $\text{Cu}_{0.5}\text{TaO}_3$, which displays a pseudocubic perovskite structure. Its unit cell is orthorhombic with eight formula units per cell. Tantalum atoms form a

TaO₃ framework as in a cubic perovskite, while the copper ions are ordered at the A-site. Three of them are located in the middle of the cube edges, while the fourth is statistically distributed over the three face centers.

C. Physical Properties

Although the physical properties of perovskite-type oxides are beyond the scope of this review, a brief account of those most relevant to these compounds is summarized below. The ABO₃ perovskites display several interesting physical properties such as ferroelectricity (BaTiO₃), ferromagnetism (SrRuO₃), weak ferromagnetism (LaFeO₃), superconductivity (YBa₂Cu₃O₇), large thermal conductivity due to exciton transport (LaCoO₃), insulator-to-metallic transitions of interest for thermistor applications (LaCoO₃), a fluorescence compatible with laser action (LaAlO₃:Nd), and transport properties of interest for high-temperature thermoelectric power (La₂CuO₄).

Magnetic Properties. In the ideal cubic perovskite structure, each oxygen is shared by two B³⁺ ions, forming a B–O–B angle of 180°. Such a configuration is favorable for superexchange interactions between magnetic B³⁺ cations. This exchange usually results in antiparallel coupling of nearest-neighbor magnetic moments. When the B³⁺ ions are in two sublattices (A₂BB'O₆) other spin arrangements are possible. If B' is a diamagnetic ion, the B³⁺ ions are aligned antiferromagnetically, and the most important exchange mechanism is believed to be a longer range superexchange interaction through two oxygens of the type B–O–B'–O–B. The B–B separation is now considerably longer than the 0.4 nm separation found in the ideal perovskite. The LnFeO₃ (Ln = lanthanide) perovskites are those that have attracted the most attention because of their possible applications as technological magnetic materials.³³ These compounds show a weak spontaneous magnetic moment, which is attributed to a slight canting of the iron moments, which are otherwise antiferromagnetically aligned. The iron moments align in such a way that the direction of easy magnetization is along the *a* or *c* axis of the orthorhombic cell. The weak ferromagnetic moment of 0.03–0.07 μ_B/mol led to the materials being considered for memory devices. Similarly, LnMnO₃ shows very interesting magnetic properties. These manganites containing mostly Mn³⁺ or Mn⁴⁺ ions show antiferromagnetic behavior. However, ferromagnetic behavior is observed in the range from 25 to 35% Mn⁴⁺. A weak magnetic interaction was found between Mn³⁺ ions, together with a negative interaction between Mn⁴⁺ ions and a strong positive interaction between Mn³⁺ and Mn⁴⁺. A similar kind of behavior was found for the combination of Co³⁺ and Co⁴⁺, but the Cr and Fe compounds were found to be antiferromagnetic.

Electrical Properties. The electrical conductivity of perovskites also shows wide variations. Several compounds have been used for their dielectric properties, while others show metallic conductivity, although most are semiconductors. As for other compounds, the electrical behavior in perovskites depends on the

outermost electrons, which may be localized at specific atomic sites or may be collective. Since localized electrons may carry a spontaneous moment, there is a strong correlation between the electrical and magnetic properties of perovskites. Rare-earth perovskites containing transition ions show widely differing electrical properties.⁹ For example, LaNiO₃, which contains nickel in the low-spin state Ni^{III}, and LaTiO₃ exhibit collective d-electron behavior, showing a metallic conductivity and Pauli paramagnetism. In the LnCrO₃ (Ln = lanthanide) perovskite series, LaCrO₃ is a semiconductor. For the heavier chromites, there seem to be two regions of conductivity. In the low-temperature region, the activation energy increases along the lanthanide series (from 0.27 eV for Dy to 0.37 eV for Yb), while the high-temperature region is characterized by a value of about 0.23 eV. The mechanism of conduction is attributed to the presence of high mobility Cr⁴⁺ ions giving rise to p-type extrinsic conduction. The decrease in conductivity in the heavier chromites may be related to a decrease in the covalence of the Cr–O bond and an increased covalence of the Ln–O bond.⁹ LaMnO₃ perovskite exhibited an abrupt change in conductivity as well as in magnetic susceptibility as a function of temperature close to 720 K. This behavior was explained on the basis that the charge carriers would be holes hopping among localized levels. LaCoO₃ displays an even more complex behavior.⁹ It is a semiconductor up to about 400 K, after which conductivity increases much more rapidly up to 823 K; in the region from 823 to 1200 K it passes through a broad, flat maximum, and, finally, above 1200 K it shows a metal-like behavior. At low temperatures, the Co ions are mainly in the low-spin Co^{III} state, and this coexists with the high-spin paramagnetic Co³⁺ state at higher temperatures. As the temperature is further increased, the Co³⁺ and Co^{III} ion pairs transform to Co²⁺ and Co^{IV} pairs. Thus, the fraction of Co³⁺ disappears around 1200 K when only long-range order is present, resulting in a first-order transition. Along with the spin behavior, the outer electrons also show a transition from the localized to a collective behavior. Conductivity can be enhanced considerably by partial substitution of the lanthanide by a divalent ion. Thus, for Sr_xLa_{1-x}MnO₃ the Mn ions are Mn³⁺ for *x* = 0. However, an increase in *x* results in the creation of Mn⁴⁺ holes, thereby increasing conductivity. For substitutions 0.2 < *x* < 0.4 the system becomes ferromagnetic and shows a metal–semiconductor transformation. A similar type of behavior was observed in Sr-substituted cobaltites.

The electrical properties of perovskites have aroused special interest since the discovery in 1986 of superconductivity at 40 K in cuprates.⁵ These cuprates are hole superconductors, exhibiting a mixed valence of copper Cu^{II}–Cu^{III}. Among these, the exception is Ce-doped Nd₂CuO₄, with *T_c* close to 25 K,³⁴ which belongs to a different structural type and is an electron superconductor. All these compounds have a common feature, the bidimensional character of the structure, which has been shown to be an important factor for the existence of superconductivity at high temperature.³⁵

Optical Properties. Compounds with the perovskite structure have been used as model systems for spectroscopic studies in the infrared, the visible, and the ultraviolet. Perovskite oxides (ABO_3) are particularly suited since the effect of magnetic ordering of the transition metal ion in the B-site can be studied in addition to that of the rare earth ion A. Because the difference in ordering temperature of the two types of ions is large there is little interaction. The absorption spectra either for the host ion of the perovskite structure or after incorporation of a low-concentration "probe" into a diamagnetic lattice can be studied. In the former case of magnetically concentrated systems, a broad spectrum is obtained, with line widths typically of $0.5\text{--}5\text{ cm}^{-1}$, while in the latter a sharp spectrum is obtained, with line widths of about 0.1 cm^{-1} . The optical properties of many ABO_3 compounds, in which B is a transition metal ion with an empty or partially filled d-shell, have been explored. For the SrTiO_3 perovskite containing an empty d-shell transition ion (Ti^{4+}), the emission spectrum shows luminescence which is independent of sample history and contamination and shows a band maximum at about 500 nm, with low quenching temperature (35 K) and a small Stokes shift (7000 cm^{-1}). The titanate octahedra sharing corners in SrTiO_3 are favorable for energy band formation. The broadening of the energy levels of the titanate octahedron results in a considerably lower energy for the first absorption transition, and the excited state of the titanate becomes mobile. This situation has been described as being due to the coexistence of free and delocalized (self-trapped) excitons.³⁶ A large body of work on the optical properties of metal ions with a partially filled d-shell containing perovskites exists. Ions with the d^3 configuration have been extensively used to investigate the optical properties of perovskites. Cr^{3+} spectroscopy has been studied in perovskites MTiO_3 ($M = \text{Ca, Sr, Ba}$) and ABO_3 ($A = \text{La, Gd, Y; B = Al, Ga}$). In these systems, the Cr^{3+} ion may show two completely different types of emission, viz. narrow-line and spin-forbidden emission (${}^2\text{E} \rightarrow {}^4\text{A}_2$) and broad-band and spin-allowed emission (${}^4\text{T}_2 \rightarrow {}^4\text{A}_2$), the latter occurring for relatively weak fields. The transition-metal doped titanates became of interest after the discovery of photoelectrochemical water splitting by titanates.³⁷ It appeared possible to sensitize an SrTiO_3 electrode for visible light by doping with transition metal ions.³⁸ The optical transitions involved were shown to be of the metal-to-metal charge-transfer type, e.g., $\text{Cr}^{3+} + \text{Ti}^{4+} \rightarrow \text{Cr}^{4+} + \text{Ti}^{3+}$, which are responsible for the brownish color of the composition.

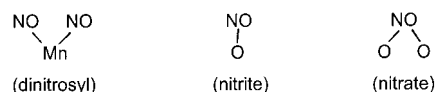
D. Adsorption Properties

The identification of the nature and structure of the exposed sites on the perovskite surfaces as well as the possible involvement of these sites in catalytic reactions have frequently been studied by the adsorption of suitable probe molecules. Both the equilibrium and the kinetics of adsorption and, in some cases, the desorption of molecules from the surface were analyzed.

1. CO and NO Adsorption

The extent of CO adsorption on LaBO_3 ($B =$ transition metal) perovskites at 298 K was found to be dependent upon on the electron configuration of the B^{3+} cation and was seen to reach a maximum for Fe^{3+} ,³⁹ which mirrors the profile observed for isobutene adsorption on the same perovskite series. In general, adsorption is fast and the kinetics can be satisfactorily described by the Elovich equation.⁴⁰ Successive adsorptions of CO_2 -CO on LaCrO_3 allowed the authors to conclude that CO_2 and CO adsorb onto the site type of surface centers.⁴¹ By contrast, preadsorption of O_2 followed by CO adsorption revealed that the extent of CO adsorbed at equilibrium approached that measured on a clean surface. This finding indicates that O_2 and CO adsorb on different surface sites.⁴¹ It was also observed that CO interaction occurs with surface oxygen and metallic ions.^{39,41-44} This is an activated process because the amount of adsorbed CO increases with the temperature of adsorption from 298 to 773 K.

NO adsorption at 298 K on a series of LaBO_3 oxides showed maxima for Mn and Co.³⁹ The extent of NO adsorption was found to be independent of temperature for LaFeO_3 ⁴⁵ and LaNiO_3 ³⁹ over a wide temperature range (273–673 K). This observation suggests that the nature of the adsorption is not altered with temperature. For LaCrO_3 ,⁴⁶ LaMnO_3 ,⁴² and LaRhO_3 ,⁴⁷ the temperature interval where NO adsorption changes moderately (below 20%) was narrower. NO coverage on all these oxides were found to be of the same order of magnitude as those measured for the simple oxides.⁴⁸ The infrared spectra of NO adsorbed on the manganite LaMnO_3 showed bands of dinitrosyls and nitrite and nitrate species.⁴⁷ This finding indicates that NO molecule interacts either through Mn^{3+} ions (dinitrosyls) or through O^{2-} ions (nitrite and nitrates) as illustrated in the scheme:



Successive NO-CO and CO-NO adsorptions on LaMO_3 at 298 K showed an inhibiting effect of NO on subsequent CO adsorption, and this was larger than the inhibiting effect of CO on NO adsorption.³⁹ NO adsorbs more strongly than CO, in accordance with previous observations by Yao and Shelef⁴⁸ for other perovskites. Consistent with this, comparison of the thermodynamic parameters for the adsorption of NO and CO on LaCrO_3 revealed higher adsorption enthalpy and lower adsorption entropy for NO than for CO. The almost constancy of the amounts of adsorbed NO with temperature as well as the strength of the NO-surface bond are arguments in favor of the use of NO instead CO for determining metallic sites.^{39,42,44,45,47} However, the complex IR spectra of chemisorbed NO^{39,42,45} indicate that there is no specificity for the adsorption on metal or cation sites, and, therefore, the assumption of a 1:1 stoichiometry between NO and B^{3+} sites may not give a proper estimate of the density of surface transition-metal

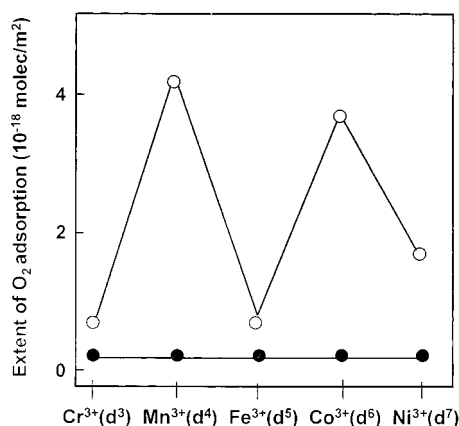


Figure 2. Extent of total (open circles) and reversible (filled circles) oxygen adsorption on clean LaMO₃ surfaces. Reprinted from ref 49 by permission of the publisher. Copyright 1985 by The Royal Society.

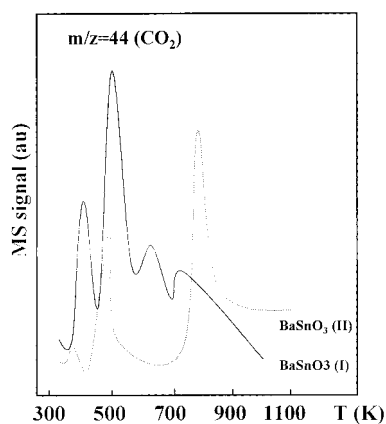


Figure 3. Temperature-programmed desorption profiles of CO₂ from BaSnO₃ perovskites: (I) prepared ex-tin oxide and (II) prepared ex-chloride. Reprinted from ref 116 by permission of the publisher. Copyright 1996 by Elsevier.

sites. Thus, the CO molecule, whose interaction with B³⁺ ions is weaker than with NO at temperatures close to ambient, is recommended for evaluating B³⁺ cations in perovskite oxides.

2. Oxygen Adsorption

Oxygen adsorption on perovskite oxides has been studied mainly because of the importance of these compounds as oxidation–reduction catalysts. The oxygen adsorption profiles on LaMO₃ (M = Cr, Mn, Fe, Co, Ni) were reported by Kremenec et al.⁴⁹ These profiles displayed maxima for Mn and Co (Figure 2) that coincide with the maxima observed by Iwamoto et al.⁵⁰ for the respective single transition metal oxides (M₂O₃) and also for the catalytic activity of oxidation of this series of perovskites.⁴⁰ It can also be noted in Figure 3 that the amount of reversible adsorbed oxygen represents a very small fraction of the total adsorption, in agreement with previous findings.⁵¹

Oxygen TPD peaks from perovskites appeared to be rather complex. Yamazoe et al.⁵² and Seiyama et al.⁵³ observed two oxygen desorption peaks after adsorption on La_{1-x}Sr_xCoO₃ at 1023 K. The low-temperature peak (α -type) was ascribed to adsorbed oxygen, whereas the high-temperature peak (β -type)

was attributed to lattice oxygen. The changes in intensity of the α -type peak with x in La_{1-x}Sr_xMO₃ (M = Mn, Fe, Co) have been interpreted in terms of the nonstoichiometry and defect structure of these perovskites.^{51,52–56} In a recent contribution, Yokoi and Uchida⁵⁷ observed that the amount of O₂ desorbed and the temperature of the α -type oxygen desorption from LaMO₃ (M = Cr, Mn, Fe, Co, Ni) tended to decrease with the increasing atomic number of the transition metal.^{57,58} The strength of the force preventing O₂ desorption was also estimated by model calculations using the DV-X α cluster method.⁵⁹ The calculated bond order for M–O became smaller with the increasing atomic number of M, which suggests that the temperature of O₂ desorption during TPD of O₂ was affected by the electronic interaction between the adsorbed O₂ and the transition metal ion (M³⁺). The β -type oxygen desorption peak was found to be more specifically associated with the M cation, although it is also affected by Ln-site substitution.

As a general rule, oxygen adsorption on the perovskite oxide surface is a complex process. As recently reported by Au et al.,⁶⁰ oxygen adsorption is dominated by a molecular form according to a fast process followed by a much slower, activated adsorption kinetics, associated to formation of oxygen-charged species (O₂ \rightarrow 2O²⁻).

E. Specific Surface and Porosity

Many different methods have been used in the preparation of perovskite oxides; the choice of a particular one basically depends on the expected application of these oxides. The application of perovskite oxides in the field of heterogeneous catalysis requires materials with a well-developed porous network. Since this review is mainly concerned with the surface and catalytic properties of perovskites, emphasis is placed on the specific area and porosity of powdered samples. Preshaped perovskite oxides in honeycomb type structures and highly ordered thin films are also briefly examined.

Classical methods of the preparation of perovskite oxides include: (i) equimolecular oxide mixing synthesis and (ii) decomposition synthesis. Type i method requires a high calcination temperature (1300–1500 K) for the solid state reaction to occur and often results in the formation of coarse aggregation. The grain size of the powder obtained by this method is relatively large and the specific area is too small, making it unsuitable for catalytic applications. Another major drawback of this method is that the purity of the product is not high. Type ii method, however, requires lower synthesis temperatures, usually below 1100 K; thus high purity and homogeneity of the product are attainable. The differences between methods i and ii were clearly shown by Berndt et al.⁶¹ These authors found that the solid-state reaction of mixtures of separately precipitated hydroxides proceeded much faster than that of physical mixtures of single oxides (ceramic method).

Spray-drying, freeze-drying, and coprecipitation methods are simple techniques for preparing agglomeration-free submicrometer powders, with high

purity, controlled stoichiometry, crystallinity, and relatively narrow particle-size distribution. These three methods were compared in the preparation of substituted manganites of the type $\text{La}_{1-x}\text{M}_x\text{MnO}_3$ ($\text{M} = \text{Sr}, \text{K}, \text{Pb}, \text{Ce}, \text{Co}, \text{Ni}, \text{Mg}, \text{Li}$).⁶² The former method yielded solids with some compositional segregation and specific areas below $17 \text{ m}^2/\text{g}$, while the latter led to well-crystallized oxides, with specific areas smaller than $10 \text{ m}^2/\text{g}$. Even larger specific areas were obtained with freeze-drying because of the lower temperature required in the calcination step.

Some novel low-temperature preparation methods include carbonate,⁶³ hydroxide,^{64,65} cyanide, and mixed nitrate decomposition,^{63,64} oxalate coprecipitation, and urea homogeneous precipitation followed by thermal decomposition,⁶⁶ as well as the sol-gel processes using citric acid⁶⁷ poly(acrylic acid),⁶⁸ poly(ethylene glycol),^{69,70} poly(vinyl alcohol),⁷¹ malic acid,⁷² and stearic acid⁷³ as the media for protecting the colloidal particles. However, the powders prepared by most of these methods still have low specific areas, usually below $10 \text{ m}^2/\text{g}$, except that the sol-gel methods yield well-crystallized samples with larger specific areas ($11\text{--}20 \text{ m}^2/\text{g}$) mainly because the calcination temperatures are as low as $823\text{--}923 \text{ K}$, i.e., $200\text{--}300 \text{ K}$ lower than that used in the carbonate process.⁶³ Among the sol-gel processes, the use of stearic acid in the preparation offers the possibility of synthesizing high purity homogeneous nanocomposites with relatively larger specific areas at reasonably low processing temperatures.⁷⁴ Following this method for the preparation of LaCoO_3 perovskite, the synthesis conditions can easily be controlled, and crystalline structures are obtained at temperatures as low as $773\text{--}873 \text{ K}$. The ultrafine perovskite particles ($20\text{--}70 \text{ nm}$) are spherical, of uniform size, and have specific areas higher than $30 \text{ m}^2/\text{g}$, substantially higher than that obtained by the conventional methods.

The hysteresis loops of the adsorption isotherms recorded on samples prepared by freeze-drying and explosion methods belong to the A-type according to de Boer's classification,⁷⁵ while the adsorption isotherms of the samples prepared by ceramic and coprecipitation methods give type B-loops. This clear differentiation proves that the porous texture of the powdered samples is strongly dependent on the preparation method. It seems worth mentioning that some powdered perovskites showed stepwise adsorption isotherms. Since the adsorption of different probe molecules on oxide surfaces pointed to the existence of an energetically heterogeneous surface, it appeared that step formation in these systems must be due to lateral interactions of adsorbed nitrogen molecules rather than to the presence of a homogeneous surface.⁷⁶

Flat perovskite surfaces can readily be obtained by epitaxial thin film growth on well-defined substrates.^{77–81} Of particular interest is the SrTiO_3 perovskite that serves as a substrate for growing oxide superconducting films.^{82,83} Tanaka et al.⁸¹ studied the atomic configuration and chemical properties of a SrO - and TiO_2 -terminated SrTiO_3 (001) surface produced by laser molecular beam epitaxy

(MBE) using an atomic force microscope (AFM) with a surface-modified tip. Both terminated surfaces displayed a terrace structure consisting of an atomically flat plane and steps of height 0.4 nm corresponding to the unit cell step. When measured using a TiO_2 -coated tip, the friction force of the SrO -terminated surface was found to be larger than that of the TiO_2 -terminated surface. This suggests that the forced friction would be caused by the bonding energy present at the interface, which provides a method for measuring the chemical energy present in oxide compounds of the nanometer order between the surface and the tip of the microscope.

Chemical vapor deposition was also used for the preparation of dense perovskite films, i.e., nonvolatile random access memory ferroelectrics, possessing an extremely low porosity.^{84,85} Other approaches consisted of the epitaxial growth of a thick perovskite layer on an ordered substrate. The epitaxial thin film of the ordered double $\text{Sr}_2\text{FeMoO}_6$ perovskite has been successfully prepared on SrTiO_3 (001) and (111) substrates by pulsed laser deposition in a narrow window of temperature and oxygen pressure.⁷⁹ The diffraction patterns of the (111) oriented film exhibited the reflection peaks of a double perovskite unit cell ($a_0 \approx 0.8 \text{ nm}$), indicating B-site ordering. The in situ reflection high-energy electron diffraction pattern revealed clear 2-fold superstructure corresponding to the double perovskite unit cell. The surface topology of these films was revealed by atomic force microscopy. The (001) oriented film showed an atomic-scale step-and-terrace structure. The step height was about 0.4 nm , which corresponds to single perovskite unit cell height. This agrees with the expectation for the $\text{Sr}_2\text{FeMoO}_6$: each perovskite sheet is equivalent and includes the same number of FeO_6 and MoO_6 octahedra arranged like a checkerboard. Since the direction of the steps is almost identical in the entire region of the sample, the structure should reflect the surface steps of the SrTiO_3 substrate, as also observed for $(\text{La},\text{Sr})\text{MnO}_3$ films.⁸⁶ On the other hand, the (111) ordered oriented film displayed triangular-shaped grains. A spiral structure of atomic-scale steps was observed on the grains, indicating that the growth mode of the film is two-dimensional spiral growth mediated by screw dislocation. It was observed that the height of each step was about 0.45 nm , which corresponds to the (111) d -spacing of the $\text{Sr}_2\text{FeMoO}_6$ unit cell and half of this. This implies that the growth of the (111) oriented film takes place with the chemical formula as a growth unit and that there exists a preferred surface termination of the B-site cation.

The atomic layered perovskite films reported here are excellent model surfaces to investigate chemical reactions between adsorbed molecules at atomic scale. Atomic force microscopy becomes an extremely useful tool not only to investigate the topology of the surface at very high resolution but also to develop specific adsorbed molecule-surface site locations, which opens the possibility of investigating chemical reactions on the catalytic surfaces.

Since perovskites had demonstrated excellent performance in exhaust treatment (see section IV.B), it

was believed that they could be supported on an inert ceramic substrate such as cordierite ($2\text{Al}_2\text{O}_3 \cdot 5\text{SiO}_2 \cdot 2\text{MgO}$), as already done in the three-way catalysts used in the car engine exhaust gases. In the first attempts⁸⁷ to deposit a perovskite layer on a cordierite monolith, the procedure basically included dipping the ceramic monolith in an aqueous slurry of powdered perovskite, followed by drying and firing to bind the perovskite to the surface. It was found that in alumina-based monoliths the decrease in catalytic performance might partly be due to a solid-state reaction between the perovskite and the alumina substrate. An approach used by Mizuno et al.⁸⁸ to circumvent reaction of the active phase ($\text{La}_{0.8}\text{Sr}_{0.2}\text{CoO}_3$) with a high specific area substrate consists of precoating the cordierite with a La_2O_3 layer. A maximum in activity for the combustion of propene at 673 K was observed for 18% La_2O_3 incorporated, which correlates well with the fraction of the monoclinic La_2O_3 phase present. Nudel et al.⁸⁹ used Al_2O_3 (25 m^2/g) previously stabilized by impregnation with $\text{La}(\text{NO}_3)_3$. Subsequent impregnation with an equimolecular solution of Co^{2+} and La^{3+} nitrates, followed by firing at 1173 K gave rise to a complex solid containing $\gamma\text{-Al}_2\text{O}_3$, LaAlO_3 , CoAl_2O_4 , and LaCoO_3 phases. This example is a good illustration of the difficulty involved in obtaining a pure perovskite phase on a reactive substrate.

Recently, Schneider et al.⁹⁰ prepared $\text{La}_{0.84}\text{Sr}_{0.16}\text{Mn}_{0.67}\text{Co}_{0.33}\text{O}_3$ perovskite-coated and perovskite-extruded monolith catalysts and tested the combustion of several aliphatic chlorinated hydrocarbons. The coated monolith catalysts were prepared by a two-step procedure. First, the monolith cordierite ceramic support was impregnated with a solution containing appropriate amounts of the corresponding nitrates. After air-calcination at 873 K, the impregnated monoliths were coated with a bulk perovskite-water suspension. Then, the dried sample was again calcined at 873 K. The perovskite-extruded monoliths were prepared by extrusion of a mixture of precipitated perovskites and a cordierite precursor in monolith form. A rather high specific area (57 m^2/g) was obtained after calcination at 823 K. Honeycomb monolith perovskite catalysts were prepared by Ciambelli et al.⁹¹ from ultradispersed powders of mixed oxides of rare-earth metals (La-Ce or Dy-Y) and transition metals (Ni, Fe, Mn) by mechanochemical methods. The honeycombs were then obtained by extrusion of plastic pastes of the perovskite powders and additives. The best performance for methane combustion was exhibited by La-Ni oxides-containing monoliths that, in turn, display the highest pore volume and fraction of macropores (20% above 1 μm).

Other preshaped structures such as foams⁹² and silica-alumina fibers⁹³ have been used as support of perovskites. Podyacheva et al.⁹² employed Ni and Ni-Cr foam substrates to deposit a LaCrO_3 perovskite phase. In both cases, preliminary washcoating of the metal surface was required in both cases to facilitate the anchorage of the perovskite phase. The perovskite was the only phase detected by diffraction methods and was stable upon calcination up to 1273 K. In a recent contribution, Klvana et al.⁹³ prepared Ni-Co-

based perovskites supported on a commercial silica-alumina fiber blanket. The system was particularly suitable for use in the combustion of lean natural gas mixtures. The perovskite deposit (12–15%) was achieved by incipient wetting of the fiber blanket with the precursor solution, followed by fast freezing of the solution wet blanket by immersion in liquid nitrogen and vacuum-drying. These systems exhibited activities comparable to those of commercial fiber-supported platinum and were found to be stable at temperatures below 1000 K.

F. Thermal Stability in a Reducing Atmosphere

The thermal stability of perovskites is determined by the cations at position A and also at position B. Arakawa et al.⁹⁴ showed that the extent of H_2 -reduction of cobalt in LnCoO_3 (Ln = lanthanide) increased from Ln = La to Ln = Eu, i.e., with decreasing ionic radius of the lanthanide element. The same reduction sequence was observed by Futai et al.⁹⁵ although the perovskites of Gd, Tb, and Dy were less reducible. These later authors also reported a direct relationship between the reducibility and the sum of the energies of the Ln-O and Co-O bonds; i.e., the ease of reduction increases with decreasing metal-oxygen bond energy. On the other hand, the stability in hydrogen of LaFeO_3 and LaRhO_3 was found to be higher than that of the corresponding yttrium perovskites.⁹⁶

In a systematic study of the Gibbs free energy of formation (ΔG°) of several ferrates from the starting metal oxides: $\text{Fe}_2\text{O}_3 + \text{Ln}_2\text{O}_3 \rightarrow 2 \text{LnFeO}_3$, in the temperature range from 1150 to 1300 K, Katsura et al.⁹⁷ found a linear relationship between the values of ΔG° and the Goldschmidt tolerance factor (t). That is, ΔG° becomes more negative with increasing values of t or increasing ionic radius of the lanthanide cation. A similar relationship was observed for the ΔG° of formation of LnFeO_3 oxides starting from metallic iron, Ln_2O_3 , and oxygen at 1470–1570 K.⁹⁸ All these results clearly indicate that the stability of the perovskite structure increases with increasing size of the lanthanide ion in the temperature interval studied and are consistent with those of Arakawa et al.⁹⁴ for LnCoO_3 oxides.

Partial substitution of the A ion by another ion of a lower oxidation state such as Sr ($\text{La}_{1-x}\text{Sr}_x\text{CoO}_3$) may also induce important changes in stability. With increasing the values of x , the concentration of unstable Co^{4+} and/or of oxygen vacancies also increase, which favors the diffusion of lattice oxygen from the bulk to surface, as charge compensators. Thus, increasing the strontium content in the defective structure of $\text{La}_{1-x}\text{Sr}_x\text{CoO}_3$ accounts for the instability of the lattice in a reducing environment.⁵¹ In contrast, the stability of the hole-doped $\text{La}_{0.8}\text{Th}_{0.2}\text{CoO}_3$ perovskite is higher than that of LaCoO_3 because part of the cobalt is present as Co^{2+} .⁹⁹

The thermal stability of perovskite oxides was found to depend also on the type of cation at the B position. Nakamura et al.¹⁰⁰ studied the structural changes of a series of LaBO_3 (B = V, Cr, Mn, Fe, Co, Ni) oxides induced by H_2 -reduction at 1273 K as a function of the oxygen partial pressure. Among the

crystalline products produced by reduction, the dismutation La_2MO_4 phases were detected, with the exception of La_2MnO_4 , which is unstable at temperatures above 1200 K.¹⁰¹ Other possible intermediate reduced mixed oxides such as $\text{La}_2\text{Co}_2\text{O}_5$, $\text{La}_2\text{Ni}_2\text{O}_5$, and LaNiO_2 phases were not observed because they are unstable. The following order of stability in terms of the $-\log P_{\text{O}_2}$ values can be established: $\text{LaNiO}_3 < \text{LaCoO}_3 < \text{LaMnO}_3 < \text{LaFeO}_3 < \text{LaCrO}_3 \approx \text{LaVO}_3$. This order parallels the Madellung constant except for LaNiO_3 and LaCoO_3 , which show higher constants. The origin of this discrepancy may be the existence of stable La_2MO_4 compounds for Ni and Co.

Crystal structures of titanium (SrTiO_3 , BaTiO_3)¹⁰² and chromium (LaCrO_3)¹⁰³ perovskites exhibited a very high stability after being exposed to a reducing atmosphere at temperatures as high as 1200 K. Other perovskites containing reducible first transition row ions in their structure underwent important crystalline and chemical transformations after less severe treatments. An exhaustive account of this was offered in our previous review.¹⁰⁴ For example, Crespin and Hall¹⁰² found that the crystal structure of LaCoO_3 is slightly altered upon quantitative H_2 -reduction of Co^{3+} to Co^{2+} . However, the diffraction pattern of the perovskite in which Co^{3+} is quantitatively reduced to metallic cobalt shows only the diffraction lines of La_2O_3 , indicating that highly dispersed metallic Co^0 would remain trapped in the La_2O_3 phase. This was already confirmed by sintering the metallic Co^0 phase upon heating at 1073 K in an He atmosphere, then after which the diffraction lines of metallic Co particles appeared.

In a recent study on the reduction–oxidation of LnCoO_3 ($\text{Ln} = \text{La}, \text{Pr}, \text{Nd}, \text{Sm}, \text{Gd}$) perovskites,¹⁰⁵ it was demonstrated that cobalt reduction occurs in two steps: near 633 K (Co^{3+} to Co^{2+}) and at 783–845 K (Co^{2+} to Co^0), the maximum of the second peak decreasing from La to Gd. Diffraction studies revealed that the perovskite NdCoO_3 is reduced in two steps, first to $\text{NdCoO}_{2.5}$ and then further to $\text{Co}^0/\text{Nd}_2\text{O}_3$, and in both stages it was demonstrated that the reoxidation with oxygen is capable of recovering the perovskite structure. Temperature-programmed oxidation with reduced $\text{LnCoO}_{1.5}$ systems indicated that the reoxidation of cobalt also takes place in two steps: first by oxidation of the supported Co^0 to the spinel Co_3O_4 followed by a further oxidation of Co^{2+} to Co^{3+} , with a simultaneous solid-state reaction with Ln_2O_3 , regenerating the perovskite structure. The nature of the Ln affects the stability of the perovskite LnCoO_3 . The Goldschmidt tolerance factor (t) for these perovskites indicates that, considering only geometric factors, lanthanum, the largest lanthanide ion in the series, forms the most stable perovskite structure. This and other examples mentioned above show that by reduction treatments or redox cycles, the metal in position B remains in a high degree of dispersion on a matrix of the Ln_2O_3 oxide. Considering the importance of dispersed metals in heterogeneous catalysis, the reduction or reduction–oxidation of perovskites under controlled conditions may offer a promising methodology for the preparation of highly active catalysts.

III. Acid–Base and Redox Properties

In this section, two important properties of perovskite-type oxides directly related to catalytic performance such as acid–base and redox are examined briefly. Since the surface of perovskites may be primarily related to their catalytic properties, the nature and concentration of the surface sites can be evaluated by analysis of the interactions of suitable probe molecules and the surfaces of these oxides. Acid sites in perovskite-type oxides have been investigated by adsorption of a basic molecule such as pyridine, whereas basic sites have been evaluated by adsorption of acid molecules such as carbon dioxide. Furthermore, the reduction of perovskites and the oxygen adsorption–reaction on their surfaces play a central role in the catalytic activity of oxygen-mediated reactions.^{104,106}

A. Acidity and Basicity

Acid sites in perovskite oxides have been determined by adsorption of pyridine. The infrared spectra of pyridine adsorbed on LaMnO_3 and LaFeO_3 at room temperature¹⁰⁷ exhibited bands at 1595, 1490, and 1440 cm^{-1} , due to the vibration modes of the pyridine bonded to Lewis sites. Pyridine adsorbed on the LaCrO_3 sample¹⁰⁸ showed similar bands but of lower intensity suggesting the presence of a smaller concentration of acid Lewis sites.

Brönsted site: MO-H^+ : $\text{N}(\text{C}_5\text{H}_5)$

Lewis site: OM: $\text{N}(\text{C}_5\text{H}_5)$

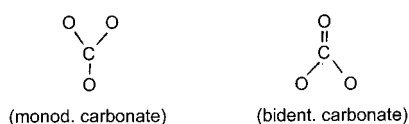
A similar spectrum to that of the unreduced samples was recorded upon pyridine adsorption on H_2 -reduced LaBO_3 oxides, exhibited similar infrared spectra together with a weak Brönsted band at 1540–1545 cm^{-1} . The intensity of this later band increased slightly upon adsorption of water at 423 K. The increase in Brönsted acidity can be understood by assuming that water molecules adsorb dissociatively on pairs of surface acid–base sites (O^{2-} ions). The band at 1490–1495 cm^{-1} is related to the pyridine adsorbed on coordinatively unsaturated exposed cations, which constitute Lewis acid sites. The presence of La^{3+} and M^{3+} ions in these perovskites with very different charge/radius ratios probably generates acid sites of markedly different strength. In any case, the weak intensity of the infrared bands of adsorbed pyridine and the removal of these bands upon outgassing at 673–873 K point to a low acidic character of these oxides.¹⁰⁷

It has been observed that calcined, and specifically H_2 -reduced, perovskite surfaces exposed to water vapor enhances the hydroxyl groups concentration.¹⁰³ The infrared hydroxyl groups spectra recorded upon water adsorption at 423 K on oxidic and reduced LaCrO_3 samples gave bands, in both cases at 3680 cm^{-1} , of isolated OH groups (site I) and at 3550 cm^{-1} of acid OH groups (site II). The adsorption and dissociation of water was assumed to take place on pairs of surface acid–base sites, yielding an acidic OH and an anion vacancy placed between coordina-

tively unsaturated La^{3+} and reduced metal ions (M^{2+} or M^+) (site I) and a basic OH^- on a coordinatively unsaturated oxygen ion bonded to a La or M ion (site II). As the dissociation of water takes place even on the oxidic samples, this suggests that during the outgassing step some O^{2-} vacancies are generated on the surface, although presumably at a low concentration, as above. In addition, the formation of these vacancies is strongly enhanced by H_2 treatment, which favors water dissociation on the reduced surface.

Many perovskite oxides exhibit basic properties which can be used to conduct several catalytic reactions.¹⁰⁴ Among the methods proposed to measure surface basicity the adsorption of benzoic acid (Brönsted basicity) and more specifically CO_2 adsorption-desorption experiments^{109–111} remain prominent. The extent of CO_2 adsorption as well as the heats of adsorption on LaBO_3 ($\text{B} = \text{Cr}, \text{Fe}, \text{Co}$) oxides were studied over a wide temperature range by Tejuca et al.^{112,113} The CO_2 coverage follows the order $\text{LaCrO}_3 > \text{LaFeO}_3 > \text{LaCoO}_3$. Activated adsorption was found to occur at temperatures above 420 K on LaCrO_3 and LaCoO_3 ; however, the extent of CO_2 adsorption on LaFeO_3 decreased continuously with increasing temperature. A modelistic analysis of the equilibrium data of CO_2 adsorption allowed to satisfactorily describe isotherms by the Freundlich model of adsorption. Sets of data of CO_2 adsorption and that of other simple molecules led the authors to propose the Freundlich equation as an additional tool to evaluate specific areas of metal oxides and perovskites.¹⁰⁸

Because CO_2 is a slightly acid molecule its adsorption on basic sites is strong. Upon CO_2 adsorption on BaTiO_3 ¹¹⁴ and LaMO_3 ($\text{M} = \text{Cr}, \text{Mn}, \text{Fe}, \text{Co}, \text{Ni}$)^{107,108,112,113} perovskites and monodentate and bidentate carbonates are formed. The former carbonates are favored at low temperatures, and in some cases transformation of these species into bidentate carbonates with increasing temperatures was observed. The broad carbonate infrared bands



provide evidence of the presence of energetically different adsorption sites. On LaFeO_3 , CO_2 adsorption gives rise to infrared bands of carbonates at 1600, 1325, 1218, 1050, and 840 cm^{-1} . The former two bands decrease in intensity upon reduction treatments, suggesting that they are associated with monodentate structures.¹¹³ The opposite trend observed for the band at 1050 cm^{-1} points to the formation of a carbonate of higher thermal stability, such as bidentate species. Finally, the band at 1218 cm^{-1} can be associated to a very labile carbonate since it was removed by outgassing at room temperature.¹¹³

CO_2 temperature-programmed desorption (TPD) measurements were also used to evaluate surface basicity in perovskites. TPD profiles after CO_2 adsorption on LaBO_3 oxides revealed two major peaks

at 340–425 K and 540–920 K.^{107,108,112,113,115} The peak at 340–425 K originates from the decomposition of a monodentate carbonate, the least stable CO_2 adsorbed species. However, the CO_2 desorption peak at 540–920 K probably arises from the decomposition of bidentate and/or bridged carbonates, whose presence was also revealed by infrared spectroscopy. A mechanism for the formation of this type of species has been advanced and consists of pair sites including a lattice oxygen and an anion vacancy. Support to this interpretation is provided by experiments on the adsorption of CO_2 on partially reduced samples in which the concentration of these carbonates increased with the extent of oxide reduction.^{107,112,113} The high-temperature desorption peak after CO_2 adsorption on reduced LaCoO_3 ⁴⁴ and LaNiO_3 ¹¹¹ samples was quite different from that of the other perovskite oxides. The intensity of the CO_2 desorption peaks showed maxima for prereduced LaCoO_3 and LaNiO_3 samples at 573 K and then decreases at higher reduction temperatures. This finding suggests an interaction of bidentate or bridged carbonates with intermediate reduction states of cobalt and nickel, such as Co^{2+} and Ni^{2+} .

Petit et al.¹¹⁶ prepared tin-containing ASnO_3 ($\text{A} = \text{Ca}, \text{Sr}, \text{Ba}$) perovskites by a sol-gel method starting from an oxide (SnO) or from chlorinated precursors (SnCl_4) and used them in the oxidative coupling of methane. They found that 10 times more CO_2 is adsorbed on BaSnO_3 ex-oxide than on BaSnO_3 ex-chloride. This difference agrees with other findings in the literature^{107–111,116,117} concerning other catalysts. Since the specific areas of the two catalysts were similar, the extent of CO_2 adsorption can therefore not be directly attributed to it. As shown in Figure 3, the shape of CO_2 TPD profiles strongly depends on the precursors used in the preparation of the two perovskites. Peaks below 470 K, very intense for ex-oxide and weak for the ex-chloride sample, were assigned to weakly adsorbed CO_2 . Other peaks located in the 500–750 K temperature range were attributed to strongly adsorbed carbonates,¹¹⁰ whereas peaks at 860 K (ex-oxide) and 910 K (ex-chloride) corresponded to the decomposition of bulk carbonates. CO_2 , which is a poison for the coupling reaction, is less strongly adsorbed on the catalyst ex-chloride. Thus, chlorine appears to stabilize the sites that are active in the coupling reaction with respect to the poisoning by CO_2 .

B. Redox Processes

The reduction and oxygen adsorption properties of several LaBO_3 ($\text{B} =$ first-row transition element) perovskite oxides^{41,49,118} conclusively demonstrated that these parameters are directly involved in the catalytic activity of these oxides for oxidation reactions. It was observed that the more easily reducible perovskite oxides (LaNiO_3 , LaCoO_3 , and LaMnO_3) resulted in better catalysts for oxidation reactions than the less reducible one (LaCrO_3).¹¹⁸ Because of the importance of this, the kinetics and mechanisms of the reduction of some perovskite oxides were briefly examined. Attention was also paid on the oxidation rates of prereduced samples. Additionally,

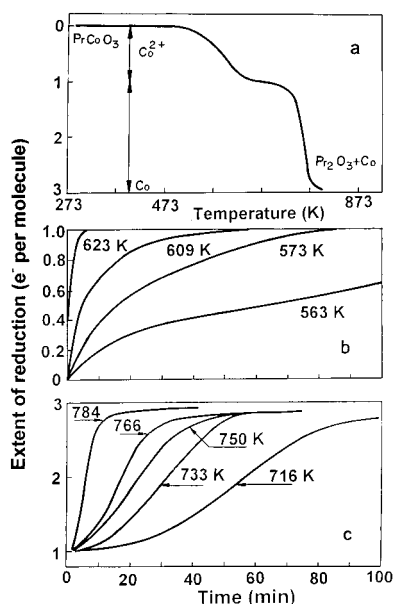


Figure 4. H₂-reduction profiles of PrCoO₃: (a) temperature programmed reduction (4 K/min); (b,c) isothermal reduction in the first (1 e⁻ per molecule) and second (3 e⁻ per molecule) steps, respectively, of diagram (a). Reprinted from ref 119 by permission of the publisher. Copyright 1988 by Chapman & Hall.

a brief account on the differences in oxygen content of the perovskite structure brought about by reduction–oxidation cycles is also given in this section.

1. Kinetics and Mechanisms

Analysis of the reduction profiles of perovskites oxides provides useful information for interpreting the reduction mechanism of these materials. These mechanisms can be studied by recording kinetic data under isothermal conditions. To illustrate this methodology, the temperature-programmed reduction (TPR) profiles of a PrCoO₃ perovskite oxide are shown in Figure 4a.¹¹⁹ The reduction profile shows that the overall reduction $\text{Co}^{3+} \rightarrow \text{Co}^0$ occurs in two steps: (i) reduction of Co^{3+} to Co^{2+} ($\text{PrCoO}_3 + \frac{1}{2}\text{H}_2 \rightarrow \text{PrCoO}_{2.5}$) at temperatures near 660 K and (ii) reduction of Co^{2+} to Co^0 ($\text{PrCoO}_{2.5} + \text{H}_2 \rightarrow \frac{1}{2}\text{Pr}_2\text{O}_3 + \text{Co}^0$) at temperatures about 800 K.

An in-depth analysis of families of kinetic curves of reduction, each one recorded at constant temperature, results extremely valuable to understand the mechanisms involved in the reduction of these mixed oxides. The plot of the reduction degree (α) versus the time of reduction (t) for the first step in Figure 4b shows that the reduction rate decreases continuously with time, indicating that the reduction of the perovskite oxide particles occurs according to the contracting-sphere model. The reduction starts with a very fast nucleation rate, which results in the complete saturation of the grains by a thin layer of the reduced phase after which the rate is attenuated until the bulk reduction is completed. This mechanism implies a continuous drop of the rate of the reduction until the unreduced phase in the core of the grains has been consumed in the reaction. The reduction process can be precisely described by the Mampel's law:¹²⁰

$$1 - (1 - \alpha)^{1/n} = kt + b$$

where α is the reduction degree (if determined by microgravimetry, it is the ratio between the experimental weight change and the theoretical one for a complete reduction); k and b are constants; $n = 2$ corresponds to a two-dimensional growth, and $n = 3$ to a three-dimensional growth of the reduction layer. This equation holds over the middle range of α values.

Kinetic experiments for the deep reduction of Co^{2+} to Co^0 in PrCoO₃ (Figure 4c) within the temperature range from 716 to 784 K showed, as expected, a fast reduction corresponding to the reduction of Co^{3+} to Co^{2+} , which is then followed by a slower reduction. The reduction curves showed a sigmoidal shape for the second reduction step and the extent of reduction corresponds to the quantitative reduction of Co^{2+} into metallic Co^0 ($\text{Co}^{2+} + \text{H}_2 \rightarrow \text{Co}^0$). Thus, the reduction of Co^{2+} to Co^0 is controlled by the formation and growth of metallic reduction nuclei on the surface of the reduced phase in step a (nucleation model). When reduction starts, the rate increases because of the growth of nuclei already formed and the appearance of new ones. Once the surface has become covered by these reduction nuclei, they overlap to a certain extent. Thus, at the inflection point of the curves of reduction both the interface of the oxidized and reduced phases and the rate of reduction begin to decrease. This process can be described by the Avrami–Erofev equation:¹²¹

$$t^n = 1/k[-\ln(1 - \alpha)] \quad (2)$$

where n , k , and α have the same meaning as in eq 2, which holds over α values from 0.05 to 0.95.

For LaNiO₃ perovskite, the kinetic reduction curves were virtually the same as that of PrCoO₃.¹²¹ However, for LaFeO₃ and LaRhO₃ the cation at the B-position is reduced the metal, following the contracting-sphere model. For the substituted LaFe_{1-x}Ni_xO_{3+δ} samples, reducibility was found to depend strongly on x ¹²² (Figure 5a). LaFeO_{3+δ} exhibited oxidativenonstoichiometry, with the principal reduction step associated with the reduction of Fe^{3+} to Fe^0 taking place at temperatures of about 1000 K.²³ There was also a small reduction in the 500–700 K range due to the nonstoichiometry of the oxide (oxygen excess and Fe^{4+}). The oxygen excess ($\delta = 0.05$) was lower than that previously reported for the same perovskite prepared at lower temperature,²³ since δ decreased with the calcination temperature. Substitution with Ni led to a decrease in the reduction temperature, which changed from 1000 K for $x = 1$ to 650 K for $x = 0$ ($\text{Ni}^{2+} \rightarrow \text{Ni}^0$). For the partially substituted ($0.15 \leq x \leq 0.75$) samples, this latter peak overlaps with the reduction of Fe^{3+} into metallic Fe^0 . Additionally, a first reduction step appeared in the range 450–500 K ($\text{Ni}^{3+} \rightarrow \text{Ni}^{2+}$).

The kinetic curves of reduction at three different temperatures (726, 749, and 784 K) for LaFe_{0.1}Ni_{0.9}O₃¹²² are shown in Figure 5b. For the sake of simplicity, only kinetic curves in the temperature region where Ni^{3+} is reduced to Ni^{2+} are included. The sigmoidal shape of these curves indicates that

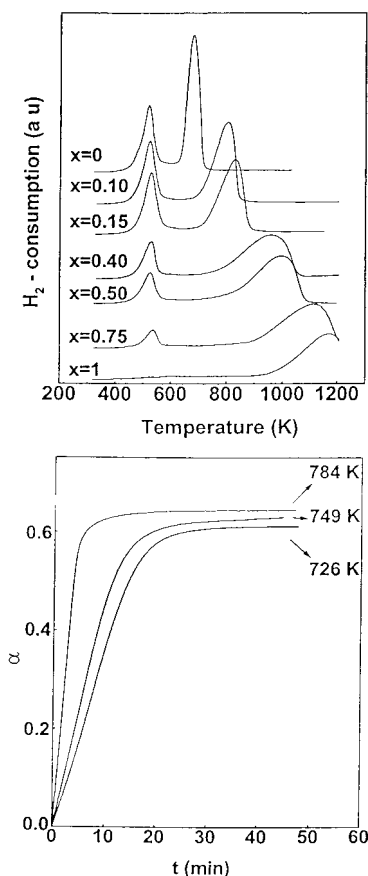


Figure 5. (a) Temperature-programmed reduction (10 K/min) of $\text{LaFe}_x\text{Ni}_{1-x}\text{O}_{3+\delta}$ samples; (b) kinetic curves of reduction at different temperatures for $\text{LaFe}_{0.1}\text{Ni}_{0.9}\text{O}_3$ sample.

the process of reduction can be reasonably described by the shell-type contracting model, which is mathematically described by the Mampel equation (eq 2). The maximum rate of the reduction can be approached to the reciprocal of the time required to achieve a 50% reduction ($r_{\text{max}} \propto 1/t_{0.5}$). Thus, activation energies (E_a) were calculated by means of the Arrhenius plot of $\ln(1/t_{0.5})$ against $1/T$. The E_a values found for the temperature windows of 490–580 K ($\text{Ni}^{3+} \rightarrow \text{Ni}^{2+}$) and 726–784 K ($\text{Ni}^{2+} \rightarrow \text{Ni}^0$) are 103 and 111 kJ mol^{-1} , respectively.¹²²

It should be emphasized here that the distinction of the two reduction mechanisms is somewhat arbitrary because the contracting-sphere model accounts for a rapid nucleation process and the nucleation mechanism ends according to a contracting-sphere model. This observation is illustrated by the close similarity of the shape of the curves of reduction after the inflection point in step b in Figure 4c and in step a in Figure 4b.

2. Reduction–Oxidation Cycles

Perovskite oxides may be reversibly reduced and oxidized at temperatures at which sintering of the reduced or oxidized phases is absent. This is illustrated by LaCoO_3 perovskite. For this sample, reoxidation at 673 K of LaCoO_3 previously reduced to $\text{Co}^0 + \text{La}_2\text{O}_3$ fully restores the perovskite structure. However, the reduced phases $\text{Co}^0 + \text{La}_2\text{O}_3$ heated in an inert atmosphere (He) at 1073 K and reoxidation

as above did not restore the original perovskite phase. Instead, a Co_3O_4 phase was formed.¹⁰² The irreversibility in the redox cycle is mainly caused by the drastic increase in the crystal size of cobalt particles brought about by thermal treatment at high temperatures. A similar increase in Ni^0 metal particle size was observed upon reduction of LaNiO_3 at 703 K followed by heating in He up to 1173 K; this proved to be greater than one order of magnitude.¹²¹ The intermediate reduction products $\text{La}_n\text{Ni}_n\text{O}_{2n+1}$ (Ni^{2+}) and LaNiO_2 (Ni^{+}) were fully oxidized by O_2 at 453 K.¹²³ This result is similar to that observed for the reduction at 773 K of LaCoO_3 to $\text{Co}^0 + \text{La}_2\text{O}_3$ followed by reoxidation with pure O_2 at 673 K.¹⁰² Under these conditions, important amounts of separate phases Co_3O_4 and La_2O_3 as well as LaCoO_3 perovskite were obtained. Formation of the simple oxides of large crystal size may be avoided by carrying out reoxidation of the reduced phases under very mild conditions, e.g., at very low oxidation rate by using highly diluted oxygen (or air) in an inert gas stream as an oxidizing agent. According to this careful operation, the perovskite structure of LaRhO_3 ⁴⁶ and PrCoO_3 ¹¹⁹ samples was completely restored through reversible reduction–oxidation cycles. In these two cases,^{46,119} the crystal size of the regenerated perovskite was found to be even smaller than that seen for the original samples.

These and other examples already mentioned above (LaCoO_3 ¹⁰² and LaNiO_3 ¹²³) show that by reduction treatments or reduction–oxidation cycles, the metal at position B is in a highly dispersed state on a matrix composed of the oxide at position A. Highly dispersed metals have also been obtained by applying reduction–oxidation–reduction cycles to supported metal oxide catalysts.^{124,125} This methodology is nicely illustrated by the work of Kobylinski et al.^{124,125} on the reduction of CoO and NiO phases deposited on ceramic substrates. These authors found that catalyst activation through reduction–oxidation–reduction cycles leads to Co and Ni crystal sizes smaller than that obtained through a single reduction process. Since catalyst activity is associated with the metal phase dispersion, combined reduction–oxidation–reduction cycles may represent a promising pathway for the development of highly dispersed metal catalysts.

C. Ion Mobility

1. Oxygen Transport

Some perovskite oxides are found to be good mixed-conducting materials. Owing to their high electronic and ionic conductivity, they can be used as oxygen semipermeable membranes without electrodes or external circuits.¹²⁶ Teraoka et al.^{127,128} were the first to demonstrate that the oxygen permeation fluxes through the LaCoO_3 -based perovskites membranes were 2–4 orders of magnitude higher than those of the stabilized zirconia (YSZ) at the same temperatures. Ceramic membranes of perovskite-related oxide phases $\text{La}(\text{Sr})\text{Co}(\text{Fe})\text{O}_{3-\delta}$ were used successfully in several external conditions.^{129–131} The highest oxygen permeation fluxes are characteristic of

$\text{SrCo}_{1-x}\text{Fe}_x\text{O}_{3-\delta}$ solid solutions at $0.3 \geq x \geq 0.2$. For the most $\text{SrCoO}_{3-\delta}$ -based perovskites, oxygen permeability is limited by both bulk ionic transport and rate of oxygen exchange between the oxides and the gas phase.^{132,133} It was found that an increase in oxygen nonstoichiometry results in decreasing electrical conductivity and oxygen permeability. This effect was observed when cobalt was substituted with lower valence cations in $\text{SrCo}(\text{M})\text{O}_{3-\delta}$ ($\text{M} = \text{Ni}, \text{Cu}$) oxide systems.^{134,135} Conversely, the introduction of copper into the cobalt sublattice of $\text{SrCo}(\text{Fe}, \text{Cu})\text{O}_{3-\delta}$ considerably improved the sinterability and mechanical strength of strontium cobaltites/ferrites.¹³⁵

As stated above, Co- or Fe-based perovskites have mainly been investigated as mixed electronic-oxide ionic conductors.¹³⁶ However, these oxides are easily reduced in a reducing atmosphere, resulting in the formation of cracks.¹³⁷ Recently, Ishihara et al.¹³⁸ found that LaGaO_3 -based perovskite doped with a transition metal cation at the Ga site is effective for increasing the conductivity of the oxide ion and also the oxygen permeation rate. In particular, for $\text{Sr}_{0.2}\text{La}_{0.8}\text{Ga}_{1-x}\text{Ni}_x\text{O}_3$, the oxygen permeation rate increased with increasing Ni-contents and reached a maximum at $x = 0.25$ at all temperatures. The oxygen permeation rate of this sample of $2.2 \text{ mL cm}^{-2} \text{ min}^{-1}$ at 1273 K is substantially higher than the permeation rate of $\text{Sr}_{0.4}\text{La}_{0.6}\text{Fe}_{0.8}\text{Co}_{0.2}\text{O}_3$ at the same temperature ($1.5 \text{ mL cm}^{-2} \text{ min}^{-1}$),¹³⁷ which is considered to be a promising mixed ion conductor for oxygen separation. The improved oxygen permeation rate of the Ni-doped LaGaO_3 perovskite is also accompanied by a stable conductivity and the absence of Ni reduction in a reducing environment.

The size of the A and B cations in the ABO_3 perovskite structure is an important factor for high ion conductivity. Using defined potentials, Cherry et al.¹³⁹ calculated the migration energies of the vacancy jump for a range of A and B cation radii. The results indicated two main points. First, the calculations exhibited a clear trend toward lower migration energies with smaller A-site cations. There was an optimum value of about 0.095 nm , below which the migration energy rose steeply. Second, there was a decrease in energy with increasing size of the B cation, with a minimum at 0.075 nm . To assess these results, the relationship between the tolerance factor (t) was also established.¹⁴⁰ The calculations suggested that perovskites with $t \approx 0.81$ may lead to lower migration energies and faster diffusion, a result with practical consequences for oxidation catalysis and for operating fuel cells at lower temperatures and at higher rates. Moreover, this value of the tolerance factor (t) would encompass several perovskite electrolytes, such as PrMnO_3 and GdMnO_3 . These findings can be rationalized in terms of lattice relaxation effects. As the mobile oxygen approaches the saddle point, it must pass through the center of a triangle of cations. Calculations have shown that the repulsive overlap interactions can be reduced by the outward relaxation of these cations. It appears that the minimum in t values corresponds to the most effective balance of the relaxation of the A and B

cations at the saddle point position. In other words, the even distribution of relaxation between the cations is an important factor for the low energy barriers to oxygen ion migration.

It has been widely documented that the incorporation of dopant ions to the LaMO_3 oxides is crucial for promoting catalytic activity and high ion conductivity.^{140–144} These oxides are commonly acceptor-doped with low-valent cations (e.g., Sr^{2+}), which substitute La^{3+} . This reduction of the effective valence of A-site cations leads to the formation of a compensating population of oxygen vacancies at low oxygen partial pressure, which in turn gives rise to the observed high ionic conductivity.

The energy of the resulting solution reaction ($\text{LaBO}_3 + \text{MO} \rightarrow \text{M}_x\text{La}_{1-x}\text{O}_{3-\delta}$, $\text{M} = \text{alkaline earth element}$) can be evaluated theoretically by combining appropriate defect and lattice energy terms.¹⁴⁵ The results revealed that the most favorable solution energy and hence the highest solubility is expected for Sr^{2+} in all the LaBO_3 hosts. The solution energy was found to be a minimum at Sr^{2+} (close to the La^{3+} radius of 0.106 nm). This agrees with experimental studies demonstrating that the incorporation of Sr, and to a lesser extent Ca, results in an increase in the oxygen diffusion coefficient and to high catalytic activity in oxidation reactions. Theoretical calculations also showed that the solution of MgO and BaO is somewhat endothermic, in keeping with the observed low solubility.

Information about the fundamental mechanistic features and migration activation energies is limited. It is generally accepted that oxygen diffusion is based on rapid transport of vacancies, which migrate by a conventional hopping mechanism, although there is no experimental evidence to support this. These factors were analyzed by looking at the potential energy surface.¹³⁹ The surface energy maps were constructed by calculating the defect energy of the migration ion along the diffusion path and allowing relaxation of the lattice at each position. According to this calculation, the results confirmed the migration of oxygen ion vacancies as the lowest energy path. The calculated migration activation energy for LaMnO_3 was 0.86 eV , in agreement with the value of 0.73 eV reported by Belzner et al.¹⁴⁶ Similarly, the activation energy for LaCoO_3 was 0.61 eV , which is in good agreement with the experimental value measured by Carter et al.¹⁴⁷ The location of ions and the available space in the perovskite lattice suggest that interstitial diffusion is unlikely. This is corroborated by the high-energy barriers ($>1.5 \text{ eV}$) calculated for the interstitial migration. Therefore, the ion diffusion in perovskite-type LaBO_3 comes from the mobility of oxygen ion vacancies.

2. Cation Transport

Despite the extensive work devoted to oxygen transport, little efforts have been devoted to investigating cation diffusion in perovskite oxides. Cation mobility plays an important role not only in the processing steps, but also in their operation and degradation. Thus, it is believed that in membrane perovskites cation mobilities occur in such a way that

the high oxygen pressure side favors enrichment with the fast moving of cations.¹⁴⁸

For manganites, lanthanum diffusion is likely to take place by vacancy migration between neighboring sites. The values of the activation energies for this La vacancy mechanism calculated by Islam¹⁴⁹ indicate a value of 3.93 eV for the cubic structure with a clear trend toward higher energies as the perovskite lattice becomes more distorted from the cubic structure. This fact is associated with the Mn–O–Mn bending and MnO₆ octahedra tilting. The calculations reveal a correlation between the shortest O–O separation across the octahedral interstice and the activation energy for La migration.¹⁴⁹ As expected, this activation energy increases as the O–O distance decreases. It should be stressed that the predicted value for the vacancy mechanism is consistent with the calculated activation energy of 4.70 eV for LaGaO₃¹⁵⁰ and the experimental value of 4.98 eV for La diffusion in the solid-oxide electrolyte fuel cell interconnect LaCrO₃ perovskite.¹⁵¹

The calculated migration energies for Mn migration are extremely high, lying around 14 eV, although in this case the perovskite distortion does not alter the energy barrier.¹⁴⁹ Working on Sr-substituted manganites, Sr_xLa_{1-x}MnO_{3+δ}, Wofenstine et al.¹⁵⁰ calculated activation energies on the order of 4–5 eV for bulk self-diffusion, although these authors were unable to assign these values to a given cation diffusion. By modeling cation transport in Ca- and Sr-substituted manganites, in which the divalent dopant cations are compensated by electron holes (Mn⁴⁺ sites), it was found that the migration energies decrease in the order La > Sr > Ca.¹⁴⁹ This trend is, in principle, unexpected because the ionic radius of La³⁺ lies between that of Sr²⁺ and Ca²⁺. It can be explained assuming that electrostatic and ion polarizability factors, as well as steric hindrance at the saddle point, are important.

Recently, perovskite oxides have received great deal of attention as high-temperature proton conductors with promising applications in several fields such as hydrogen sensors, fuel cells, and electrolyzers.¹⁵² The best studied perovskites for this purpose are A²⁺B⁴⁺O₃, particularly ACeO₃ (A = Sr, Ba)^{153,154} and AZrO₃ (A = Ca, Sr),¹⁵⁵ with only a few studies on A³⁺B³⁺O₃ oxides.¹⁵⁶ As revealed by isotope effect (H+/D+) analysis of perovskite oxides, the conduction mechanism is due to proton hopping between adjacent oxygen ions, rather than by hydroxyl ion migration. Proton jump involves quantum effects (tunneling) and cooperative motions of the structure (lattice phonons), both leading to modulations of O–O distance. Using ab initio Hartree–Fock techniques, Cherry et al.¹³⁹ studied the proton-transfer process and calculated energy barriers for proton conductivities of less than 0.2 eV, which are 2–3 times lower than that observed in perovskite oxides.^{153–156} It should be emphasized that these calculations yield the energy and geometry of the ground and barrier state configurations. However, they provide no information concerning the relaxation of the surrounding lattice, which would accompany the proton migration.

IV. Heterogeneous Catalysis

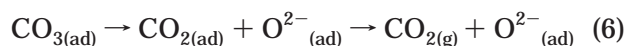
A. Oxidation Reactions

1. CO Oxidation

The oxidation of CO over perovskite oxides was taken as a probe reaction on a number of perovskite oxides with the aim of correlating the observed activity with electronic state of the transition metal ions or the defect chemistry of these compounds.^{104,157} In LnBO₃ (Ln = lanthanide) perovskites, the Ln³⁺ ions are essentially inactive in catalysis and the active M³⁺ transition metal ions are located at relatively large distances from each other (around 0.4 nm), which make them excellent catalytic models for study the interactions of CO and O₂ on single surface sites.

The first study on the CO oxidation on perovskite oxides was carried out by Parravano in the early 50s.¹⁵⁸ Later on, Kawai et al.¹¹⁵ observed a discontinuity in the activation energy for the oxidation of CO with O₂ or N₂O on BaTiO₃ ferroelectrics near the Curie temperature (*T*_c = 393 K) of this catalyst. The reaction rate is very slow in the temperature range from 373 to 473 K and under steady-state conditions is limited by the rate of the desorption of CO₂. Both facts were taken as conclusive that the oxidation reaction proceeds via surface defects. Many other perovskite oxides have been proposed and used in CO oxidation. Looking at most of the works discussed in our previous review,¹⁰⁴ it is apparent that CO oxidation over perovskites proceeds according to a suprafacial process, in which the electronic band structure near the Fermi level is believed to play a key role.^{104,159} Thus, for the LaBO₃ (B is transition atom from V to Ni) perovskite series, LaCoO₃ proved to be the one most active^{159–163} and LaCrO₃ among the least active for CO oxidation.^{164,165}

On the basis of kinetic and spectroscopic data, Tascon et al.¹⁶⁶ proposed a simple reaction mechanism for CO oxidation on LaCoO₃:



where eq 6 should be the rate-determining step. Oxygen is adsorbed as molecular O₂[−] species on Co²⁺ ions, which subsequently dissociates yielding atomic oxygen (O[−]) adsorbed on the same site. On the other hand, CO adsorbs on surface oxide ions, leading to a labile species that interacts with adsorbed atomic oxygen, producing a carbonate structure that then decomposes to afford adsorbed CO₂ and oxygen.

LaCuO_{3-δ} (δ = 0.05–0.45) perovskites offer a useful model catalyst system in which the concentration of oxygen vacancies can be gradually changed by controlled annealing under high oxygen pressures at temperatures from 1073 to 1273 K.¹⁶⁷ These defect structures were carefully characterized using the

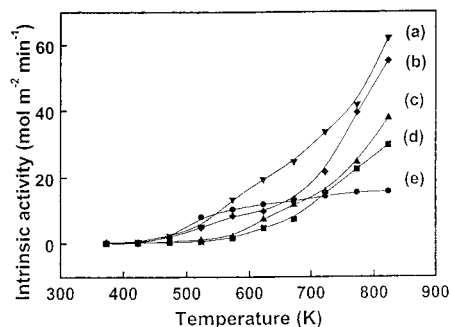


Figure 6. Temperature dependence of the intrinsic activity in the catalytic CO oxidation on $\text{LaCuO}_{3-\delta}$ catalysts: (a) $\text{LaCuO}_{2.55}$; (b) $\text{LaCuO}_{2.65}$; (c) $\text{LaCuO}_{2.73}$; (d) $\text{LaCuO}_{2.95}$; and (e) La_2CuO_4 .

Rietveld method and photoelectron spectroscopy and were then tested in the catalytic oxidation of CO under flow conditions. Stationary-state activity data of the $\text{LaCuO}_{3-\delta}$ systems, expressed as moles of CO converted per square meter and per minute, as a function of temperature, are shown in Figure 6. Although all the samples display measurable activity at 423 K, differences among them become apparent at higher temperatures. The orthorhombic sample $\text{LaCuO}_{2.55}$ shows the strongest activity; its monoclinic counterpart $\text{LaCuO}_{2.65}$ is less active, and the tetragonal samples $\text{LaCuO}_{2.73}$ and $\text{LaCuO}_{2.95}$ exhibit still lower activity. Catalytic activity in CO oxidation is largely controlled by the number of oxygen vacancies present in the crystal structure. The almost stoichiometric tetragonal $\text{LaCuO}_{2.95}$ perovskite, with 90% Cu^{3+} , exhibits a moderate activity well below that of the most nonstoichiometric compound ($\text{LaCuO}_{2.55}$) with only 10% Cu^{3+} irrespective of the temperature range considered. As has been observed in the series of superconducting materials of the $\text{YBa}_2\text{Cu}_3\text{O}_{7-\delta}$ family, the oxygen vacancies seem to be responsible for this reaction.⁵¹ The thermal decomposition under reducing conditions of the orthorhombic $\text{LaCuO}_{2.55}$ phases at temperatures significantly lower than the remaining $\text{LaCuO}_{3-\delta}$ phases¹⁶⁷ suggests that the activity is also related to the ease of oxygen removal, either from the adsorbed state or from the lattice, as observed in $\text{LaCoO}_{3-\delta}$ series.¹⁶⁸

A strong enhancement in the catalytic activity for CO oxidation has recently been reported on hole doped $\text{Ln}_{1-x}\text{Sr}_x\text{NiO}_3$ ($\text{Ln} = \text{Pr}, \text{Sm}, \text{Eu}$) perovskites.¹⁶⁹ Figure 7 shows the influence of reaction temperature on the intrinsic activity for CO oxidation. To normalize differences in the specific areas of the $\text{Sr}_x\text{Ln}_{1-x}\text{NiO}_3$ samples, activity was expressed here as intrinsic activity, which represents the number of moles of CO converted per square meter of catalyst and unit time. As expected for the three series of perovskites, intrinsic activities increased with the reaction temperature. In addition, the Sr-substituted samples were more active than the respective undoped LnNiO_3 counterparts. However, the effect of Sr-substitution was much more marked in $\text{Pr}_{0.95}\text{Sr}_{0.05}\text{NiO}_3$, in which activity was nearly 3-fold activity of the unsubstituted PrNiO_3 sample. Sr-substitution had a less marked effect in $\text{Sm}_{0.90}\text{Sr}_{0.10}\text{NiO}_3$ and even less effect in the $\text{Eu}_{0.99}\text{Sr}_{0.01}\text{NiO}_3$ sample. Since the hole-doped samples underwent the first reduction process

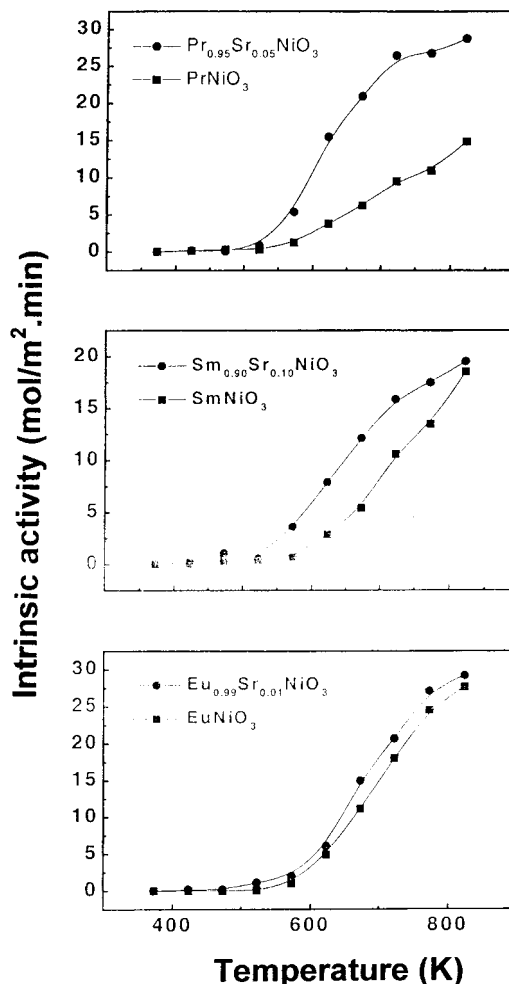


Figure 7. Temperature dependence of the intrinsic activity in the catalytic CO oxidation on $\text{Ln}_{1-x}\text{Sr}_x\text{NiO}_3$ ($\text{Ln} = \text{Pr}, \text{Sm}, \text{and Eu}$).

at lower temperatures than the respective undoped compounds, activity is related to the ease of oxygen removal. The reduction temperature decreases when the Ni valence is enhanced using a suitable Ln partner in the crystal lattice. The larger the Ln^{3+} cation, the higher is its basic character, and the more enhanced is the actual valence for Ni. For $\text{Pr}_{0.95}\text{Sr}_{0.05}\text{NiO}_3$ sample, the formal valence of Ni is +3.05, which results in a shorter Ni–O bond, and therefore reduced at lower temperatures.¹⁶⁹ Thus, the lattice oxygens are more labile and can participate more easily in the external redox process, as depicted by eqs 4–7.

2. Oxidation of Hydrocarbons

The reports by Libby¹⁷⁰ and Pedersen and Libby¹⁷¹ in the early 70s opened the possibility of using perovskite oxides for the oxidation of hydrocarbons. Following this, the large body of work ensued solid arguments to explain the catalytic performance of these materials in terms of the relative ease with which oxygen species can be released from the surface. The oxidation of paraffins,^{172–190} olefins,^{49,52} aromatics,^{185–187} and oxygenate compounds^{53,185,188–193} are the most representative examples.

The combustion of methane over perovskite oxides has been extensively investigated, particularly in

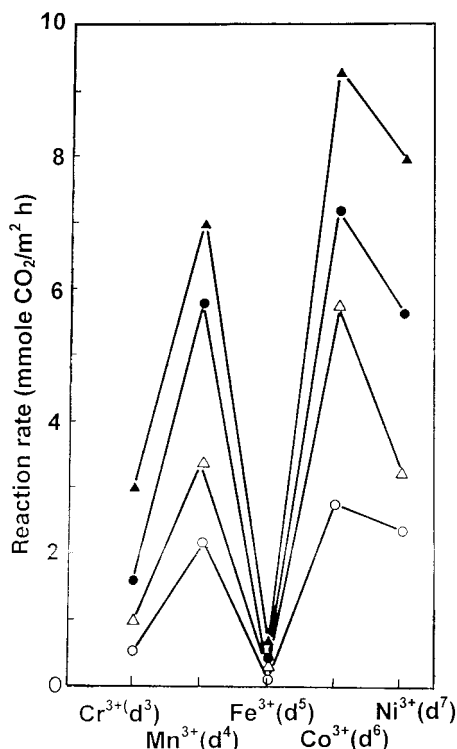


Figure 8. Rates of propylene (open symbols) and isobutene (filled symbols) oxidations on LaMO_3 oxides at 573 K. Molar ratio $\text{HC}:\text{O}_2 = 0.25:1$ (circles) or $2:1$ (triangles). Reprinted from ref 49 by permission of the publisher, Copyright 1985 by The Royal Society.

recent years (see below). The performance of these compounds for the combustion of other long chain hydrocarbons has also been examined. Thus, Nakamura et al.⁵¹ and Nitadori and Misono⁵⁴ studied propane combustion on Sr- or Ce-substituted LaMO_3 ($M = \text{Fe}, \text{Co}$) perovskites. The activity of $\text{La}_{1-x}\text{Sr}_x\text{MnO}_3$ varied in a parallel way to the reducibility of the catalyst surface, the amount of reversibly adsorbed oxygen, and the rate of isotopic equilibration of oxygen. Since all these properties are related to the surface oxygen, it can be inferred that the catalytic activity is controlled by the nonstoichiometric character of the surface. In another contribution, Kremenec et al.⁴⁹ studied the combustion of propylene and isobutene at 573 K on LaBO_3 ($B = \text{Cr}, \text{Mn}, \text{Fe}, \text{Co}, \text{Ni}$) oxides and found the rates of isobutene combustion to be higher than those of propylene. In both cases, a twin peak pattern with maxima for Mn and Co was observed (Figure 8), matched with that obtained upon oxygen adsorption on the perovskites. Finally, the close parallelism between O_2 adsorption and catalytic activity in the combustion of propylene and i-butene suggests that these reactions occur through a suprafacial mechanism, in which adsorbed oxygen is the dominant species participating in the reaction.

a. Methane Combustion. Perovskite-type oxides show particular promise for the combustion of methane (or natural gas) owing to their good stability, at least below 1300 K, and high catalytic activity. Arai et al.¹⁷² studied the catalytic combustion of methane over LaBO_3 ($B = \text{transition element}$) and Sr-substituted $\text{La}_{1-x}\text{Sr}_x\text{BO}_3$ ($0 < x < 0.4$) perovskites. Particularly, the Sr-substituted manganites, cobaltites, and

ferrites exhibited very high oxidation activities comparable with the activity of a $\text{Pt}/\text{Al}_2\text{O}_3$ combustion catalyst.¹⁷² High catalytic activities for methane combustion over perovskite oxides were also reported by McCarty and Wise.¹⁴¹ An interesting characteristic of these perovskites is the possibility of varying the dimensions of the unit cell by substitution of the A ion, and thereby the covalency of the B–O bond in the ABO_3 structure. Moreover, partial substitution at the A-site can strongly affect catalytic activity due to stabilization of unusual oxidation states of the B component and to the simultaneous formation of structural defects. Structural defects are responsible not only for part of the catalytic activity, but also for oxygen mobility within the crystal lattice, due to the nonstoichiometry created by substituting the A-site. An overview of these aspects as well as the implications in methane combustion have been compiled in our previous reviews.^{4,104}

In a recent contribution, Ferri and Forni⁵⁵ demonstrated that the type of substitution at the A-site in families of $\text{La}_{1-x}\text{A}'_x\text{BO}_3$ ($B = \text{Co}, \text{Fe}, \text{Ni}$) oxides has a strong influence on methane combustion. Substitution at the A-site with a bivalent cation ($\text{A}' = \text{Sr}, \text{Eu}$) or a tetravalent cation ($\text{A}' = \text{Ce}$) led to a decrease or an increase, respectively, of methane combustion activity. The Eu- or Sr-substitution for La leads to higher oxidation states for Co, so that the higher the amount of Sr, the higher is the concentration of Co^{4+} . However, since Co^{4+} is unstable, then oxygen release can take place ending in the formation of oxygen vacancies. By contrast, insertion of Ce^{4+} leads to a partial reduction of the Co^{3+} to Co^{2+} , thus affording a large amount of active sites for oxygen adsorption from gas-phase. Consistent with these observations, O_2 TPD patterns revealed a high-temperature peak, attributed to structural lattice oxygen, and a low-temperature peak corresponding to oxygen originated by the reduction process involving the B-site cation and the formation of anion vacancies. At low temperatures, methane combustion on these catalysts is a suprafacial reaction¹⁹⁴ involving oxygen coming from the gas phase or sitting in the oxygen vacancies of the catalyst.¹⁶⁰ In fact, at low temperature methane combustion rate is of zero order with respect to the oxygen partial pressure due to a rapid incorporation of gaseous oxygen into the lattice:

$$r = k_1 P_{\text{CH}_4} \quad (7)$$

where k_1 is the specific rate constant and P_{CH_4} is the methane partial pressure. However, at high-temperature methane reacts with the oxygen supplied by the catalyst and coming from the bulk (intrafacial mechanism).¹⁹⁴ On the basis of these considerations, the overall rate of CH_4 combustion throughout the whole temperature range can be described by the sum of two parallel reactions.

$$r = \frac{K_2 P_{\text{CH}_4} (K_{\text{O}_2} P_{\text{O}_2})^{1/2}}{1 + (K_{\text{O}_2} P_{\text{O}_2})^{1/2}} + k_1 P_{\text{CH}_4} \quad (8)$$

where P_{O_2} and K_{O_2} are the partial pressure and adsorption constant for oxygen. At high tempera-

tures, the reaction rate can be expressed simply as $r = K_a P_{\text{CH}_4} (K_{\text{O}_2} P_{\text{O}_2})^{1/2}$, if the oxygen coverage is small ($1 \gg (K_{\text{O}_2} P_{\text{O}_2})^{1/2}$). Equation 9 will thus be:

$$r = K_a P_{\text{CH}_4} (K_{\text{O}_2} P_{\text{O}_2})^{1/2} + K_1 P_{\text{CH}_4} \quad (9)$$

The contribution of each oxygen species to the overall rate can be estimated separately by plotting the experimental rate r vs $P_{\text{O}_2}^{1/2}$.⁵⁷ The intercepts of the straight lines ($P_{\text{O}_2} = 0$) represent the contribution of lattice oxygen, which is expected to increase with increasing reaction temperature. These considerations are consistent with the simultaneous participation of suprafacial and intrafacial processes during hydrocarbon oxidations taking place at low and high temperatures, respectively, on perovskite oxides.^{104,159}

Monolith perovskites prepared from ultradispersed powders of mixed oxides of rare earths (La-Ce or Dy-Y) and transition metals (Ni, Fe, Mn) have recently been used in methane combustion.⁹¹ These preshaped structures were seen to be active and selective in the target reaction over a wide range of temperatures. The scale of the specific activity and apparent activation energy for monoliths paralleled that found for powder samples. The catalyst decreased the ignition temperature, up to 200 K for the temperature required to achieve a 10% methane conversion, and enhanced the selectivity to CO_2 with respect to the uncatalyzed process.

b. Oxidative Coupling of Methane. Elshof et al.¹⁹⁵ studied the oxidative coupling of methane on a $\text{La}_{0.6}\text{Sr}_{0.4}\text{Co}_{0.8}\text{Fe}_{0.2}\text{O}_3$ membrane using O_2 partial pressures between 0.01 and 1 bar. Methane was converted to C_2H_6 and C_2H_4 with selectivities of up to 70% but at conversion levels of only about 1–3%. An important requirement for the reaction is that the O_2 flux should be limited by exchange kinetics, because otherwise reduction of the membrane would occur, with the subsequent decrease in C_2 selectivity. The same reaction was studied in a membrane reactor with $\text{BaCe}_{0.8}\text{Gd}_{0.2}\text{O}_{3-\delta}$,¹⁹⁶ which is a mixed oxide ion–electron hole conductor. By passing CH_4 over one side of the membrane and O_2 over the other side, reasonable conversions of methane were obtained, with much greater selectivity than when both CH_4 and O_2 were fed to the same side of the membrane. This means that the O species released from the membrane at the CH_4 side is more active for C_2 formation than gaseous O_2 . By considering both the surface reactions on the membrane–gas interface and the diffusion of the different charged species in the solid, equations for the transport of oxygen through thin mixed conducting membranes were derived.¹⁹⁷ The calculations show that the use of highly permeable ceramic membranes with a catalytically active surface for the coupling reaction affords one the possibility of achieving much higher C_2 yields than with a packed-bed reactor. The high C_2 yield can only be attained when the oxygen flux, the CH_4 flow rate, and the intrinsic reaction rate match each other.

Other perovskite membranes display proton conductivity when exposed to a H-containing atmosphere at high temperatures. Iwahara et al.^{198,199} discussed the application to steam electrolysis to produce H_2

gas on proton conductive MCeO_3 ($\text{M} = \text{Sr}, \text{Ba}$) perovskites. In particular, the Nd-doped BaCeO_3 material shows significantly higher proton conduction in wet air than SrCeO_3 . This oxide was used as a solid electrolyte in a steam electrolyzer producing H_2 and in a H_2 /air fuel cell. In the latter case, the resistance of the solid electrolyte was the main factor limiting cell performance. Hamakawa et al.²⁰⁰ reported data on CH_4 coupling using $\text{SrCe}_{0.95}\text{Yb}_{0.05}\text{O}_{3-\delta}$ (SCYO) as a solid electrolyte in an electrochemical cell. Because there is no gaseous O_2 , which is responsible for the combustion reaction, this may lead to a much better C_2 -selectivity than can be obtained with the conventional catalytic process. Chiang et al.²⁰¹ also investigated the dehydrogenative dimerization of methane using SCYO proton-conducting membranes and proposed that the rate-determining step is the formation of a $\text{CH}_3\cdot$ radical by proton abstraction. Comparison of the activity data using different reactors for this reaction indicates that the SCYO membrane reactor affords a substantially larger yield than the corresponding conventional catalytic reactor.²⁰² The experimental results clearly show that the equilibrium conversion of the dehydrogenation reaction can be dramatically changed by using a proton-conducting membrane in an electrochemical reactor cell.

c. Partial Oxidation of Methane. Several perovskite oxides have been studied as catalysts for the partial oxidation of methane to syngas ($\text{CH}_4 + 1/2\text{O}_2 \rightarrow \text{CO} + 2\text{H}_2$).^{105,203–205} Slagtern and Olsbye²⁰³ reported the in situ formation and high activity of metal species for synthesis gas production on LaBO_3 ($\text{B} = \text{Rh}, \text{Ni}, \text{Co}$) perovskites, where the perovskite structure decomposed during the reaction. The best system, LaRhO_3 , displayed high activity at 1073 K for long times on stream (120 h), and exhibited good dispersion of Rh particles on the La_2O_3 phase, while both LaNiO_3 and LaCoO_3 were deactivated, probably due to coke formation during the reaction. In the series of $\text{Ca}_{0.8}\text{Sr}_{0.2}\text{Ti}_{1-y}\text{Ni}_y\text{O}_3$, Hayakawa et al.²⁰⁵ reported that the catalyst with a composition of $y > 0.1$ shows high activity for CH_4 combustion at temperatures around 873 K but suddenly changes to synthesis gas formation at 1073 K. An increase in y results in high activity for CH_4 combustion, and the highest selectivity to synthesis gas at 1073 K is obtained with catalyst $y = 0.2$. Under the conditions of synthesis gas formation, the overall reaction appears to occur through two consecutive processes: the first part of the catalyst bed catalyzes CH_4 combustion under the O_2 -rich atmosphere, and the second part of the bed catalyzes CH_4 reforming with the H_2O and CO_2 produced in the first part, under the O_2 -deficient atmosphere. Either Ni species in the perovskite structure or the NiO phase originally separated from the perovskite structure during catalyst preparation is easily reduced to Ni^0 under the O_2 -deficient environment at high temperature, and the Ni metal thus formed in the second zone shows high activity for synthesis gas formation.

Lago et al.¹⁰⁵ investigated a series of LnCoO_3 ($\text{Ln} = \text{La}, \text{Pr}, \text{Nd}, \text{Sm}, \text{Gd}$) perovskites as catalyst precursors for the partial oxidation of methane to

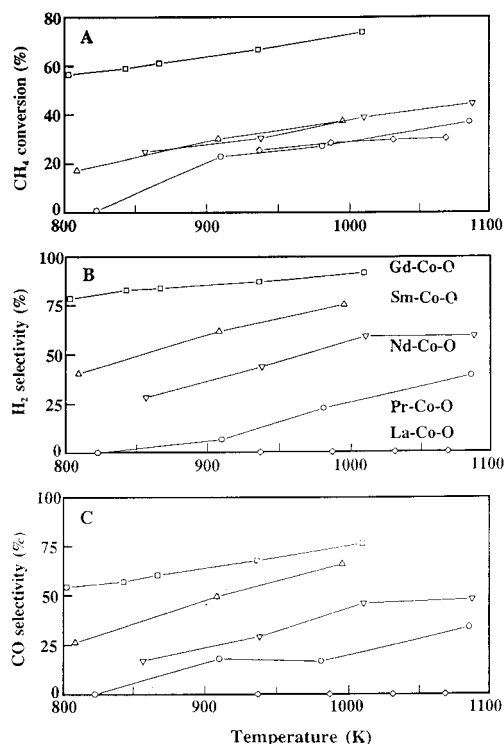
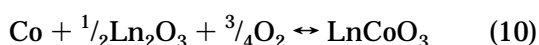


Figure 9. (A) Methane conversion; (B) H₂; and (C) CO selectivity in the presence of LnCoO₃ systems prereduced at 1023 K.

synthesis gas. Among these compounds, the Gd-Co-O system showed exceptional performance for synthesis gas formation (Figures 9A–C). At 1009 K, a steady-state CH₄ conversion of 73%, with selectivities of 79 and 81% for CO and H₂, respectively, was observed for the catalyst Gd-Co-O. The less active Nd-Co-O and Sm-Co-O catalysts afford a similar steady-state CH₄ conversion within the temperature range studied. The catalyst La-Co-O is active for CH₄ combustion, and only traces of H₂ and CO were observed under the reaction conditions used. It was observed that at constant temperature the steady-state yields of H₂ and CO inversely followed the order of the ionic radii of the rare earth, considering the oxidation state +3, coordination number 8, and the sexquioxides of structural type A for La₂O₃, Pr₂O₃, and Nd₂O₃ and type B for Sm₂O₃ and Gd₂O₃.¹⁰⁵ Thus, gadolinium, which has the shortest ionic radius, exhibits the highest CO and H₂ yields and contrasts with the La-containing catalyst (the largest ion), in which no syngas was observed.

The nature of the Ln affects the reducibility of Co in the LnCoO₃ perovskites.¹⁰⁵ The Goldschmidt tolerance factor *t* obtained for these systems indicates that, considering only geometric factors, lanthanum, which is the largest ion in the series, forms the most stable perovskite structure. This trend is reflected in the reduction profiles, where the LaCoO₃ perovskite, the most stable structure, is reduced at the higher temperature (Figure 10). Likewise, the oxidation profiles obtained on the H₂-reduced perovskites



showed that reoxidation of cobalt to form the perovskite structure is more favorable for larger lan-

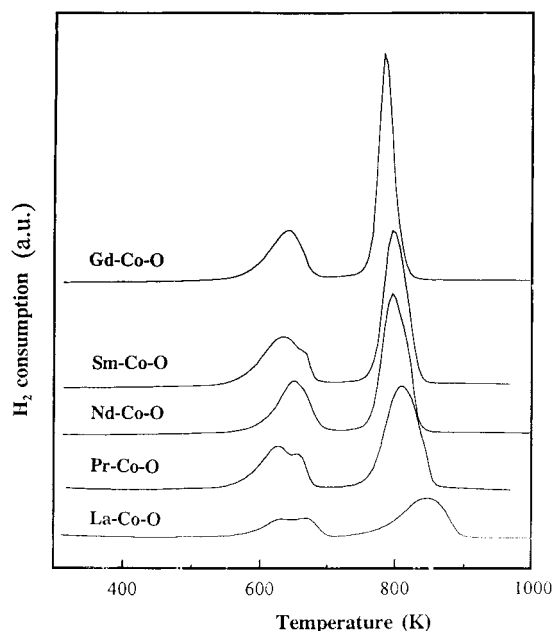


Figure 10. Temperature-programmed (10 K/min) reduction profiles of LnCoO₃ perovskite oxide precursors.

thanides. This finding agrees with the thermodynamic calculations made by Katsura et al.⁹⁸ for the oxidation of iron to the rare earth perovskite between 1473 and 1673 K, who showed that reoxidation to form the perovskite is favored in the order La > Nd > Sm > Gd, with standard Gibbs energies of −288.0, −274.6, −267.9, and −263.7 kJ mol^{−1}, respectively. Accordingly, deactivation of these catalysts derived from perovskite structures appears to be related to the reoxidation of the active metal phase during the syngas reaction and the subsequent solid-state reaction with the lanthanide oxide (M₂O₃ + Ln₂O₃ → LnMO₃) to regenerate the original perovskite phase.

Internal reforming reaction of methane and oxygen (or air) in a solid oxide electrolyte fuel cell was investigated by Yamada et al.²⁰⁶ These authors reported that large electric power as well as syngas (CO + H₂) mixtures can be obtained by using LaGaO₃ perovskite as solid electrolyte. It was found that doping of a small amount of cobalt for electrolyte is effective in increasing the power density and the yield of CO and H₂. In particular, the optimized composition La_{0.9}Sr_{0.1}Ga_{0.8}Mg_{0.115}Co_{0.085}O₃ for the electrolyte afforded power density and yield of CO and H₂ of 242 mW cm^{−2} and 16%, respectively, at 1073 K. Considering that the thickness of electrolyte was 0.5 mm and small Gibbs free energy change for the partial oxidation of methane into CO and H₂, power generation characteristics of the cell was even superior. Since the decrease in power density was not significant when air is used as oxidant instead of oxygen, the internal reforming fuel cell is attractive not only from the standpoint of upgrading natural gas but also from separation of air.

The reforming of methane using carbon dioxide as an oxidant agent (dry reforming) (CH₄ + CO₂ → 2CO + 2H₂) has also been investigated on Ni-based perovskites.^{207–209} La_{1−x}Sr_xNiO₃ (*x* = 0–0.1) and La_{2−x}Sr_xNiO₄ (*x* = 0–1.0) perovskite series displayed

different performances in the dry reforming of CH_4 .⁹⁸ LaNiO_3 shows high activity without coke formation while La_2NiO_4 is inactive. Among the Sr-substituted perovskites, $\text{La}_{0.9}\text{Sr}_{0.1}\text{NiO}_3$ and $\text{La}_{1.8}\text{Sr}_{0.2}\text{NiO}_4$ display the highest activity, with coke formation on the surface. Initially, the catalytic activity increases with time and then reaches steady state. Such an increase in catalyst performance is associated with the transformation of the original perovskite into $\text{La}_2\text{O}_2\text{CO}_3$ and SrCO_3 with highly dispersed Ni metal particles due to the H_2 generated in the reaction. The enhanced catalytic activity of Sr-substituted perovskite could come from dual sites: La_2O_3 for CO_2 adsorption and Ni^0 for CH_4 activation.

Perovskite membranes have also been studied for the partial oxidation of methane to syngas.^{210–215} Tubular $\text{La}_{0.2}\text{Sr}_{0.8}\text{Fe}_{0.6}\text{Co}_{0.4}\text{O}_{3-\delta}$ membranes coated on the inside of the tube with an Rh reforming catalyst were used in syngas production.²¹⁰ At 1023 K, CH_4 conversion reaches levels above 98%, with a CO selectivity of about 90% and an H_2 yield almost twice the CO yield. Since this perovskite is highly active in CH_4 combustion, the overall reaction might proceed in such a way that the total combustion of CH_4 occurs ($\text{CH}_4 + 2\text{O}_2 \rightarrow \text{CO}_2 + 2\text{H}_2\text{O}$), followed by a reforming reaction ($2\text{CH}_4 + \text{CO}_2 + \text{H}_2\text{O} \rightarrow 3\text{CO} + 5\text{H}_2$) on the Rh-coated reforming catalyst. Another group of materials investigated is based on a composition in the $\text{Sr}_4(\text{Fe}_{6-x}\text{Co}_x)\text{O}_{13+\delta}$ region. These compounds are not simple perovskites because the B/A ratio is larger than 1 (in the perovskite ABO_3 it is 1). These are layered compounds, which combine high electronic/ionic conductivity with an appreciable oxygen permeability. Dense membranes of these materials can be used to separate high purity oxygen from air and also to partially oxidize CH_4 to synthesis gas, without the need of an external electrical circuit.

Mixed oxygen anion- and electron-conducting membranes derived from the brownmillerite structures have also been used for the same purpose.²¹⁶ This structure has the general composition $\text{A}_2\text{B}_2\text{O}_5$ and is attractive as an oxygen anion conductor since it can support a large population of O^{2-} vacancies, as well as a variety of substituents in the A- and B-sites. To promote the partial oxidation reaction utilizing these mixed conducting membranes, they were successfully assembled in tubes.²¹⁷ One side of the reactor is exposed to air, and hence the membrane serves to separate oxygen from the atmosphere. This oxygen is then transported as oxide ions through the membrane where it goes on to react with the CH_4 present on the second side of the membrane, to yield syngas (Figure 11). Using these brownmillerite membranes at 1173 K, H_2/CO ratios between 1.9 and 2.0, a CO selectivity above 96% and a CH_4 conversion of about 90% can be obtained. It should also be emphasized that this performance was maintained by the membrane for continuous operation for over one year on-stream.

d. Oxydehydrogenation of Ethane. Production of ethylene monomer via oxidative dehydrogenation of ethane (ODE: $\text{C}_2\text{H}_6 + \frac{1}{2}\text{O}_2 \rightarrow \text{C}_2\text{H}_4 + \text{H}_2\text{O}$) is a reaction of great chemical and technological relevance. Besides the alkaline earth, rare earth, and

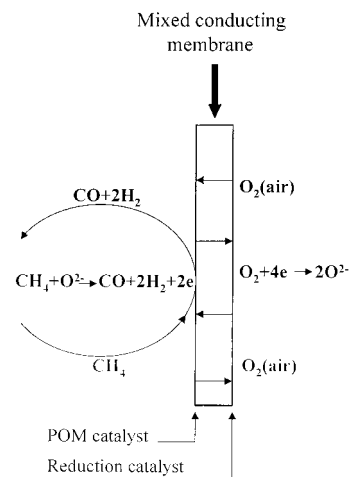


Figure 11. Schematic diagram of a perovskite membrane for the partial oxidation of methane to syngas.

transition metal oxides, with or without the use of alkali or halides as dopants, perovskite oxides are effective systems for the ODE reaction. Hayakawa et al.²¹⁸ studied the catalytic activity of $\text{CaTi}_{1-x}\text{Fe}_x\text{O}_{3-\delta}$ ($0 < x < 0.4$) and $\text{SrTi}_{1-x}\text{Fe}_x\text{O}_{3-\delta}$ ($0 < x < 1.0$) for the ODE reaction and found that the latter showed higher C_2H_4 selectivity than the former. Later, Yi et al.²¹⁹ reported a yield of 37% to C_2H_4 when working at 923 K and $\text{C}_2\text{H}_6:\text{O}_2 = 1:1$ (molar ratios) in the feed. A significant advance was achieved very recently by Dai et al.²²⁰ who embedded halide ions in the lattice of the perovskite oxide. Following this approach, the deep oxidation of C_2H_6 and C_2H_4 and the leaching of the halide from the lattice were minimized. The oxygen-deficient structures $\text{SrFeO}_{2.81}$ and $\text{SrFeO}_{2.618-\text{Cl}_{0.443}}$ were highly active for the ODE reaction, although the latter performed much better than the former, with a C_2H_4 yield of ca. 63% when working at 953 K, a reactant molar ratio of $\text{C}_2\text{H}_6:\text{O}_2:\text{N}_2 = 2:1:3.7$ and at atmospheric pressure. The temperature-programmed desorption of oxygen and temperature-programmed reduction experiments show that the introduction of chlorine into the $\text{SrFeO}_{3-\delta}$ lattice would lead to the regulation of oxygen vacancies and the $\text{Fe}^{4+}/\text{Fe}^{3+}$ ratio and hence suppression of C_2H_6 and C_2H_4 deep oxidation.

e. Other Oxidation Reactions. Perovskites have also been studied as model compounds in the oxidation of oxygenated compounds.^{190–193} Trikalitis and Pomonis¹⁹⁰ reported the activity profiles for the decomposition of isopropyl alcohol on $\text{La}_{1-x}\text{Sr}_x\text{VO}_{3-\delta}$ perovskites at temperatures between 473 and 573 K. Among the two reaction products, acetone and propylene, the selectivity of the reaction for $x = 0$ was ca. 15% for acetone and increased linearly with the substitution of La by Sr, reaching a value of 40% at $x = 1.0$. The apparent activation energy calculated for the total conversion of i-propyl alcohol according to first-order kinetics was close to 120 kJ mol^{-1} , which is similar to that found for acetone formation while that estimated for the propylene formation was lower by $10\text{--}15 \text{ kJ mol}^{-1}$ on average. The influence of electronic effects on the reaction appeared negligible, whereas the acid/base function of the catalyst played a key role. More recently, Sumathi et al.¹⁹³ have studied the selective oxidation and dehydrogenation

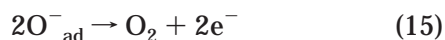
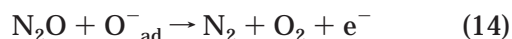
of benzyl alcohol on BaBB'O₃ (B = Pb, Ce, Ti; M' = Bi, Cu, Sb) perovskites in the absence and in the presence of oxygen. Partial reduction of the catalyst was observed on-stream when the reaction was carried in the absence of O₂ or at low O₂ partial pressures. Catalytic activity was found to depend on the reducibility of the catalyst surface, and this was higher for Cu-containing perovskites and lower for BaMO₃ (B = Ti, Ce) oxides. Catalytic activity and reducibility were correlated with metal–oxygen bonding as well as with the free energy of reduction of B-site cations

The chemical and thermal stabilities of perovskite-type oxides have also been exploited for the oxidation of halocompounds.^{221,222} Kiessling et al.²²¹ reported the complete decomposition of CH₃Cl, CH₂Cl₂ and 1,2-C₂H₄Cl₂ in air over LaMO₃ (M = Mn, Co) and La_{0.84}Sr_{0.16}Mn_{0.67}Co_{0.33}O₃ perovskite oxides at temperatures above 800 K. Besides the main reaction products (carbon dioxide, water, and hydrochloric acid) chlorine-containing byproducts (C–C coupling and cracking) were also formed in the low temperature range. Depending on the reaction temperature, the residence time and the type of reactant halocompound, a reversible catalyst deactivation takes place. Considering the formation of chloride species on the surface and in the bulk during reaction, it was suggested that the formation of more highly chlorinated byproducts takes place by insertion of chloride species on the catalyst surface in reactants or intermediates. The preferential formation of these byproducts with increasing time on-stream and with residence time, as well as the reaction temperature at lower conversion degrees, is consistent with a consecutive insertion of chloride on the surface in intermediates or adsorbed halocompounds.

B. Pollution Abatement

1. NO_x Decomposition

The decomposition of N₂O into its elements is one of the best model reactions to evaluate the catalytic activity of many materials in heterogeneous catalysis.²²³ The elementary steps involved in the N₂O decomposition reaction can be summarized as follows:



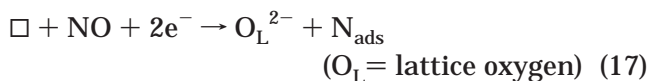
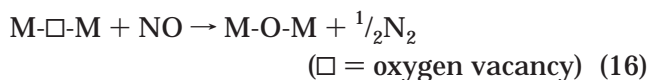
The decomposition rate is inhibited by oxygen, and its desorption has been found to be the rate-limiting step of the overall reaction^{224–226} (eq 15). Thus, the reaction rate would be expected to depend on the lattice parameter of the perovskite, because the M–O bond length and bond energy should alter the M–O_{ad}. This aspect and a brief account of the works con-

ducted on N₂O decomposition on perovskites up to the end of 80s were summarized in our previous review.¹⁰⁴

The catalytic decomposition of N₂O to nitrogen and oxygen was investigated by Gunasekaran et al.²²⁷ over various substituted La_{0.8}Sr_{0.2}MO_{3–δ} (M = Cr, Fe, Mn, Co, Y) perovskite series. Among the various solid solutions, La_{0.8}Sr_{0.2}CoO_{3–δ} showed a maximum N₂O conversion of 90% at 873 K. The activity of La_{0.8}Sr_{0.2}CoO_{3–δ} was found to be comparable to a reference Pd/Al₂O₃ catalyst at temperatures above 773 K when feeding N₂O (in helium). However, incorporation of O₂ to the feed stream (about 4% O₂) led to a decrease in the conversion of N₂O by ca. 13% in the case of La_{0.8}Sr_{0.2}CoO_{3–δ}, whereas it remained constant in the Pt/Al₂O₃ catalyst. Complementary studies on the reduction–oxidation properties as well as nonstoichiometry and oxygen desorption capacity over substituted La_{1–x}Sr_xMO_{3–δ} (M = Mn, Fe, Co) confirmed the operation of a redox mechanism for N₂O decomposition reaction.^{228,229} In addition, the effect of added oxygen in the reaction feed was to inhibit both N₂O conversion and the overall reaction rate, consistent with the established reaction mechanism in eqs 13–17 above.

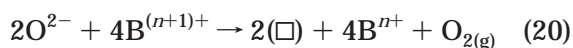
The decomposition of NO into N₂ and O₂ (2NO → N₂ + O₂) is thermodynamically favorable at temperatures below 1300 K. It is generally accepted that the decomposition of NO involves the dissociation of NO to nitrogen and oxygen on a catalytic surface and that nitrogen readily desorbs as N₂ while oxygen is strongly retained on the surface. Catalysts active for NO decomposition should accordingly display not only the ability to adsorb and dissociate NO but also the ability to facilitate the desorption of oxygen. A broad variety of catalytic systems such as metals, simple and mixed metal oxides, and ion-exchanged zeolites have been studied for this purpose.^{230–232} Several perovskite-type oxides exhibit good performance for the decomposition of NO at temperatures above 750 K^{104,233–235} and are quite stable for long-term operation at these high temperatures.²³⁶

Most of the results reported on the decomposition of NO on perovskite oxides can be described by a reaction scheme that includes the participation of molecular and dissociative chemisorption of NO:^{17,159,237}



Manganites, cobaltites, and ferrites^{57,234,236} as well as perovskite-related YBa₂Cu₃O_{7–x},²³³ La₂CuO₄ based-oxides,^{235,238} and BaRu_xBi_{1–x}O₃ (x = 0.33–1.0) perovskites²³⁹ have been reported to be active for NO decomposition. Teraoka et al.²⁴⁰ studied the effect of the partial pressure of NO and O₂ and contact time

(W/F) on the NO decomposition activity of $\text{La}_{0.8}\text{Sr}_{0.2}\text{CoO}_3$ and $\text{La}_{0.4}\text{Sr}_{0.6}\text{Mn}_{0.8}\text{Ni}_{0.2}\text{O}_3$ perovskites. The reaction was practically first-order with respect to NO and was inhibited by O_2 . To explain the kinetic results in a consistent fashion, a reaction mechanism was proposed in which the active site would be a pair of adjacent oxide ion vacancy sites near the surface. The reaction of NO molecules on the active site is assumed to occur stepwise (first-order kinetics). NO is adsorbed along with the oxygen atom that fits into the vacancy, and an electron flows to the NO molecule from a B-site cation neighboring the vacancy, giving rise to the formation of the NO^- species and the concomitant oxidation of the B-site cation ($\text{Co}^{3+} \rightarrow \text{Co}^{4+}$; $\text{Mn}^{3+} \rightarrow \text{Mn}^{4+}$; $\text{Ni}^{2+} \rightarrow \text{Ni}^{3+}$). As is well-known,²⁴¹ electron transfer to the antibonding orbital of NO reduces the bond order from 2.5 to 2 and facilitates the cleavage of the N–O bond. Once the second NO molecule has been adsorbed, a free N_2 molecule is released into the gas phase by the interaction of two neighboring NO^- species. The release of oxygen is regulated by the adsorption–desorption equilibrium, and the formation of two oxide vacancies (\square) involves a 4-electron process:



Because of the easy redox change of $\text{B}^{(n+1)+}/\text{B}^{n+}$ ($\text{B}=\text{Mn}, \text{Co}, \text{Ni}$) and the good electrical conductivity of the solids, electron transfer is expected to occur smoothly. Support for the redox mechanism operating in NO decomposition was provided by Bontchev et al.,²³⁹ who observed that the reaction is enhanced on $\text{BaRu}_x\text{Bi}_{1-x}\text{O}_3$ by the particular crystal structure of these oxides, with a high percentage of hexagonally stacked units of two and/or three RuO_6 octahedra. The concentration of these units increases with the Ru content, and they can be regarded as active sites for the NO decomposition reaction.

DV- $X\alpha$ cluster molecular orbital method²⁴² was applied to investigate the electronic effects of the LaBO_3 (B from Ti to Ni) series on the reactivity of the adsorbed NO molecule and the oxygen produced by direct NO decomposition at the oxygen vacancy. Yokoi and Uchida²⁴² calculated the bond orders of N–B and O–B pairs and found that they correlate with the maximum temperature of the O_2 DTP peaks. In addition, the ease O_2 desorption was ascribed to the higher binding energy component of the O1s core-level spectra located at 530.5–531.5 eV. Thus it can be assumed intuitively that the desorption site of such an O1s species is the active site for the direct decomposition reaction of NO on this perovskite oxide family.

2. Exhaust Treatment

Perovskite oxides are excellent candidates as catalysts particularly suited for exhaust gas depollution processes. They can be regarded as valuable alternative catalysts to supported noble metals, which are easy to synthesize at lower cost and with great thermal stability up to high temperatures. This section compiles the reduction processes of NO in the presence of different reducing agents.

Most work on the reduction of NO on perovskites has focused on the use of CO as a reducing gas because of the need to control NO and CO emissions especially from motor vehicles. Mechanistically, the $\text{CO} + \text{NO}$ reaction on perovskites seems to proceed through the formation of N_2O and surface isocyanate species.⁴⁶ If this possibility exists, then the perovskites must be tailored in such a way that the direct oxidation of CO becomes an easy process as compared with the isocyanate route. This may be possible with a proper choice of the cations in the perovskite oxides, with orbitals of suitable energy and symmetry able to activate the CO molecule directly so as to promote the oxidation reaction over the formation of isocyanate species.

Different perovskite systems were investigated as catalysts for the $\text{NO} + \text{CO}$ reaction in the 90s. Among these are $\text{La}_{1-x}\text{FeO}_3$,²⁴³ LaCoO_3 ,^{244,245} LaMnO_3 and $\text{LaMn}_{0.99}\text{Pt}_{0.01}\text{O}_3$,²⁴⁶ LaMO_3 and $\text{La}_{1-x}\text{Sr}_x\text{MO}_3$ ($\text{M} = \text{Fe}, \text{Co}, \text{Mn}, \text{Cr}, \text{Ni}$),^{247–249} $\text{La}_{1-x}\text{Sr}_x\text{Al}_{1-2y}\text{Cu}_y\text{Ru}_y\text{O}_3$,²⁵⁰ $\text{La}_{0.8}\text{Sr}_{0.2}\text{Co}_{1-2y}\text{Cu}_y\text{Ru}_y\text{O}_3$,²⁵¹ and $\text{La}_{2-x}\text{Sr}_x\text{NiO}_4$.^{252,253} On $\text{La}_{2-x}\text{Sr}_x\text{NiO}_4$, the transformation of NO is monomolecular as compared to CO oxidation, which is a bimolecular reaction. The apparent activation energies run parallel for both reactions, CO oxidation showing higher values, especially in the high temperature region. Kinetic analysis reveals that NO is more strongly adsorbed in samples poor in oxygen (large x) and more loosely on samples rich in that element (small x) in the low-temperature region, while at higher temperatures and at large x , the excess oxygen produced acts as a poison to the reaction.²⁵³ Details on the mechanism of the $\text{CO} + \text{NO}$ reaction on $\text{La}_{1-x}\text{Ce}_x\text{CoO}_3$ were provided by Forni et al.²⁵⁴ In this system, the first step involves the oxidation of CO by the catalyst surface, followed by the dissociative adsorption of NO onto the catalyst surface. Finally, the adsorbed nitrogen yields N_2O , N_2 , and NCO_{ad} along three parallel paths. Thus, oxygen exchange between NO and CO seems to occur indirectly and involves an oxygen vacancy. Additionally, the catalytic activity is decreased by the replacement of Ce^{4+} by La^{3+} in the perovskite structure, which reduces the mobility of bulk oxygen. A different mechanism is operative in the reducible La_2CuO_4 system:²⁵⁵ activity increases during the reaction up to a stabilized level while the solid is reduced with the formation of Cu^0 and La_2O_3 , suggesting that the reduced copper sites are active in the $\text{CO} + \text{NO}$ reaction. This reduction and the resulting activation are not determined by the stoichiometry of the reaction mixture conditions because they can also occur under oxidative reaction conditions when NO is present in large excess with respect to CO.

Effective reduction of NO was also accomplished by ethylene-²⁵⁶ and hydrogen-²⁵⁷ reducing agents. Harada et al.²⁵⁶ reported the performance for the selective reduction of NO with C_2H_4 over perovskites containing Co, Mn, Fe, Cr, Al, Sn, and Ti as host B cations in the ABO_3 structure. Only the systems with a nonredox function (Al, Sn, and Ti) displayed selective catalytic reduction of NO. Over perovskites containing redox cations, the undesirable consumption of C_2H_4 by O_2 proceeded preferentially. Ferri et

al.²⁵⁷ used $\text{La}_{0.9}\text{Ce}_{0.1}\text{MO}_3$ ($M = \text{Mn, Fe, Co, Ni}$) perovskites for NO reduction by H_2 and observed $M = \text{Co}$ as the most active. Activity was found to depend on both anion vacancies and Co^{2+} ions. The NO reduction with H_2 includes reduction of the catalyst followed by NO adsorption, which is favored by the lower oxidation state of the B-site cation. This involves the catalyst in a redox cycle exploiting its defect structure. The higher activity found for cobaltates could thus be attributed to the presence of O-vacancies suitable for NO adsorption. However, the oxidation state of the B-ion is also important. Indeed, the $\text{La}_{0.9}\text{Ce}_{0.1}\text{CoO}_{3+\delta}$ catalyst performed better after pretreatment in O_2 at high temperature. Under these conditions, oxygen is accommodated in the O-vacancies, which then desorb, favoring NO oxidation to surface NO_2 . In addition, the formation of Co^{2+} ions is needed in this catalyst to achieve a better adsorption and thus a faster N–O dissociation.

In the mid 70s, placing a catalyst in the exhaust of car engines opened a new area for the application of catalysts for controlling gaseous emissions from both mobile and stationary sources. This has received impetus due to the development of three-way catalysts (TWC) for converting HC, NO_x , and CO simultaneously.²⁵⁸ The systems used for this purpose are small particles of Pt, Pd, and Rh deposited on a ceria-alumina-coated ceramic substrate and display a number of desirable properties such as high activity, stability, and resistance to sulfur poisoning. However, shortage of the worldwide resources of noble-metals and high prices limit their use for such a purpose. In addition, the presence of water vapor and carbon dioxide in the exhaust stream along with the high-temperature reached sometimes due to local overheating make the perovskite oxides (ABO_3) excellent candidates as TWC catalysts. These systems often exhibit activity comparable to that of noble metal catalysts.^{104,259}

Incorporating noble metals (Pt, Pd, Rh) into the perovskite structure results in the stabilization of the metal against sintering, volatilization, or solid-state reaction with the substrate. Some enhancement in activity of the simple perovskite can also be achieved when small amounts of noble metals are incorporated. Sorenson et al.²⁶⁰ adopted this approach to use noble metal-loaded perovskites for the simultaneous reduction of NO and the oxidation of CO and unburned hydrocarbons. These authors found the substituted multicomponent cobaltite ($\text{La}_{0.6}\text{Sr}_{0.4}$)($\text{Co}_{0.94}\text{Pt}_{0.03}\text{Ru}_{0.03}$) O_3 highly active and selective for exhaust treatment from single cylinder engine. Selective reduction of NO_x (>90%) was attained in excess CO while efficient oxidation of hydrocarbons and CO was observed at the oxidizing side of the stoichiometric O_2 :fuel ratio. As can be seen in Figure 12, the above perovskite provides an operating window in which the elimination of all three pollutants was about 80% or higher.

It has been shown recently that the incorporation of a small amount of Rh into the $\text{LaMnO}_{3.15}$ perovskite ($\text{LaMn}_{0.976}\text{Rh}_{0.024}\text{O}_{3.15}$) leads to high three-way catalytic activity in a synthetic $\text{CO} + \text{NO} + \text{C}_3\text{H}_6$ mixture.²⁶¹ Rh is an essential component for the

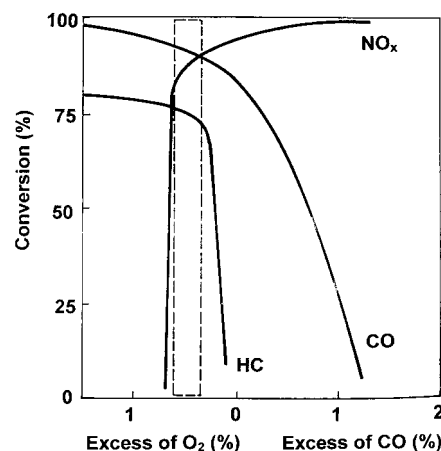


Figure 12. Conversions of NO_x , CO, and hydrocarbons on a multicomponent cobaltite ($\text{La}_{0.6}\text{Sr}_{0.4}$)($\text{Co}_{0.94}\text{Pt}_{0.03}\text{Ru}_{0.03}$) O_3 . The dashed lines indicate clearly the strong influence of excess oxygen on the pollutants removal.

reduction of NO, while Mn^{3+} ions allow the total oxidation of CO and C_3H_6 . In this work, the stoichiometric factor (s) = $(2\text{O}_2 + \text{NO})/(\text{CO} + 9\text{C}_3\text{H}_6)$ was varied from very reducing ($s = 0.46$) to very oxidizing ($s = 2.18$) conditions with large amplitude oscillations of the feed stream. These oscillations have only a slight influence on the catalyst performance, and the light-off temperatures for catalyst $\text{La}(\text{MnRh})\text{O}_{3.15}$ were quite similar under stationary and cycling conditions. The lack of effect of the oscillating conditions suggests that the over-stoichiometric oxygen is easily removed and replenished from the oxide lattice and is used under oscillating conditions to compensate for the variations in the composition of the reactant mixture: at 673 K this oxygen is consumed under a stream of CO to form CO_2 , whereas the $\text{La}(\text{MnRh})\text{O}_{3.15}$ is transformed into $\text{La}(\text{MnRh})\text{O}_3$. The over-stoichiometric oxygen can be easily recovered under oxygen or NO under the conditions of three-way reactions. This corresponds to the oxygen storage capacity of the catalyst, which allows stable high performance in rich/lean oscillating compositions. Additional experiments in the presence of 10% steam in the feed stream revealed some catalyst deactivation; in particular, NO reduction was strongly inhibited.²⁶¹ This deactivation was explained in terms of (i) strong adsorption of water on the $\text{La}(\text{MnRh})\text{O}_3$ surface which poisons active sites and (ii) participation of water gas-shift (WGS) and reforming reactions. The type ii possibility seems very likely because the H_2 produced by the WGS reaction does not dissociate on the mixed oxide and hence cannot favor NO reduction. This is not the case of noble metal TWCs, which are highly active for such reactions, while at the same time maintaining the ability to dissociatively adsorb hydrogen and reduce NO.

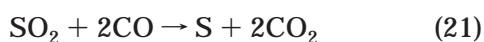
Alkaline and alkaline earth perovskites are also highly active for the combustion of soot particulates in diesel engine exhaust.^{262,263} The ignition temperature with perovskite oxides decreases by more than 200 K as compared to carbon particulates alone. In the ABO_3 perovskites, partial substitution of alkali and alkaline-earth metals at the A-site enhances the catalytic activity in the combustion of soot particulates. The removal of soot is also favored by the

presence of NO_x in the feed stream, and the reaction presumably takes place at the interface point where soot-oxide and NO gas meet.

3. Stability

The stability of a few unsubstituted (LaMnO₃, LaCoO₃) and Pb-substituted (La_{1-x}Pb_xMnO₃) perovskites was studied by Yao.²⁶⁴ It was observed that the introduction of steam caused a drop in catalyst activity, the resulting specific activity being comparable to that of the single oxide (Co₃O₄) at low temperature. Conversely, adding a 0.1% SO₂ into the feed stream resulted in an enhancement in activity of the Pt-substituted perovskites (only containing 300 ppm Pt). This effect is, however, opposite to the general tendency to decrease activity instead of increasing activity in the presence of SO₂. Quantitative studies of the chemisorption of SO₂ on several La-containing perovskites revealed that the amount of chemisorbed SO₂ required to suppress the reaction rate by a 90% is approximately that of one monolayer. SO₂ chemisorption is believed to occur on cation sites via the formation sulfite–sulfate structures. Looking at the interaction modes of SO₂ on perovskites surfaces, Tejuca et al.¹⁰⁴ suggested that the poisoning effect of SO₂ on ABO₃ perovskites is primarily associated with its adsorption on the catalytically active B cations (ionic radius of B³⁺ is smaller than that of A³⁺). The interaction of SO₂ at the B-site cannot be ruled out, although such a process does not lead to catalyst deactivation.

Chemisorbed SO₂ on the perovskite surface can be readily reduced by the CO present in the feed stream.^{265,266} The reaction produces elemental sulfur (eq 21), although further reaction between S and excess CO is expected to occur (eq 22):



It was reported that COS formation can be strongly inhibited using the perovskite LaTiO₃, even at high SO₂ conversions. This behavior appears to be related to the high resistance of LaTiO₃ to form sulfides, with the elemental sulfur produced by reaction 21. This explanation is based on the fact that the stability of the oxide versus sulfide, as measured by the difference between the heats of formation of simple oxides and sulfides for different transition metals, was found to reach a maximum for Ti.²³⁷ A few examples showing the performance and the stability of several perovskites in the reduction of SO₂ with CO were summarized in our previous work.⁴

More recently, it was demonstrated that incorporation of Pt to a substituted (LaCe)(FeCo)O₃ perovskite leads to high activity and durability.²⁶⁷ Surface analysis of the original sample revealed that palladium is present as a mixture of Pd⁴⁺ and Pd²⁺; however, the catalyst subjected to accelerated aging tests showed a single component characterized by a binding energy of Pd3d core electrons of Pd³⁺ species. This unusual, high valence state of Pd in the perovskite structure seems to be responsible for the diffusion of oxygen ions within the crystal. As a

result, adsorption–desorption of activated oxygen is favored, thereby affording enhanced catalyst performance. The mechanism responsible for the improvement of catalytic activity of the Pd-loaded (LaCe)-(FeCo)O₃ perovskite is primarily associated with the specific incorporation of Pd as a solid-solution into the structure that controls the growth of Pd particles under the redox atmosphere at high temperature.

C. Hydrogenation and Hydrogenolysis Reactions

1. Hydrogenation of Carbon Oxides

Transition metals and metal oxide-promoted metals have been used for the synthesis of hydrocarbon^{268–272} and oxygenated compounds^{57,273–278} from syngas (CO + H₂) mixtures. Regarding these reactions, Δ*G*° values at 298 K are in most cases negative and a large variety of products (paraffins, olefins, alcohols, ethers, esters) can be achieved under appropriate reaction conditions. From the analysis of the existing vast body of work, it can be concluded that there is a close relationship between the nature and chemical state of the elements responsible for the activity and the type of surface C-containing intermediates and product distributions.^{279–281} Accordingly, ABO₃ perovskite-type oxides with reducible B³⁺ ions under typical reaction conditions are excellent model catalysts to gain useful insight into the surface process taking place during CO (and CO₂) activation and carbon chain growth.

a. CO Hydrogenation. Somorjai et al.^{282,283} studied the influence of reduction pretreatments on the activity of LaRhO₃ at different temperatures in syngas conversion. The reaction products were CH₃OH and hydrocarbons (HC) and the relative proportion CH₃OH/HC was found to be highly temperature-dependent. These results were rationalized by assuming that two different reaction mechanisms are involved: CH₃OH is formed through a nondissociative adsorption of CO, whereas hydrocarbon formation follows a dissociative mechanism. The change of the CH₃OH/HC ratio with temperature is due to competing H- and CO-insertion reactions and variable proportions of molecularly and dissociatively adsorbed CO and H₂ on the surface. As the methanol is the major reaction product at temperatures below 500 K, hydrogenation of adsorbed CO species predominates. However, at temperatures above 620 K the C–O bond splits and CH₃OH formation is strongly inhibited, while methane and other C₂ + hydrocarbons are the major reaction products. In the middle temperature range, C–O is broken, yielding CH_x fragments that can then recombine to form either CH₄ or other HC through hydrogenation reactions or undergo CO insertion to yield oxygenates. Surface analysis of the activated catalysts allowed these authors to conclude that the active catalyst contains Rh⁺ species and a small proportion of Rh⁰.

Gysling et al.²⁸⁴ and Monnier and Apai²⁸⁵ investigated the hydrogenation of CO on H₂-reduced LaRhO₃ perovskite at reaction temperatures from 493 to 623 K. These authors observed that the formation rates of HC decreased monotonically with the number of C atoms, suggesting the participation of a common

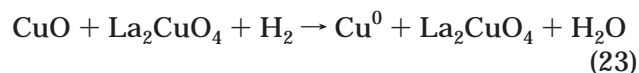
mechanism for carbon chain growth. However, at temperatures above 548 K the formation rates of $C_2 + OH$ were found to be greater than for CH_3OH , indicating that the mechanism is different in both cases. The $C_2 + OH$ oxygenates are probably formed by CO insertion into adsorbed alkyl fragments, as previously reported by Ichikawa and Fukushima²⁸⁶ and Watson and Somorjai.²⁸² The quite similar product distributions observed during the hydrogenation of CO on $LaRhO_3$ and a conventional Rh/SiO_2 catalyst at the same reaction temperatures suggests that the same catalytic Rh species is present in both catalysts. Since the Rh present on Rh/SiO_2 catalysts is considered to be Rh^0 under such reaction conditions,^{284,285} it may be inferred that the active rhodium present in $LaRhO_3$ should also be Rh^0 .

Noble metal perovskites of the type $BaBO_3$ ($B = Rh, Ru, Ir, Pt$) have also been used in syngas conversion.²⁷³ $BaRhO_3$ and $BaPtO_3$ were found to yield selectively oxygenates, almost exclusively methanol (maximum selectivities of 62 and 54%, respectively). By contrast, the $BaRuO_3$ perovskite showed the lowest oxygenate selectivity. All these perovskites were pure crystalline phases prior to catalyst testing. The bulk oxidation state of the noble metal was the expected M^{4+} , although partially reduced species instead of, or in addition to, the M^{4+} state were observed. Both crystalline and amorphous $BaBO_3$ perovskites are unstable against syngas and its reaction products; the B^{4+} ion is reduced to M^0 , and the barium is converted to $BaCO_3$.

Copper-substituted perovskites were also used in syngas conversion by Broussard and Wade²⁷³ and Brown-Bourzutshky et al.²⁷⁵ These authors observed that substitution of Mn by Cu in $LaMnO_3$ samples shifted the product distribution from hydrocarbons to methanol and small amounts of C_{2+} oxygenates. Later on, van Grieken et al.²⁷⁸ used $LaTi_{1-x}Cu_xO_3$ perovskites to analyze the effect of the substitution degree (x) on the activity and product distributions during CO hydrogenation. The conversion of CO strongly depends on the Cu substitution, the highest values being attained in the $0.5 \leq x \leq 1.0$ composition range and the lowest for $x = 0$. $LaTiO_3$ produced methanol, CH_4 , and CO_2 , with selectivities about 30%, and a substantially lower proportion of dimethyl-ether. Upon incorporation of Cu, the selectivity of the alcohols increased whereas that of methanation decreased. It was also emphasized that a reference Cu/La_2O_3 catalyst gave lower methanol selectivity and substantially higher selectivities to CO_2 , CH_4 , C_2H_6 , and dimethyl-ether. The methanol synthesis rate was found to pass through a maximum at substitution $x = 0.6$. This rate of $9.7 \times 10^{-2} \text{ g h}^{-1} \text{ m}^{-2}$ is similar to the one observed by Sheffer and King²⁷⁴ for a 1.2% K-promoted unsupported Cu catalyst working under similar reaction conditions. All these findings clearly indicate the importance of copper for both activity and selectivity toward methanol.

Surface analysis of used catalysts revealed that copper becomes reduced, and that for $x = 1.0$, and to a lesser extent for $x = 0.6$, the reduced Cu-phase coexists with a minor proportion of Cu^{2+} ions. This

is consistent with the presence of both CuO and La_2CuO_4 phases in the calcined sample; only CuO is reduced in H_2 at 573 K while La_2CuO_4 remains unreduced up to 673 K:



The Auger parameter of copper in a representative $LaMn_{0.5}Cu_{0.5}O_3$ catalyst prereduced and used in CO hydrogenation at 573 K appeared 1849.2 eV,²⁷⁸ which agrees with that at 1848.8 eV observed by Sheffer and King²⁷⁴ for a K-promoted copper catalyst exposed to a $CO:H_2$ mixture, and by Karwaci et al.²⁸⁷ for Cu_2O (Cu^+). This result indicates that Cu^+ species are present in the used catalyst and are presumably involved in the CH_3OH synthesis reaction. As copper is stabilized in the La_2CuO_4 phase, Cu^+ ions can be developed on its surface under on-stream operation. The fact that Cu^+ ions remain dispersed and embedded in the La_2CuO_4 matrix also explains the high resistance to sintering of the resulting reduced phase, thus explaining the great stability of these catalysts for long periods. The differences in catalytic behavior of $LaTi_{1-x}Cu_xO_3$ and the reference Cu/La_2O_3 sample were explained in terms of the structural differences. Because large Cu^0 crystallite particles have been found in the Cu/La_2O_3 catalyst it seems that the formation of hydrocarbons very probably occurs on metallic Cu. Because CO does not dissociate on Cu^0 ,²⁸⁸ adsorbed CO can be hydrogenated to form H_x -CO intermediates, which then dissociates into CH_x fragments, the starting precursor of the hydrocarbons. Finally, the presence of a small proportion of Cu^+ on the surface of the Cu crystals, or in close contact with them, cannot be excluded, since this species appears to be involved in the synthesis of methanol.

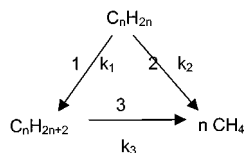
b. CO_2 Hydrogenation. Hydrogenation of CO_2 on metal catalysts produces mainly CH_4 , with minor amounts of higher hydrocarbons. Although this is a strong H_2 -consuming reaction, a few works were focused on the use of perovskite systems for the target reaction. Ulla al.²⁸⁹ studied the catalytic behavior for CO_2 hydrogenation of $La_{1-x}M_xCoO_3$ ($M = Sr, Th$) perovskites prereduced at different extents. For unsubstituted $LaCoO_3$, the initial reaction rate of the reduced perovskite depended on the extent of reduction but did not reach a maximum. The production of C_{2+} products decreased at higher degrees of reduction, whereas CH_4 selectivity followed the opposite trend. However, the $La_{0.8}Th_{0.2}CoO_3$ sample was much more active and selective to CH_4 than its unsubstituted $LaCoO_3$ counterpart, and the extent of reduction does not significantly affected the initial rate. The behavior of $La_{0.6}Sr_{0.4}CoO_3$ was found to depend on the reaction temperature. Below 570 K, the product distribution of the unreduced and the H_2 -treated catalysts was close to that of the Th-substituted sample. However, at higher reduction degrees CH_4 selectivity decreased and the amount of C_{2+} products increased with the extent of reduction. In particular, the fully reduced catalyst gave the highest selectivity to C_{2+} products.

It has been observed that the surface Co/La ratio in the reduced catalysts correlates with the rate of methanation and C_{2+} production. This shows that Co^0 is the active species on which CO_2 first chemisorbs dissociatively and then the adsorbed CO fragment undergoes further hydrogenation, in accordance with the mechanisms describing hydrogenation of CO adsorbed on Group VIII metal surfaces.²⁷⁰ The rate of CH_4 formation over the H_2 -reduced $La_{1-x}M_xCoO_3$ samples reported by Ulla et al.²⁸⁹ was substantially higher than that reported by Weatherbee and Bartholomew²⁹⁰ for a silica-supported Co catalyst under similar reaction conditions, indicating that the specific activity of the metallic sites is affected by the surrounding matrix. This led to the conclusion that the Co^0 crystallites developed on the surface on both Th- and Sr-substituted perovskites have a higher specific methanation activity than Co on silica. The matrix effect may arise from the stabilization of highly dispersed cobalt particles on the perovskite surface, which in turn would be affected by the basic character of the perovskite components.

2. Hydrogenation and Hydrogenolysis Reactions

Since Pedersen and Libby¹⁷¹ first reported that $ACoO_3$ (A = lanthanide elements) oxides are more active than some transition metals for the hydrogenolysis of *cis*-2-butene, many other hydrogenation reactions have been carried out on perovskite oxides. Among these, the use of cobaltites for hydrogenolysis of various alkanes^{291–293} and ethylene^{102,294,295} remain prominent.

The hydrogenation and hydrogenolysis of C_2 – C_5 hydrocarbons proceed according to the following reaction scheme (except for the butene isomers):²⁹¹



Reactions 1, 2, and 3 represent the hydrogenation of alkenes, the direct hydrogenolysis of alkenes, and hydrogenolysis of alkanes, respectively. The reaction of C_2H_4 with H_2 on $LaCoO_3$ below 420 K yields only the hydrogenated product C_2H_6 , whereas above this reaction temperature the hydrogenolysis of C_2H_4 forms CH_4 in addition to the hydrogenation. The hydrogenolysis of C_3 – C_5 alkanes such as propane, butane, isobutane, pentane, isopentane, and neopentane on $LaCoO_3$ produces only CH_4 .^{291,292} Neither the corresponding alkenes nor the fragmented hydrocarbons are formed in the gas phase. The reaction order with respect to the hydrocarbon pressure is unity for all reactions, while the hydrogen order increases with the number of carbon atoms involved in the reactant hydrocarbons. Thus, reaction orders of 0.0, 1.0, and 2.0 were found for C_3H_8 , C_4H_{10} , and C_5H_{12} , respectively. By contrast, in the reaction of alkenes with H_2 , methane, and the corresponding alkanes were produced. For example, the reaction of propene with hydrogen produces a considerable amount of methane, together with propane during the initial reaction

stage. The reaction of butenes with hydrogen undergoes rapid isomerization, followed by the formation of butane and then methane. For all reactions, the ratios of the butene isomers produced remain almost unchanged until the disappearance of the reactant butenes; the *cis*-2-butene/*trans*-2-butene, *cis*-2-butene/1-butene, and *trans*-2-butene/1-butene ratios are 1.0, 1.8, and 1.8, respectively. Since there is no marked difference in the observed rates of butene hydrogenation, the average of these rates represents that of butene hydrogenation.

The hydrogenolysis of alkanes has mainly been studied for transition metal catalysts.²⁹⁵ The kinetic behavior is characterized by negative orders with respect to H_2 pressure and by a wide variety of fragmented hydrocarbons, except for the selective formation of C_2H_6 in the case of nickel catalysts.²⁹⁶ The proposed mechanism involves the dissociative adsorption of alkanes, releasing an H-atom on the surface, followed by step-by-step cleavage of C–C bonds. It is emphasized that the hydrogenolysis reactions of alkanes on $LaCoO_3$ are characterized not only by the high reaction order with respect to the H_2 pressure but also by the selective formation of CH_4 ; neither the other fragmented nor hydrogenated hydrocarbons are detected in the gas phase. Tracer isotopic studies in the reaction of alkanes with deuterium showed that large amounts of methane (CHD_3 and CD_4) are involved, even from the initial stage of hydrogenolysis, whereas the fractions of the D_2 -exchanged alkanes are negligibly small. These results indicate that the adsorption of alkanes is irreversible, although the surface species thus produced undergo a rapid hydrogen exchange.

Ichimura et al.²⁹³ compared the behavior of $LaCoO_3$, $LaFeO_3$, and $LaAlO_3$ in the hydrogenolysis of alkanes and observed that only $LaCoO_3$ perovskite is active in these reactions. The reaction exhibits a maximum rate at a given temperature, which depends on the nature of each catalyst: ca. 420 K for $LaCoO_3$ and $LaFeO_3$, and 490 K for $LaAlO_3$. The distributions of D-atoms in the reactants and products, when D_2 is used instead of H_2 , indicate highly D-exchanged ethanes at 333 and 573 K. However, the deuterium distributions among gaseous hydrogen isotopes reaches equilibrium at high temperatures, although much smaller amounts of HD and H_2 are produced at lower temperatures. These isotope distributions indicate that the hydrogenation proceeds via an ethyl radical as intermediate and the rate-determining step varies from the adsorption of hydrogen at 333 K to the hydrogenation of the ethyl radical at 573 K.

In the TPD spectra of hydrocarbons from $LaCoO_3$ exposed to ethane at 300 K, single peaks of C_2H_2 and C_2H_4 appear at ca. 380 K and two peaks of C_2H_6 at ca. 380 and 540 K, with methane only above 450 K. Almost the same TPD spectra are obtained from the surface exposed to C_2H_4 , although the fraction of methane formed is smaller. The TPD spectra of hydrogen from $LaCoO_3$ shows two peaks, referred to as the α -peak, appearing below 340 K, and the β -peak, above this temperature. When the surface retaining β -H was exposed to C_2H_6 at 298 K, the TPD

spectra revealed the complete disappearance of the C_2H_2 and C_2H_4 peaks and a considerable enhancement of the C_2H_6 and CH_4 peaks, with no shift in their positions. Consumption of the β -H located at the lower temperature side of β occurred as a consequence of contact with C_2H_6 , thus suggesting that these H-species would be responsible for the hydrogenolysis and also for the hydrogenation of C_2H_4 and C_2H_2 . Hydrogen was desorbed from the $LaFeO_3$ and $LaAlO_3$ surfaces, and its TPD spectra consisted of α - and β -peaks similar to those observed for $LaCoO_3$. However, the desorption spectra of C_2H_4 and C_2H_6 are relatively simple; only the original molecules are observed. The H-preadsorbed $LaFeO_3$ and $LaAlO_3$ surfaces convert the subsequently adsorbed C_2H_4 only to C_2H_6 . On these surfaces, β -H is also largely consumed. As revealed by photoelectron spectroscopy, reduction of Co^{3+} to Co^{2+} occurs during the reaction, resulting in a structural change and a drop of catalytic activity. By contrast, no significant change in La 3d spectra is observed for any of the catalysts in comparison with that seen for La_2O_3 .

TPD and XPS data point to the participation of Co^{3+} ions for the C–C bond cleavage during the hydrogenolysis of alkanes.²⁹³ H_2 , CO, and C_2H_4 adsorption at room temperature provide a surface site density of $4 \times 10^{14} \text{ cm}^{-2}$ on $LaCoO_3$, which corresponds to about 40% of the total surface ions. These results suggest that most of the exposed surface is available for the reaction and the (110) and (102) lattice planes are likely to be exposed at the surface because of their higher thermodynamic stability than the other planes. For hydrogenolysis, the geometric arrangement of the (110) plane substantiates the co-functional role in which the C–C bond is broken on the Co^{3+} , whereas the nearby O^{2-} provides H-adatoms to the resulting monocarbon species. These synergic effects by the lattice ions are even more pronounced in the hydrogenolysis of longer alkanes. The distance between the adjacent Co^{3+} in the (110) plane is 0.542 nm. The C-atom chain of butane or higher alkanes is long and flexible enough to interact with two Co^{3+} in a bridge form. Although La^{3+} and O^{2-} fail to adsorb alkanes dissociatively, both ions are likely to accommodate the methyl and carbene groups formed as a result of the bond rupture. Thus, such a bridged adsorption makes the nearby La^{3+} and O^{2-} effective in supplying H-atoms to the decomposed species, thus lowering the activation energy.

Crespin and Hall¹⁰² investigated the surface states of several ABO_3 perovskites and found that Co^{3+} ions in $LaCoO_3$ are easily reduced to Co^{2+} , but they reduce to the metal (Co^0) and La_2O_3 only at temperatures as high as 773 K.¹⁰² They also observed that the final products of the reduction ($Co^0 + La_2O_3$) restore its original perovskite structure by reoxidation at 673 K. Using $LaCoO_3$ prepared in the same way, Petunchi et al.²⁹⁴ reported changes in catalytic activity for C_2H_4 hydrogenation, with an increase in the degree of reduction of the oxide; maximum activity at 253 K is observed on the $LaCoO_{3-x}$ catalyst at the $x = 0.7$ composition for the first oxidation–reduction cycle and at $x = 1.2$ for the second cycle. The catalyst

prepared by Petunchi et al.²⁹⁴ is more reducible than that prepared by Crespin and Hall,¹⁰² since the catalyst of the former authors is reduced to some extent at 353 K. Ulla et al.²⁹⁵ proposed that the active site of $LaCoO_3$ would be highly dispersed Co^0 particles on the La_2O_3 surface.

A CNDO-MO calculation was performed for ethane adsorbed on a linear atomic cluster, $O-M-O-M-O$ ($M = Co, Fe, Al$), which represents one part of the (110) plane of perovskite.²⁹¹ The adsorption energy of ethane and the change in C–C bond energy were estimated by changing the distance between the axes of ethane and the cluster lying in parallel. In the case of $[Co-O]$ and $[Fe-O]$ clusters, the energetically stable adsorption takes place when the center of the molecule is located on the metal ion, whereas for the $[Al-O]$ cluster the favorable position of the admolecules shifts to the top of the central oxygen atom. The percentage decreases in the C–C bond energy induced by adsorption at equilibrium distances are estimated at 3.7, 1.7, and 6.4% for the $[Al-O]$, $[Fe-O]$, and $[Co-O]$ clusters, respectively; the largest value for the $[Co-O]$ cluster reflects the strong ability of $LaCoO_3$ to break the C–C bond as compared to the other two perovskites.

D. Photocatalysis

Perovskite oxides, in particular $SrTiO_3$, have commonly been used as photocatalysts because some of them can decompose H_2O into H_2 and O_2 with no external bias potential.²⁹⁷ This is because the conduction band (CB) edges of some of the perovskite oxides are more negative than the H^+/H_2 energy level. Since the photocatalytic activity is related to the surface properties of these perovskites, powdered materials rather than single crystals or films were used for this purpose.²⁹⁸

1. Photodecomposition of Water

Wrighton et al.²⁹⁷ reported the photoassisted splitting of water molecule into H_2 and O_2 using a photoelectrochemical cell having a $SrTiO_3$ single-crystal photoanode at zero applied potential. Hydrogen evolution was also observed in experiments conducted upon irradiation a $SrTiO_3$ crystal coated with alkali and in contact with water vapor.²⁹⁸ In addition, there are several works addressing the photocatalytic decomposition of water over irradiated $SrTiO_3$ powders in suspension.^{299–301} Lehn et al.³⁰¹ found that $SrTiO_3$ powders alone were unable to split the water molecule into its components and that a metal coating of the substrate was an essential ingredient to make H_2 evolution observable.

Concerning different doping metals, $Rh/SrTiO_3$ system exhibited higher activity than $SrTiO_3$ powders coated with other transition metals. In general, the aim of metal coating is to decrease the H_2 over-voltage of the semiconductor, which, since it is usually very high, leads to low efficiency in the photoreduction of water. The over-voltage can be decreased by metal deposition. A metal-deposited semiconductor acts as a “short-circuited” photoelectrochemical cell, where oxidation and reduction reactions occur at two different sites, i.e., on the semi-

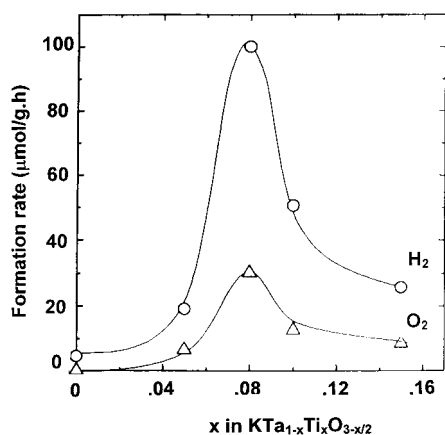


Figure 13. Formation rate of H_2 and O_2 as a function of Ti content in KTaO_3 (loaded with 1 wt % NiO). Reprinted from ref 307 by permission of the publisher. Copyright 1999 by The Chemical Society of Japan.

conductor and on the metal islands, respectively, of the same particle. Metal deposition also decreases the recombination of photoproducted electrons and holes by enhancing the rate of electron transfer to the metal. Surface modifications of the SrTiO_3 substrate with an oxide such as NiO have also been attempted.³⁰² Thus, working with the NiO/SrTiO_3 photocatalyst H_2 evolution was ascribed to formation of some NiO/Ni domains, whereas O_2 evolution came from sites located at the SrTiO_3 phase. It has been suggested that the role of the nickel phase at the interface is to enhance the transfer of electrons between NiO and SrTiO_3 oxides.³⁰³

In all these investigations, commercially available SrTiO_3 powders were used, which have a particle size of $\geq 2 \mu\text{m}$. Since there is a clear particle size-dependence of the band structure, and consequently the electronic properties of the semiconductor crystallites,³⁰⁴ it became imperative to prepare ultrafine particles of SrTiO_3 . Ultrafine powders of binary oxides are not easy to obtain because of the high temperature required for the reaction between the refractory components. Thampi et al.³⁰⁵ studied the photocatalytic activity of SrTiO_3 powders prepared by the sol-gel technique. Kudo et al.³⁰⁶ found that photocatalytic activity was strongly dependent upon the calcination temperature of SrTiO_3 and the optimum calcination temperature is different for different reactions.

Mitsui et al.³⁰⁷ found that the activity of KTaO_3 for the photocatalytic splitting of water was greatly improved by partially substituting Ta with a tetravalent cation M^{4+} (Ti^{4+} , Zr^{4+} , Hf^{4+}). The formation rate of both H_2 and O_2 as a function of the amount of Ti^{4+} substituting the Ta site of KTaO_3 reached the maximum value for a substitution degree of $x = 0.08$. The formation rate of H_2 at that optimized composition ($\text{KTa}_{0.92}\text{Ti}_{0.08}\text{O}_{2.96}$) attained a value of $100 \mu\text{mol h}^{-1} \text{g}^{-1}$, which in turn proved to be higher than that of Zr^{4+} - or Hf^{4+} -substituted counterparts, while the formation rate of O_2 was slightly lower than half the H_2 formation rate (Figure 13). The electronic spectra of all M^{4+} -substituted samples revealed no change in the band gap (ca. 3.8 eV); however, their electric conductivity decreased by substituting Ta^{5+} with M^{4+} .

Therefore, it seems likely that the M^{4+} element acts as a charge carrier annihilator, and it is expected that the life of photoexcited electron and hole will be improved by decreasing charge density. Thus, the formation rate of H_2 was enhanced by partially substituting Ta^{5+} with M^{4+} ions. On the other hand, carrier density would become insufficient owing to the incorporation of M^{4+} ion annihilator, with the subsequent drop in photocatalytic activity.

Very recently, Kudo and Kato³⁰⁸ reported enhanced activities of water splitting over NiO/NaTaO_3 photocatalysts doped with low amounts of lanthanide oxides. Lanthanum oxide was the most effective dopant with apparent quantum yields approaching 50%. Scanning electron microscopy observations suggested that the effects on the catalytic properties are mainly due to the decrease in the particle size and the characteristic step structure created by the doping. As the particle size is decreased, the probability of the surface reaction of electrons and holes with water molecules is increased in comparison with recombination in the bulk, resulting in an increase in the photocatalytic activity for water splitting. The photocatalytic activity was decreased when Eu and Yb were doped into NiO/NaTaO_3 . This effect may be explained considering that the tantalate photocatalysts has high conduction band levels.³⁰⁹ The Eu^{3+} and Yb^{3+} can trap the photogenerated electron in the high conduction band levels of NaTaO_3 because they can take a divalent oxidation number. Such electron capture suppresses the supply of electrons to NiO cocatalyst, resulting in a decrease in the photocatalytic activity.

Ion-exchangeable layered perovskites of the type $\text{K}_2\text{La}_2\text{Ti}_3\text{O}_{10}$ are also attractive water-splitting photocatalysts.³¹⁰ The structure basically consists of two-dimensional oxide sheets stacked along the c axis, in which K^+ ions are located between the individual sheets as interlayer cations to compensate for the negative charge of the layer. The performance for water splitting under UV irradiation of $\text{K}_2\text{La}_2\text{Ti}_3\text{O}_{10}$ photocatalysts and their 3% Ni-loaded counterparts was reported by Takata et al.³¹⁰ The generation of H_2 and O_2 is observed in both cases, and this increases almost linearly with the reaction time. For Ni-modified photocatalysts, activity becomes remarkably enhanced, and the H_2/O_2 ratios approach the stoichiometric value. A key feature of these layered perovskites is their inability to absorb light in the visible region because the oxides containing metal cations with a d^0 electron configuration are wide gap semiconductors. The incorporation of Pb into these layered perovskites seems to be effective in extending the absorption edge into the visible region.³¹⁰ The edge of the valence band shifts to the negative side due to Pb incorporation probably because of the donation of Pb6s electrons to the valence band, to which O2p electrons contribute.³¹¹ This is illustrated by the Pb-exchanged $\text{RbPb}_2\text{Nb}_3\text{O}_{10}$ photocatalyst, which generates H_2 from $\text{H}_2\text{O}/\text{CH}_3\text{OH}$ mixtures even under irradiation of light with a wavelength longer than 400 nm.

Other highly donor-doped (110) layered perovskites loaded with NiO have proved to be efficient photo-

catalysts for the water splitting under UV irradiation.^{312,313} These layered structures, with a generic composition $A_mB_mO_{3m+2}$ ($m = 4, 5$; $A = \text{Ca, Sr}$; $B = \text{Nb, Ti}$), exhibited high quantum yields and stoichiometric evolution of H_2 and O_2 . The high photocatalytic activity resulted from the specific layered structure and the high concentration of donor levels as compared with the bulk perovskite. When NiO was incorporated into these perovskites, a significant enhancement in photocatalytic activity was observed. This improvement, which might be ascribed to the role of Ni in p–n junction between nickel and the layered perovskite, was made possible by reduction of the Ni-loaded layered perovskite at 973 K and further oxidation at 473 K. The rates of H_2 and O_2 production increased with the amount of Ni incorporated up to 1 wt %. The nickel oxide, a p-type semiconductor, and the perovskite oxide, an n-type semiconductor, should absorb the sufficient photons for its band gap excitation so that the p–n junction can operate properly. The high electron density of these donor-rich materials would create a narrower charge depletion region of the semiconductor and an increased band bending, which would allow more efficient electron–hole separation and higher quantum yields than the undoped counterparts.

2. Other Photocatalytic Reactions

Several titanates and cobaltites have been used for the photocatalytic oxidation of CO.^{314,315} A strong photocatalytic effect was observed over BaTiO_3 and SrTiO_3 samples, whereas no effect was detected over the easily reducible oxide LaCoO_3 . Activity was found to depend on the preparative source of the photocatalyst.

Photocatalytic synthesis of NH_3 from N_2 and H_2O was performed over SrTiO_3 and binary-wafered catalysts of SrTiO_3 and platinum black,³¹⁶ where the copolymer of ethylene and vinyl alcohol was studied as a binder. The yield of NH_3 was larger in the case of the binary-wafered catalyst than the semiconductor powdered catalyst alone. The photosynthesis of NH_3 and its subsequent photodecomposition were investigated over Ba and Sr-titanates.³¹⁷ The rate of NH_3 production from H_2O and N_2 mixtures was found to be very small on the undoped BaTiO_3 and SrTiO_3 perovskites. The decomposition of water was strongly enhanced upon NiO doping of the SrTiO_3 substrate although the yield of NH_3 remained very small. On the other hand, the amount of NH_3 formation increased significantly for the doubly doped RuO_2 – NiO – BaTiO_3 and RuO_2 – NiO – SrTiO_3 samples. This enhancement can be attributed to the increased activities of NiO for H_2 generation and RuO_2 for N_2 activation. These findings also demonstrated that the thermodynamically unfavorable reaction of NH_3 formation from N_2 and H_2O can be produced under band-gap irradiation of these catalysts. Finally, it should be stressed that photodecomposition of ammonia becomes correspondingly important when the partial pressure of NH_3 in the cell is high.

E. Chemical Sensors

The development of reliable and selective solid-state gas sensors is crucial for many industrial

applications, among which environmental monitoring remains prominent.³¹⁸ A number of perovskite oxides (ABO_3) have been used as gas sensor materials because of their stability in thermal and chemical atmospheres. Since the gas-sensing function of semiconducting oxides mainly utilizes the change in the resistivity of semiconducting oxides under adsorption of gases, it is essential to understand several physical parameters, including the electrical conductivity, to develop gas sensors using perovskite oxides. Most perovskite-type LnBO_3 compounds are semiconductors, although LaNiO_3 and LaTiO_3 display metallic conductivity.³¹⁹ LaCoO_3 behaves as a semiconductor below 398 K because it mainly contains low spin Co^{III} , with a random distribution of high spin Co^{3+} .³²⁰ In the $398 < T < 1210$ K temperature range, conductivity increases much more rapidly with an increase in the temperature and is metallic above 1210 K, since the transition from localized to itinerant e_g electrons occurs in the form of a first-order phase transition.³²¹

Substantial changes occur in the conductivity of perovskite systems upon adsorption of gases on their surfaces. When reducing gases (CO , CH_3OH) are adsorbed on p-type LnMO_3 ($M = \text{Mn, Cr, Co}$) oxides, conductivity decreases.³²² This phenomenon can be represented by the following equations:



where (ad) denotes adsorbed species and (g) denotes a gaseous species. Since an electron is released upon adsorption, chemisorption of the reducing gases results in the loss of a conductivity hole through interaction with this free electron. These equations mean that the catalytic reaction occurs on the surface of perovskite oxides.

The application of gas sensors is limited by the stability of the perovskite phase in a reducing atmosphere at high temperatures. The stability of a series of perovskite-type oxides LaBO_3 ($B = \text{V, Cr, Mn, Fe, Co, Ni}$) was investigated by Nakamura et al.¹⁸ at 1273 K in gas mixtures of CO_2/H_2 . The stability sequence of these oxides was found to be $\text{LaCrO}_3 > \text{LaVO}_3 > \text{LaFeO}_3 > \text{LaMnO}_3 > \text{LaCoO}_3 > \text{LaNiO}_3$. Obayashi et al.³²³ employed $(\text{Ln, M})\text{BO}_3$ ($\text{Ln} = \text{rare earth}$, $M = \text{alkaline earth metal}$, and $B = \text{transition metal}$) to detect ethanol in exhaled air. In the presence of ethanol vapor, the electrical conductivity of these oxides changes drastically. This was the first example of perovskite oxides applied as gas sensors.

The activity for methanol sensing was found to be high for the LnCrO_3 and LnFeO_3 series. It is clear that the activities of these compounds are influenced by the transition metal ions and the rare earth ions. Rao and Bhide³²⁴ have suggested that the catalytic properties of these cobaltites would be connected to the spin states and, particularly, to the proportion of high-spin state Co^{3+} . It is noteworthy that the activity of rare earth cobaltites is the greatest for SmCoO_3 , which has the highest room temperature ratio of high-spin to low-spin cobalt ions. In $\text{Ln}_{1-x}\text{A}_x\text{BO}_3$ systems, the introduction of alkaline earth

ions results in the creation of a mobile hole. However, gas sensing activity may not be appreciably influenced by the number of holes, but rather by the depth of the trap centers of holes in these perovskite oxides.³²⁵ If Ln and A ions are fixed, B ions play a role in determining the gas-sensing activity. In the $\text{Sm}_{0.5}\text{Sr}_{0.5}\text{MO}_3$ system,³²⁴ the activity of the $\text{Sm}_{0.5}\text{Sr}_{0.5}\text{FeO}_3$ compound is higher than that of the $\text{Sm}_{0.5}\text{Sr}_{0.5}\text{CoO}_3$ homologue if the activity is compared by the response ratio alone. However, the $\text{Sm}_{0.5}\text{Sr}_{0.5}\text{CoO}_3$ compound shows the best tradeoff characteristics concerning both the response ratio and response time.

Orthoferrites can be either p- or n-type semiconductors, as indicated by Seebeck coefficient measurements.^{326,327} The n-type LnFeO_3 compounds exhibit a remarkable activity for methanol-sensing above the Néel temperature (T_N) of these oxides.³²⁸ The sensing activity appeared in the temperature ranges in which these oxides show paramagnetic behaviors. For the n-type LnFeO_3 oxides, activity increases as the radius of the rare earth ion (Ln) decreases, while T_N decreases with a decrease in the radius of the Ln ion. Orthochromites exhibit p-type conduction and are antiferromagnetic at the Néel temperature.³²⁹ The T_N of orthochromites is lower than the T_N of orthoferrites. The activity of orthochromites is expected to increase with the decrease in the radius of the rare earth ion, as in the case of orthoferrites, since T_N decreases going from La to Sm, i.e., 282, 214, and 190 K for LaCrO_3 , NdCrO_3 , and SmCrO_3 , respectively. However, there is no correlation between activity and the Néel temperature.

Ultrafine SmFeO_3 powders have been used for the preparation of thick films, screen-printed on alumina substrates.³³⁰ The electrical response of the films prepared from pastes of different compositions of an organic vehicle is very sensitive to CO and NO_2 in dry and wet air. However, the electrical conductivity and its activation energy, as well as the gas response of the films, which had similar microstructure, were strongly dependent on the composition of the organic vehicle. Since SmFeO_3 is a p-type semiconductor, unlike the commonly used n-type in gas sensors, there is an advantage for the detection of oxidizing gases, such as NO_2 , and for the preparation of sensor arrays for environmental monitoring or automotive applications.

Another application of perovskite oxides to gas sensors has been the measurement of oxygen pressure in combustion control systems. The requirements for controlling the fuel–air mixture to maintain a fixed concentration of excess oxygen, which is called “lean-burn control,” have received increasing attention with a view to increasing fuel efficiency as well as reducing pollutant components in the exhaust gases of vehicle engines. These oxygen sensors are divided into two groups, i.e., the solid electrolyte type, such as yttria-stabilized zirconia, and the semiconductor type such as titania³³¹ or $\text{Co}_{1-x}\text{Mg}_x\text{O}$.³³² Sensors using yttria-stabilized zirconia have been developed for use in lean-burn oxygen sensors. The semiconductor type sensors utilizing electrical conductivity changes due to oxygen adsorption or desorption have been the object of considerable interest

because of their simple structure and lower cost. TiO_2 was the first oxygen sensor of the semiconductor type used for control of the stoichiometric fuel–air mixture in car engine systems.³³³ However, TiO_2 cannot be used for sensing elements in the lean-burn region because the temperature coefficient of resistivity is too high, although titania has an advantage as regards chemical stability. On the other hand, lean-burn oxygen sensors using p-type semiconducting oxides, i.e., CoO ³³⁴ or $\text{Co}_{1-x}\text{Mg}_x\text{O}$ have the advantage in the lean-burn regions since the resistance of these oxides in such regions is low. Arai et al.^{335,336} observed that $\text{SrMg}_{0.4}\text{Ti}_{0.6}\text{O}_3$, among $\text{SrA}_x\text{Ti}_{1-x}\text{O}_3$ ($A = \text{Al}, \text{Mg}$), exhibits the largest change in resistance at the stoichiometric point of combustion. To obtain excellent lean-burn oxygen sensor it is necessary to continue the search for new materials with higher oxygen sensitivity and stability even at an extremely low oxygen partial pressure.

F. Electrocatalysis

1. Oxygen Reduction

Many semiconducting Pt-doped W bronzes,^{337,338} LaNiO_3 perovskites,^{339–341} and Sr-substituted $\text{Ln}_{1-x}\text{Sr}_x\text{NiO}_3$ perovskites^{341–344} are known to be effective electrocatalysts for the oxygen generation reaction in strong alkaline solutions. The Tafel slopes of oxygen generation appear to be dependent on the electrode material. However, a common mechanism consisting of the electrochemical adsorption of OH^- followed by the electrochemical desorption of OH (the rate-determining step), yielding H_2O_2 , as an intermediate, which then undergoes catalytic decomposition to O_2 , seems to be operative.

The reduction of oxygen in alkaline solutions has been chosen by several authors for kinetic investigations involving the evaluation of the rate-determining step. This reaction has been studied on both metals and metal oxides as electrode materials. Among the latter, RuO_2 remains prominent. On this oxide, the reaction was found to occur with the participation of lattice oxygen.³⁴⁵ Bockris and Ottagawa^{343,344} examined several substituted perovskites with a view to correlating their electrocatalytic properties with the electronic structure of the transition ions on the perovskite surface. These authors suggested that the most likely mechanism in the alkaline generation of O_2 involves a rate-determining $\text{M}^z\text{-OH}$ desorption step, where M^z is an orbital perpendicular to the surface of the transition element (M) in LnMO_3 perovskites.

Falcon et al.^{346,347} and Carbonio et al.³⁴⁸ have reported good catalytic activity for H_2O_2 decomposition and oxygen reduction over the perovskite system $\text{LaFe}_x\text{Ni}_{1-x}\text{O}_3$. The rate constant of H_2O_2 decomposition at 295 K in a 4 M KOH solution displayed a maximum for an $x = 0.25$ substitution. This result correlates with the isomer shift (δ) variations for Fe^{3+} and Fe^{4+} as measured by Mossbauer spectroscopy. The difference in the isomer shift between the two types of iron sites (Fe^{3+} and Fe^{4+}) also reaches a maximum for $x = 0.25$. Since the isomer shift is a direct measurement of the electron density surround-

ing the nucleus, it can be concluded that there is a maximum in the difference between the electron densities for the Fe^{3+} and Fe^{4+} sites in that composition. It is likely that both the mixed oxidation states for Fe and/or Ni and the unusual presence of Fe^{4+} sites may be factors involved in promoting the catalytic activity. In light of the classical explanation of H_2O_2 decomposition catalysis as proposed by Latimer,³⁴⁹ this correlation could be considered reasonable. Any redox couple that falls in the potential range between the O_2/HO_2^- and $\text{HO}_2^-/\text{OH}^-$ couples can, in principle, catalyze the decomposition reaction. The presence of both strongly oxidizing and strongly reducing species in $\text{LaFe}_x\text{Ni}_{1-x}\text{O}_3$ might accelerate the coupled HO_2^- oxidation and reduction reactions.

2. Solid Oxide Fuel Cells

Some perovskites display good performance as cathode materials in high temperature fuel cells. Solid oxide fuel cells (SOFCs) have recently attracted considerable interest as highly effective systems, efficiency ranging from 50 to 65%, and environmentally acceptable sources of electrical energy production.^{319,350–355} The most common SOFCs feed fuels are H_2 , CO, CH_4 , and other hydrocarbons.³⁵⁵ Moreover, an important advantage of SOFCs is that they can operate at temperatures at which the reaction rates reach values of practical interest.³⁵⁶ There are significant barriers to the reduction in the operating temperature of the SOFCs, i.e., electrolyte ohmic resistance and electrode overpotentials.

A representative electronic conductor is the $\text{La}_{1-x}\text{Sr}_x\text{MnO}_3$ type perovskites that have been extensively used as cathodes in ZrO_2 -based SOFCs.^{357,358} These are good electronic conductors, but the lack of oxide-ion vacancies, and therefore of oxide-ion conduction at the working temperatures, makes it necessary to use thick, porous electrodes containing an array of triple-phase boundaries where gas, electrolyte, and electrode meet. The cathode overpotentials, i.e., 20–300 mV, of such cathodes depend on their microstructure, which may change under the high temperatures required by the electrocatalytic reaction. By contrast, Sr-substituted cobaltites, $\text{La}_{1-x}\text{Sr}_x\text{CoO}_3$, contain oxide-ion vacancies in the bulk even in an oxidizing environment. These mixed oxide-ion and electronic conductors afford excellent cathode performance with very low overpotentials, even at high current density, when present as a film on the electrolyte.^{359,360} Apart from these advantages, the thermal expansion of $\text{La}_{1-x}\text{Sr}_x\text{CoO}_3$ perovskites is very high and the mismatch between the electrode and the electrolyte and interconnection makes this system unsuitable as cathode material for a SOFCs subject to repeated thermal cycling.

For decreasing the operating temperature, development of the active catalysts for electrode is essentially required in addition to the development of electrolyte with low resistivity. Although La^{3+} cations are generally used as the A-site cations of perovskite cathodes of SOFCs, rare earth cations used for the A-site of Mn-based perovskites have a great influence on the electrical conductivity as well as the cathodic overpotentials. Ishihara et al.³⁶¹ found that the Sr-

doped PrMnO_3 perovskite exhibited a low overpotential in a low-temperature range around 973 K and a thermal expansion coefficient consistent with YSZ. Although the mechanism for low overpotential on the Sr-doped PrMnO_3 is not clear, it seems likely that PrMnO_3 exhibits a high activity for the dissociation of oxygen molecule into oxide ions. Rare earth cations at the A-site in Co-based perovskite cathodes also had a significant effect on the power generation characteristics. In particular, a high power density could be attained in the temperature range from 973 to 1273 K by using a doped SmCoO_3 for the cathode.³⁶² Sr-doped SmCoO_3 exhibited the smallest cathodic overpotential resulting in the highest power density. Power density of the cell was maximum when $\text{Sm}_{0.5}\text{Sr}_{0.5}\text{CoO}_3$ was used as the cathode.

It is of great importance for the intermediate temperature SOFCs to develop new electrolyte materials, which show a high oxide ion conduction over a wide range of oxygen partial pressures. It was reported that the LaGaO_3 -based perovskite oxides exhibit high ion conductivity,³⁶³ which is comparable to that of CeO-based oxide. In particular, LaGaO_3 doped with Sr for La and Mg for Ga (denoted as LSGM) exhibits a high oxide ion conductivity stable over a wide range of oxygen pressures.^{364,365} Ishihara et al.³⁶⁶ prepared Fe-doped LSGM electrolyte and found an increase in the power density of the fuel cell with respect to the undoped LSMG counterpart. This can be explained by the decrease in electrical resistance loss by improving the oxide ion conductivity. A maximum power density close to 700 mW cm^{-2} was obtained at 1073 K on the cell using an Fe-doped LSGM and oxygen as electrolyte and oxidant, respectively, which is close to the theoretical open-circuit potential. On the other hand, the power density was slightly smaller than that of the cell using Co-doped LSGM as electrolyte, especially at temperatures below 973 K.³⁶⁷ This may result from the large activation energy for ion conduction.

Tu et al.³⁵⁴ prepared $\text{Ln}_{0.4}\text{Sr}_{0.6}\text{Co}_{0.8}\text{Fe}_{0.2}\text{O}_{3-\delta}$ ($\text{Ln} = \text{La, Pr, Nd, Sm, Gd}$) perovskites and found semiconductor-like behavior at lower temperatures and metallic conduction at higher temperatures. $\text{Nd}_{0.4}\text{Sr}_{0.6}\text{Co}_{0.8}\text{Fe}_{0.2}\text{O}_{3-\delta}$ exhibited the highest conductivity in the 300–1300 K temperature range and simultaneously showed the best catalytic activity for oxygen reduction at intermediate temperatures (870–1070 K). A large thermal expansion mismatch between these perovskite oxides and the 8% mol Y_2O_3 -doped ZrO_2 (YSZ) electrolyte was reported. The transformation of the Co^{4+} and Fe^{4+} states to the trivalent states causes the precipitation of Sr at higher temperatures, resulting in the reaction of Sr with ZrO_2 to form SrZrO_3 . The formation of an interfacial reaction between the YSZ and calcium-substituted chromite anodes was also observed during electrochemical tests under fuel cell conditions. Using energy-dispersive X-rays and photoelectron spectroscopy techniques, Sfeir et al.³⁵³ showed that under such reducing conditions, the Ca-substituted chromite anodes are enriched with Ca and Cr at the surface. The CaCrO_4 phase is believed to exsolve from these materials and to decompose to CaCr_2O_4 and CaO ,

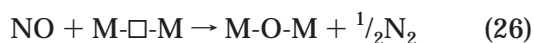
which eventually reacts with the YSZ electrolyte to form CaZrO_3 . This phase segregation is also believed to affect the activity of these anodes toward fuel oxidation.

Other mixed-valent perovskites designed to display a thermal expansion better matched to that of the electrolyte and interconnection and also to be good mixed electronic and oxide-ion conductors in an oxidizing environment at $970 < T < 1300$ K have been explored.³¹⁹ For this purpose, Huang et al.³¹⁹ used the $\text{Ni}^{3+}/\text{Ni}^{2+}$ redox couple in association with the $\text{Fe}^{4+}/\text{Fe}^{3+}$ and the low-spin/intermediate-spin $\text{Co}^{4+}/\text{Co}^{3+}$ couples in the perovskite structure. The electric conductivity of both $\text{La}_{1-x}\text{Sr}_x\text{Ni}_{1-y}\text{Co}_y\text{O}_3$ and $\text{La}_{1-x}\text{Sr}_x\text{Ni}_{1-y}\text{Fe}_y\text{O}_3$ perovskites appears to be polaronic with an overlap of the $\text{Co}^{4+}/\text{Co}^{3+}$ and $\text{Ni}^{3+}/\text{Ni}^{2+}$ in the former and of $\text{Fe}^{4+}/\text{Fe}^{3+}$ and $\text{Ni}^{3+}/\text{Ni}^{2+}$ couples in the latter. This overlap provides two types of polaronic conduction, p-type and n-type, with the p-type carriers moving on the Co- or Fe-atom array, and the n-type carriers moving on the Ni-atom array. The compositions $\text{La}_{0.8}\text{Sr}_{0.2}\text{Ni}_{0.2}\text{Co}_{0.8}\text{O}_3$ and $\text{La}_{0.7}\text{Sr}_{0.3}\text{Ni}_{0.2}\text{Fe}_{0.8}\text{O}_3$ have a thermal expansion coefficient better matched to that of the electrolyte than the expansion coefficient of $\text{La}_{0.8}\text{Sr}_{0.2}\text{CoO}_3$, and they show a comparable electrode resistance at temperatures above 970 K. In contrast to the $\text{La}_{1-x}\text{Sr}_x\text{MnO}_3$ cathode, these oxides lose oxygen reversibly at temperatures above 870 K, which makes them mixed electronic/oxide-ion conductors with good catalytic activity for oxygen reduction in SOFCs.

G. Structure–Activity Relationships

Precise knowledge of the relationships between solid-state properties and catalytic performance is crucial for the design and tailoring of efficient catalysts. In the search for these relationships, the availability of families of isostructural perovskite-type oxides characterized by a great flexibility of the crystal to accommodate cation substitutions is extremely useful. There is no doubt that the structure and composition of ABO_3 model perovskites facilitate this arduous but extremely important task. By changing the A cation while keeping the B cation constant, or vice versa, a series of compounds may be synthesized with no substantial modification of the crystal structure, provided that the conditions for the lower limits of the ionic radii are met and that the relationship between the ionic radii and the tolerance factor (t) as defined by Goldschmidt⁷ is obeyed.

The reduction of NO is an example of an intrafacial process. This reaction occurs through dissociative chemisorption of the NO molecule on an oxygen vacancy (\square) present on the surface of cobaltite and manganite perovskites:^{47,154}



In this reaction, the reduced and oxidized surfaces are represented by $[\text{M}-\square-\text{M}]$ and $[\text{M}-\text{O}-\text{M}]$, respectively. Lanthanum manganites provide a suitable example of the effect of oxygen binding energy on their catalytic performance for the target reaction. On the basis of a thermodynamic approach to esti-

mate the binding energy of surface oxygen in a series of manganites, Voorhoeve et al.³⁶⁸ observed that increasing activity for NO decomposition coincides with the decreasing order of the binding energy of surface oxygen. This finding was taken as conclusive that the binding energy of oxygen determines the number of oxygen vacancies (active sites) and hence activity.³⁶⁸ Another example of the influence of the binding energy between the oxygen and the lanthanide cation has been reported by Futai et al.⁹⁵ in LnCoO_3 ($\text{Ln} = \text{La}-\text{Dy}$) oxides. These authors found a correlation between the sum of the Ln-O and Co-O binding energies, reducibility, and the catalytic activity in CO oxidation. Maximum activity corresponded to EuCoO_3 , which exhibited the lowest oxygen binding energy and was also the oxide that proved to be the easiest to reduce.

A correlation with the electronic parameters of the perovskite oxide is, however, more appropriate in suprafacial catalytic processes.³⁶⁸ In these reactions, the solid surface serves as a template providing electronic orbitals of the proper energy and symmetry for the bonding of reagents and intermediates. Sazonov et al.³⁶⁹ studied the oxygen equilibration:



on LaMO_3 (M, first-row transition metal from Cr through to Ni) oxides and found the rate and activation energy of the oxygen equilibration above 500 K to be maximum for LaMnO_3 and LaCoO_3 , very similar in fact to those of simple oxides of transition metals (M_2O_3). However, the temperature dependence of the rate of equilibration on LnMO_3 ($\text{Ln} = \text{La}, \text{Nd}, \text{Sm}$) oxides below 500 K was found to be of an identical nature to that recorded on the corresponding rare earth oxides. Thus, a distinct separation of the functions of the cations of the transition and rare earth elements can be seen for these perovskites, i.e., activity is determined by the cations of the transition metals at high temperature and by the rare earth ions at low temperature. These results are in agreement with those reported by Kremenec et al.⁴⁹ for propene and isobutene oxidation at 573 K (Figure 8). The twin-peak patterns in catalytic activity profiles resemble the twin-pattern which is found on going from d^0 to d^{10} cations in the change in the crystal field stabilization energy caused by the change in the coordination of surface M^{3+} cations upon oxygen adsorption.³⁷⁰ These results suggest a close relationship between the electronic configuration of the transition metal ion (M) and catalytic activity.

The oxidation of CO with molecular oxygen has also been suggested as an example of suprafacial processes. Voorhoeve et al.,^{159,368,371} Shimizu,³⁷² and Tascon and Tejuca¹⁶⁵ have shown a volcano-type dependence between the activity for CO oxidation and the electronic configuration of the transition metal ion. This is illustrated in the plot of catalytic activity, either as the reciprocal of the reaction temperature at which the activity is $1\ \mu\text{mol}$ of CO converted per square meter of catalyst per second or as the rate of mole CO transformed per unit area and unit time (Figure 14) as a function of the occupancy

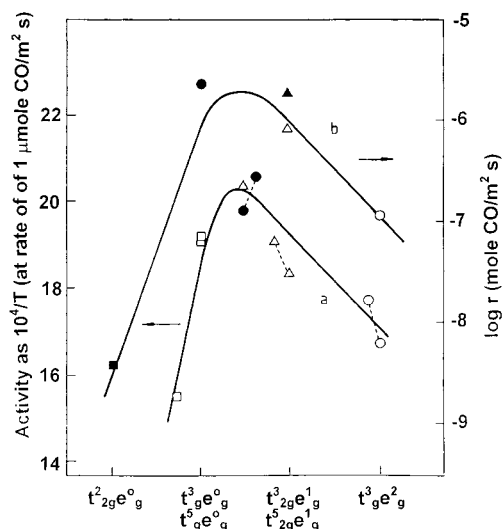


Figure 14. Activity of first-row transition metal oxide perovskites for CO oxidation in a CO:O₂ = 2:1 mixture (a) or in a CO:O₂ = 2:1 mixture at 500 K. The activities of vanadates (■), chromates (□), manganates (△), ferrates (○), cobaltates (●), and nikelates (▲) are plotted at the appropriate d orbital occupation. Reprinted from ref 104 by permission of the publisher. Copyright 1989 by Academic Press.

of the d levels for the transition M³⁺ ion. Catalytic activity is also influenced by its stoichiometry. In ABO₃ perovskites, a simple way of varying the oxidation state of the B³⁺ ion is by substitution of the A³⁺ ion by a different one with an oxidation state other than 3. For (La,A')CoO₃ systems, the appearance of Co⁴⁺ ions by substitution with A' = Sr decreases the rate, whereas the presence of Co²⁺ ions by introduction of A' = Ce⁴⁺ enhances the rate of CO oxidation. Variations in the valence states can be also achieved by partial reduction, within the homogeneity ranges of the perovskite systems.

According to crystal field theory, the octahedral (truncated octahedron at the surface) environment of the M³⁺ ions splits into two levels: the lower one (*t*_{2g}) contains orbitals that are repulsed less by negative point charges than are the orbitals in the higher energy (*e*_g) level. In both cases, the maximum activity in the volcano curves is attained for an occupation of the *e*_g levels of less than one electron whereas the *t*_{2g} levels remain half-filled or completely filled. This correlation can be understood in terms of the kinetic data, which show that the binding of CO to the surface is a critical part of the process since the reaction rate varies with the partial pressure of CO. Regarding the binding of CO as a carbonyl to transition metals, binding is optimal when donation of the carbon lone pair into the d_{z²} metal orbital and simultaneous back-donation of *t*_{2g} electrons to the antibonding π* orbital of CO are possible.³⁷³ The correlation of the rate with the occupation of 3d orbitals is therefore consistent with the kinetic data and a mechanistic view based on molecular orbital arguments.

V. Future Perspectives

Historically, the initial interest of perovskites in the middle 70s was focused on their application as

catalysts for removal of exhaust gases. However, this impetus has declined, mainly because of their lower resistance of perovskites to poisoning by sulfur dioxide as compared with noble metals. The knowledge of interactions of sulfur dioxide with the surface of perovskite oxides still remains limited, and most of the conclusions regarding their behavior in a sulfur dioxide environment have been extrapolated from the available data from single oxides. This weakness certainly warrants further research on the subject.

The relationship between solid-state properties and catalytic performance is crucial for the design and tailoring of efficient catalysts. The availability of families of isostructural perovskite-type oxides characterized by a great flexibility of the crystal to accommodate cation substitutions, or anion vacancies, is extremely useful. This is illustrated by the formation heat of an oxygen vacancy in several unsubstituted and substituted manganites which appears to be related to the binding energies of the surface oxygen to the A-sites. The increasing order of values of this sum was found to coincide with the decreasing order in catalytic activity for NO decomposition. This indicates that the binding energy of oxygen determines the number of oxygen vacancies, and therefore the number of active sites, and hence the activity of manganites in NO decomposition. Similar correlations between performance and solid-state properties are expected for catalytic reactions in which O vacancies are involved.

Some perovskites display good performance as cathode materials in high temperature fuel cells (SOFC), although inherent barriers to the reduction in operating temperature of the SOFCs must be overcome, i.e., electrolyte ohmic resistance and electrode overpotentials. Some Sr-substituted cobaltites can act as mixed oxide-ion and electronic conductors and afford excellent cathode performance with very low overpotentials, even at high current density, when present as a film on the electrolyte. Apart from these advantages, the thermal expansion of those perovskites is very high, and the mismatch between the electrode and the electrolyte and interconnection makes this system unsuitable as cathode material for a SOFCs subject to repeated thermal cycling. There is obviously a need to develop new mixed oxygen anion- and electron-conducting membranes derived from perovskite structures for the production of new, clean energy vectors, e.g., hydrogen, and SOFCs applications.

An important characteristic of perovskite oxides, mentioned in the preceding sections, is their susceptibility of partial substitution in both A and B positions. Because of the wide range of ions and valences which this simple crystal structure can accommodate, the perovskites lend themselves to chemical tailoring. They are relatively simple to synthesize because the flexibility of the structure to diverse chemistry. In light of the many possibilities of perovskites as catalysts, it is anticipated that further investigations will expand the scope of catalytic perspectives examined in this review and contribute to the development of practical processes.

VI. Acknowledgment

This work was partially supported by the Inter-ministerial Commission of Science and Technology under Projects QUI98-0887 and QUI98-1655-CE.

VII. References

- (1) *Catalytic Chemistry of Solid State Inorganics*, Moser, W. R., Ed.; New York Academy of Sciences: New York, 1976.
- (2) Centi, G.; Trifiro, F. *Catal. Rev.-Sci. Eng.* **1986**, *28*, 165.
- (3) Mizuno, N.; Misono, M. *Chem. Rev.* **1998**, *98*, 199.
- (4) *Properties and Applications of Perovskite Type Oxides*; Tejuca, L. J., Fierro, J. L. G., Eds.; Marcel Dekker: New York, 1993.
- (5) Bednorz, J. G.; Muller, K. A. *Angew. Chem. Ed. Engl.* **1988**, *100*, 757.
- (6) Raveau, B. *Proc. Indian Natl. Sci. Acad. Part A* **1986**, *52*, 67.
- (7) Goldschmidt, V. M. Skr. Nor. Viedenk.-Akad., Kl. I: Mater.-Naturvidensk. Kl. 1926, No. 8.
- (8) Megaw, H. D. *Proc. Phys. Soc.* **1946**, *58*, 133.
- (9) Khattak, C. P.; Wang, F. F. Y. In *Handbook of the Physics and Chemistry of Rare Earths*; Gschneider, K. A. Jr.; Eyring, L., Eds.; North-Holland Publisher: Amsterdam, 1979; p 525.
- (10) Goodenough, J. B.; Longo, J. M. In *Landolt-Bronstein New Series*; Hellwege, K. H., Hellwege, A. M., Eds.; Springer-Verlag: Berlin; Vol. 4, part a, p 126.
- (11) Goodenough, J. B. In *Solid State Chemistry*; Rao, C. N. R., Ed.; Marcel Dekker: New York, 1974; p 215.
- (12) Rao, C. N. R.; Gopalakrishnan, J.; Vidyasagar, K. *Indian J. Chem. Sect. A* **1984**, *23A*, 265.
- (13) Smyth, D. M. *Annu. Rev. Mater. Sci.* **1985**, *15*, 329.
- (14) Smyth, D. M. in *Properties and Applications of Perovskite-Type Oxides*; Tejuca, L. G., Fierro, J. L. G., Eds.; Marcel Dekker: New York, 1993; p. 47.
- (15) Sayagues, M. J.; Vallet-Regi, M.; Caneiro, A.; Gonzalez-Calbet, J. M. *J. Solid State Chem.* **1994**, *110*, 295.
- (16) Tofield, B. C.; Scott, W. R. *J. Solid State Chem.* **1974**, *10*, 183.
- (17) Voorhoeve, R. J. H.; Remeika, J. P.; Trimble, L. E.; Cooper, A. S.; Disalvo, F. J.; Gallagher, P. K. *J. Solid State Chem.* **1975**, *14*, 395.
- (18) Vogel, E. M.; Johnson, D. W. Jr.; Gallagher, P. K. *J. Am. Ceram. Soc.* **1977**, *60*, 31.
- (19) Taguchi, H.; Sugita, A.; Nagao, M.; Tabata, K. *J. Solid State Chem.* **1995**, *119*, 164.
- (20) Kamegashira, N.; Miyazaki, Y.; Yamamoto, H. *Mater. Chem. Phys.* **1984**, *11*, 187.
- (21) Mizusaki, J.; Tagawa, H.; Naraya, K.; Sasamoto, T. *Solid State Ion.* **1991**, *49*, 111.
- (22) Van Roosmalen, J. A. M.; Cordfunke, E. H. P. *J. Solid State Chem.* **1994**, *110*, 100.
- (23) Mizusaki, J.; Mori, N.; Takai, H.; Yonemura, Y.; Minamiue, H.; Tagawa, H.; Dokiya, M.; Inaba, H.; Naraya, K.; Sasamoto, T.; Hashimoto, T. *Solid State Ion.* **2000**, *129*, 163.
- (24) Anderson, M. T.; Vaughey, J. T.; Poeppelmeier, K. R. *Chem. Mater.* **1993**, *5*, 151.
- (25) Crespin, M.; Levitz, P.; Gatineau, L. *J. Chem. Soc., Faraday Trans.* **1983**, *79*, 1181.
- (26) Rao, C. N. R.; Gopalakrishnan, J.; Vidyasagar, K.; Ganguly, A. K.; Ramanan, A.; Ganapathi, L. *J. Mater. Res.* **1986**, *1*, 280.
- (27) Bringley, J. F.; Scott, B. A.; La Placa, S. J.; Boehme, R. F.; Shaw, T. M.; McElfresh, M. W.; Trail, S. S.; Cox, D. E. *Nature* **1990**, *347*, 263.
- (28) Bringley, J. F.; Scott, B. A.; La Placa, S. J.; McGuire, T. R.; Mehran, F.; McElfresh, M. W.; Cox, D. E. *Phys. Rev. B* **1993**, *47*, 15269.
- (29) Karpinnen, M.; Yamaguchi, H.; Suematsu, H.; Fukunaga, O. *Physica C* **1996**, *264*, 268.
- (30) Falcon, H.; Martinez-Lope, M. J.; Alonso, J. A.; Fierro, J. L. G. *Appl. Catal. B: Environmental* **2000**, *26*, 131.
- (31) Han, Y. H.; Harmer, M. P.; Hu, Y. H.; Smyth, D. M. In *Transport in Non-stoichiometric Compounds*; Simkovich, G., Stubican, V. S., Eds.; Plenum: New York, 1985; p. 73.
- (32) Chan, N. H.; Sharma, R. K.; Smyth, D. M. *J. Am. Ceram. Soc.* **1981**, *64*, 448.
- (33) *Handbook of the Physics and Chemistry of Rare Earths*; Gschneider, K. A. Jr.; Eyring, L., Eds.; North-Holland Publishers: Amsterdam, 1979; p 553.
- (34) Akimitsu, J.; Suzuki, S.; Watanabe, M.; Sawa, H. *Jpn. J. Appl. Phys.* **1988**, *27*, L1859.
- (35) Labbe, J.; Bok, J. *Europhys. Lett.* **1987**, *3*, 1225.
- (36) Blasse, G. *Prog. Solid State Chem.* **1988**, *18*, 79.
- (37) Butler, M. A.; Ginley, D. S. *J. Mater. Sci.* **1980**, *51*, 1.
- (38) Blasse, G.; de Korte, P. H. M.; Mackor, A. *J. Inorg. Chem.* **1981**, *43*, 1499.
- (39) Tascon, J. M. D.; Tejuca, L. G.; Rochester, C. H. *J. Catal.* **1985**, *95*, 558.
- (40) Petunchi, J. O.; Nicastro, J. L.; Lombardo, E. A. *J. Chem. Soc., Chem. Commun.* **1980**, 467.
- (41) Tascon, J. M. D.; Tejuca, L. G. *Z. Phys. Chem. (Wiesbaden)* **1980**, *121*, 63.
- (42) Peña, M. A.; Tascon, J. M. D.; Fierro, J. M. D.; Tejuca, L. G. *J. Colloid Interface Sci.* **1987**, *119*, 100.
- (43) Tejuca, L. G.; Bell, A. T.; Fierro, J. L. G.; Tascon, J. M. D. *J. Chem. Soc., Faraday Trans. 1* **1987**, *83*, 3149.
- (44) Tejuca, L. G.; Bell, A. T.; Fierro, J. L. G.; Peña, M. A. *Appl. Surf. Sci.* **1988**, *31*, 301.
- (45) Peña, M. A.; Tascon, J. M. D.; Tejuca, L. G. *Nouv. J. Chim.* **1985**, *9*, 591.
- (46) Olivan, A. O. M.; Peña, M. A.; Tascon, J. M. D.; Tejuca, L. G. *J. Mol. Catal.* **1988**, *45*, 355.
- (47) Tascon, J. M. D.; Olivan, A. M. O.; Tejuca, L. G.; Bell, J. *Phys. Chem.* **1986**, *90*, 791.
- (48) Yao, H. C.; Shelef, M. *J. Phys. Chem.* **1974**, *78*, 2490.
- (49) Kremenec, G.; Nieto, J. M. L.; Tascon, J. M. D.; Tejuca, L. G. *J. Chem. Soc., Faraday Trans. 1* **1985**, *81*, 939.
- (50) Iwamoto, M.; Yoda, Y.; Yamazoe, N.; Seiyama, T. *J. Phys. Chem.* **1982**, *72*, 2564.
- (51) Nakamura, T.; Misono, M.; Yoneda, Y. *Bull. Chem. Soc. Jpn.* **1982**, *55*, 394.
- (52) Yamazoe, N.; Teraoka, Y.; Seiyama, T. *Chem. Lett.* **1981**, 1767.
- (53) Seiyama, T.; Yamazoe, N.; Eguchi, K. *Ind. Eng. Chem., Prod. Res. Dev.* **1985**, *24*, 19.
- (54) Nitadori, T.; Misono, M. *J. Catal.* **1985**, *93*, 459.
- (55) Ferri, D.; Forni, L. *Appl. Catal. B: Environmental* **1998**, *16*, 119.
- (56) Ponce, S.; Peña, M. A.; Fierro, J. L. G. *Appl. Catal. B: Environmental* **2000**, *24*, 193.
- (57) Yokoi, Y.; Uchida, H. *Catal. Today* **1998**, *42*, 167.
- (58) Zhao, Z.; Yang, X.; Wu, Y. *Appl. Catal. B: Environ.* **1996**, *6*, 281.
- (59) Tsukuda, M.; Satoko, H.; Adachi, H. *J. Phys. Soc. Jpn.* **1980**, *48*, 200.
- (60) Au, C. T.; Chen, K. D.; Dai, H. X.; Liu, Y. W.; Luo, J. Z.; Ng, C. F. *J. Catal.* **1998**, *179*, 300.
- (61) Berndt, U.; Maier, D.; Keller, C. *J. Solid State Chem.* **1975**, *13*, 131.
- (62) Johnson, D. W. Jr.; Gallagher, P. K.; Schrey, F.; Rhodes, W. W. *Am. Ceram. Soc. Bull.* **1976**, *55*, 520.
- (63) Keshavaraja, A.; Ramaswamy, A. V. *Ind. J. Eng. Mater. Sci.* **1994**, *1*, 229.
- (64) Jain, A. N.; Tiwari, S. K.; Singh, R. N.; Chartier, P. *J. Chem. Soc., Faraday Trans.* **1995**, *91*, 1887.
- (65) Teraoka, Y.; Nanri, S.; Moriguchi, I.; Kagawa, S.; Shimanoe, K.; Yamazoe, N. *Chem. Lett.* **2000**, 1202.
- (66) Nakajima, Y.; Ogura, T.; Kinoshita, M.; Komirama, T. *Chem. Express* **1989**, *4*, 225.
- (67) Ho, S.; Park, I. H. *J. Korean Chem. Soc.* **1994**, *38*, 276.
- (68) Taguchi, H.; Yoshioka, H.; Naguo, M. *J. Mater. Sci. Lett.* **1994**, *13*, 891.
- (69) Li, X.; Zhang, H.; Chi, F.; Li, S.; Xu, B.; Zhao, M.; *Mater. Sci. Eng.* **1993**, *B18*, 209.
- (70) Park, H. B.; Kwon, H. J.; Kim, S. J.; Kim, K. *J. Korean Chem. Soc.* **1994**, *38*, 852.
- (71) Shimizu, Y.; Murata, T. *J. Am. Ceram. Soc.* **1997**, *80*, 2702.
- (72) Tiwaris, K.; Chartier, P.; Singh, N. R. *J. Electrochem. Soc.* **1995**, *142*, 148.
- (73) Xiong, G.; Zhi, Z. L.; Yang, X.; Lu, L.; Wang, X. *J. Mater. Sci. Lett.* **1997**, *16*, 1064.
- (74) Wang, X.; Li, D.; Lu, L.; Wang, X. *J. Alloy Compounds* **1996**, *237*, 45.
- (75) Gregg, S. J.; Sing, K. S. W. *Adsorption, Surface Area and Porosity*; Academic Press: London, 1952.
- (76) Nicholson, D.; Silvester, R. G. *J. Colloid Interface Sci.* **1977**, *62*, 447.
- (77) Ioroi, T.; Hara, T.; Uchimoto, Y.; Ogumi, Z.; Takehara, Z. *J. Electrochem. Soc.* **1998**, *145*, 1999.
- (78) Li, A.; Wu, D.; Liu, Z.; Ge, C.; Liu, X.; Chen, G.; Ming, N. *Thin Solid Films* **1998**, *336*, 386.
- (79) Nanako, M.; Izumi, M.; Konishi, Y.; Kobayashi, K.; Kawasaki, M.; Tokura, Y. *Appl. Phys. Lett.* **1999**, *74*, 2215.
- (80) Yu, T.; Chen, Y. F.; Liu, Z. G.; Chen, X. Y.; Sun, L.; Ming, N. B.; Shi, L. *J. Mater. Lett.* **1996**, *26*, 73.
- (81) Tanaka, H.; Tabata, H.; Kawai, T. *Thin Solid Films* **1999**, *342*, 4.
- (82) Shlom, D. G.; Eckstein, J. N.; Hellman, E. S.; Streiffer, S. K.; Harris, J. S. Jr.; Beasley, M. R.; Bravman, J. C.; Geballe, T. H.; Webb, C.; Von Dessenneck, K. E.; Turner, F. *Appl. Phys. Lett.* **1988**, *53*, 1660.
- (83) Terashita, T.; Bando, Y.; Iijima, K.; Yamamoto, K.; Hirota, K.; Hayashi, K.; Kamigaki, K.; Terauchi, H. *Phys. Rev. Lett.* **1990**, *65*, 2684.
- (84) Okada, M.; Tominaga, K.; Araki, T.; Katayama, S.; Sakashita, Y. *Jpn. J. Appl. Phys.* **1990**, *29*, 718.
- (85) Akizuki, M.; Matsuo, J.; Qin, W.; Aoki, T.; Harada, M.; Ogasawara, S.; Yodoshii, K.; Yamada, I. *Mater. Chem. Phys.* **1998**, *54*, 255.
- (86) Izumi, M.; Konishi, Y.; Nishihara, K.; Hayashi, S.; Shiohara, M.; Kawasaki, M.; Tokura, Y. *Appl. Phys. Lett.* **1998**, *73*, 2497.

- (87) Gallagher, P. K.; Johnson, D. W. Jr.; Schrey, F. *Mater. Res. Bull.* **1974**, *9*, 1345.
- (88) Mizuno, N.; Fujii, H.; Misono, M. *Chem. Lett.* **1986**, 1333.
- (89) Nudel, J. N.; Umansky, B. S.; Lombardo, E. A. *Appl. Catal.* **1987**, *31*, 275.
- (90) Schneider, R.; Kiessling, D.; Wendt, G.; Burckhardt, W.; Winterstein, G. *Catal. Today* **1999**, *47*, 429.
- (91) Ciambelli, P.; Palma, V.; Tikhov, S. F.; Sadykov, S. V.; Isupova, L. A.; Lisi, L. *Catal. Today* **1999**, *47*, 199.
- (92) Podyacheva, O. Yu.; Ketov, A. A.; Ismagilov, Z. R.; Ushakov, V. A.; Bos, A.; Veringa, H. J. *React. Kinet. Catal. Lett.* **1997**, *60*, 243.
- (93) Klvana, D.; Kirchnerova, J.; Chaouki, J.; Delval, J.; Yaici, W. *Catal. Today* **1999**, *47*, 115.
- (94) Arakawa, T.; Ohara, N.; Shiokawa, J. *J. Mater. Sci.* **1986**, *21*, 1824.
- (95) Futai, M.; Yonghua, C.; Hui, L. *React. Kinet. Catal. Lett.* **1986**, *31*, 47.
- (96) Carreiro, L.; Qian, Y. T.; Kershaw, R.; Dwight, K.; Wold, A. *Mater. Res. Bull.* **1985**, *20*, 619.
- (97) Katsura, T.; Sekine, T.; Kitayama, K.; Sugihara, T.; Kimizuka, T. *J. Solid State Chem.* **1978**, *23*, 43.
- (98) Katsura, T.; Kitayama, K.; Sekine, T.; Sugihara, T.; Kimizuka, T. *Bull. Chem. Soc. Jpn.* **1975**, *48*, 1809.
- (99) Marcos, J. A.; Buitrago, R. H.; Lombardo, E. A. *J. Catal.* **1987**, *105*, 95.
- (100) Nakamura, T.; Petzow, G.; Gauckler, L. J. *Mater. Res. Bull.* **1979**, *14*, 649.
- (101) Vogel, E. M.; Johnson, D. W. *Thermochim. Acta* **1975**, *12*, 49.
- (102) Crespín, M.; Hall, W. K. *J. Catal.* **1981**, *69*, 359.
- (103) Fierro, J. L. G.; Tejuca, L. G. *J. Catal.* **1984**, *87*, 126.
- (104) Tejuca, L. G.; Fierro, J. L. G.; Tascon, J. M. D. *Adv. Catal.* **1989**, *36*, 237.
- (105) Lago, R.; Bini, G.; Peña, M. A.; Fierro, J. L. G. *J. Catal.* **1997**, *167*, 198.
- (106) Tascon, J. M. D.; Fierro, J. L. G.; Tejuca, L. G. In *Properties and Applications of Perovskite-Type Oxides*; Tejuca, L. G., Fierro, J. L. G., Eds.; Marcel Dekker: New York, 1993; p 171.
- (107) Tejuca, L. G.; Rochester, C. H.; Fierro, J. L. G.; Tascon, J. M. D. *J. Chem. Soc., Faraday Trans. 1* **1984**, *80*, 1089.
- (108) Martin, M. A.; Fierro, J. L. G.; Tejuca, L. G. *Z. Phys. Chem. (Wiesbaden)* **1981**, *127*, 237.
- (109) Sokolovskii, V. D.; Aliev, G. M.; Buyevskaya, O. V.; Davydov, A. A. *Catal. Today* **1989**, *4*, 293.
- (110) Ding, W.; Chen, Y.; Fu, X. *Appl. Catal. A: General* **1993**, *104*, 61.
- (111) Dissanayake, D.; Kharas, K. C. C.; Lunsford, J. H.; Rosynek, M. P. *J. Catal.* **1993**, *139*, 652.
- (112) Tejuca, L. G.; Bell, A. T.; Cortes, V. *Appl. Surf. Sci.* **1989**, *37*, 353.
- (113) Cortes, V.; Tejuca, L. G.; Bell, A. T. *J. Mater. Sci.* **1989**, *24*, 4437.
- (114) Tejuca, L. G.; Fierro, J. L. G. *Thermochim. Acta* **1989**, *147*, 361.
- (115) Kawai, T.; Kunimori, K.; Kondow, T.; Onishi, T.; Tamaru, K. *Z. Phys. Chem. NF* **1973**, *86*, 268.
- (116) Petit, P. E.; Teymour, M.; Roger, A. C.; Hehspringer, J. L.; Hilaire, L.; Kiennemenn, A. *Stud. Surf. Sci. Catal.* **1995**, *108*, 607.
- (117) Hinson, P. G.; Clearfield, A.; Lunsford, J. H. *J. Chem. Soc. Chem. Commun.* **1991**, 1430.
- (118) Seiyama, T. In *Properties and Applications of Perovskite-type Oxides*; Tejuca, L. G., Fierro, J. L. G., Eds.; Marcel Dekker: New York, 1993; p 215.
- (119) Fierro, J. L. G.; Peña, M. A.; Tejuca, L. G. *J. Mater. Sci.* **1988**, *23*, 1018.
- (120) Keattch, C. J.; Dollimore, D. In *An Introduction to Thermogravimetry*, 2nd Ed.; Heyden: London; 1975; p 63.
- (121) Fierro, J. L. G.; Tascon, J. M. D.; Tejuca, L. G. *J. Catal.* **1985**, *93*, 83.
- (122) Falcon, H.; Baranda, J.; Campos-Martin, J. M.; Peña, M. A.; Fierro, J. L. G. *Stud. Surf. Sci. Catal.* **2000**, *130*, 2195.
- (123) Crespín, M.; Levitz, P.; Gatinéau, L. *J. Chem. Soc., Faraday Trans. 1* **1983**, *79*, 1181.
- (124) Kobylinski, T. P.; Kibby, C. L.; Pannell, R. B.; Eddy, E. L. *US Patent 4,670,414*, 1987.
- (125) Kobylinski, T. P.; Kibby, C. L.; Pannell, R. B.; Eddy, E. L. *US Patent 4,729,981*, 1988.
- (126) Lin, Y. S.; Wan, W.; Han, J. *AIChE J.* **1994**, *40*, 786.
- (127) Teraoka, Y.; Zhang, H. M.; Okamoto, K.; Yamazoe, N. *Mater. Res. Bull.* **1988**, *3*, 51.
- (128) Teraoka, Y.; Nobunaga, K.; Okamoto, K.; Miura, N.; Yamazoe, N. *Solid State Ion.* **1991**, *48*, 207.
- (129) van Hassel, B. A.; ten Elshof, J. E.; Bouwmester, H. J. M. *Appl. Catal. A: General* **1994**, *119*, 279.
- (130) ten Elshof, J. E.; Bouwmester, H. J. M.; Verweij, H. *Solid State Ion.* **1995**, *81*, 97.
- (131) Stevenson, J. W.; Armstrong, T. R.; Carneim, B. D.; Pederson, L. R.; Weber, L. W. *J. Electrochem. Soc.* **1996**, *143*, 2722.
- (132) Bouwmester, H. J. M.; Kruidhof, H.; Burggraaf, A. J. *Solid State Ion.* **1994**, *72*, 185.
- (133) Qiu, L.; Lee, T. H.; Liu, L. M.; Yang, Y. L.; Jacobson, A. J. *Solid State Ion.* **1995**, *76*, 321.
- (134) Kharton, V. V.; Naumovich, E. N.; Nikolaev, A. V. *Solid State Phenom.* **1994**, *39–40*, 147.
- (135) Kharton, V. V.; Nikolaev, A. V.; Naumovich, E. N.; Samokhval, V. V. *Inorg. Mater.* **1994**, *30*, 492.
- (136) Balachandran, U.; Dusek, J. T.; Sweeney, S. M.; Poeppel, R. B.; Mieville, R. L.; Maiya, P. S.; Kleefish, M. S.; Pei, S.; Kobylinski, T. P.; Udovich, C. A. *Am. Ceram. Soc. Bull.* **1995**, *74*, 71.
- (137) Tsai, C. Y.; Dixon, A. G.; Ma, Y. H.; Moser, W. R.; Pascucci, M. R. *J. Am. Ceram. Soc.* **1998**, *81*, 1437.
- (138) Ishihara, T.; Furutani, H.; Honda, M.; Yamada, T.; Shibayama, T.; Akbay, T.; Sakai, N.; Yokokawa, H.; Takita, Y. *Chem. Mater.* **1999**, *11*, 2081.
- (139) Cherry, M.; Islam, M. S.; Catlow, C. R. A. *J. Solid State Chem.* **1995**, *138*, 125.
- (140) Minh, N. Q. *J. Am. Ceram. Soc.* **1993**, *76*, 563.
- (141) McCarty, J. C.; Wise, H. *Catal. Today* **1990**, *8*, 231.
- (142) Salomonsson, P.; Griffin, T.; Kasemo, B. *Appl. Catal. A: General* **1993**, *104*, 175.
- (143) Marti, P. E.; Baiker, A. *Catal. Lett.* **1994**, *26*, 71.
- (144) Anderson, H. U. *Solid State Ion.* **1992**, *52*, 33.
- (145) Lewis, G. V.; Catlow, C. R. A. *J. Phys.* **1985**, *6*, 1149.
- (146) Belzner, A.; Gur, T. M.; Huggins, R. A. *Solid State Ion.* **1992**, *57*, 327.
- (147) Carter, S.; Selcuk, A.; Chater, R. J.; Kajda, J.; Kilner, J. A.; Steele, B. C. H. *Solid State Ion.* **1992**, *53–56*, 597.
- (148) Bouwmester, H. J. M.; Burggraaf, A. J. in *Fundamentals of Inorganic Membrane Science and Technology*; Burggraaf, A. J., Cot, L., Eds.; Elsevier: Amsterdam, 1996.
- (149) Islam, M. S. *J. Mater. Chem.* **2000**, *10*, 1027.
- (150) Khan, M. S.; Islam, M. S.; Bates, D. R. *J. Phys. Chem. B* **1998**, *102*, 3099.
- (151) Akashi, T.; Nanko, M.; Maruyama, T.; Shiraishi, Y.; Tanabe, J. *J. Electrochem. Soc.* **1998**, *145*, 2090.
- (152) Norby, T. *Solid State Ion.* **1999**, *125*, 1.
- (153) Shima, D.; Haile, S. M. *Solid State Ion.* **1997**, *97*, 443.
- (154) Guan, J.; Morris, S. E.; Balachandran, U.; Liu, M. *Solid State Ion.* **1998**, *110*, 303.
- (155) Huang, P.; Petric, A. *J. Mater. Chem.* **1995**, *5*, 5.
- (156) Ruiz-Trejo, E.; Kilner, J. A. *Solid State Ion.* **1997**, *97*, 33.
- (157) Balasubramanian, M. R.; Natesan, R.; Rajendran, P. *J. Sci. Ind. Res.* **1984**, *34*, 500.
- (158) Parravano, G. *J. Am. Chem. Soc.* **1953**, *75*, 1497.
- (159) Voorhoeve, R. J. H.; Remeika, J. P.; Trimble, L. E. *Ann. N. Y. Acad. Sci.* **1976**, *272*, 3.
- (160) Chan, K. S.; Ma, J.; Jaenicke, S.; Chuah, G. K. *Appl. Catal. A: General* **1994**, *107*, 201.
- (161) Tilset, B. G.; Fjellvag, H.; Kjekshus, A.; Slagtern, A.; Dahl, I. *Appl. Catal. A: General* **1996**, *147*, 189.
- (162) Tabata, K.; Hirano, Y.; Suzuki, E. *Appl. Catal. A: General* **1998**, *170*, 245.
- (163) Shu, J.; Kaliaguine, S. *Appl. Catal. B: Environmental* **1998**, *16*, L303.
- (164) Wachowski, L. *Z. Phys. Chem. (Leipzig)* **1988**, *269*, 743.
- (165) Tascon, J. M. D.; Tejuca, L. G. *React. Kinet. Catal. Lett.* **1980**, *15*, 185.
- (166) Tascon, J. M. D.; Fierro, J. L. G.; Tejuca, L. G. *Z. Phys. Chem. (Wiesbaden)* **1981**, *124*, 249.
- (167) Falcon, H.; Martínez-Lope, M. J.; Alonso, J. A.; Fierro, J. L. G. *Appl. Catal. B: Environ.* **2000**, *26*, 131.
- (168) Jiang, A.; Peng, Y.; Geo, K. W.; Zhou, P. Y.; Yuan, H. Q.; Deng, J. F. *Catal. Lett.* **1989**, *3*, 235.
- (169) Falcon, H.; Martínez-Lope, M. J.; Alonso, J. A.; Fierro, J. L. G. *Solid State Ion.* **2000**, *131*, 237.
- (170) Libby, W. F. *Science* **1975**, *171*, 499.
- (171) Pedersen, L. A.; Libby, W. F. *Science* **1972**, *176*, 1355.
- (172) Arai, H.; Yamada, T.; Eguchi, K.; Seiyama, T. *Appl. Catal.* **1986**, *26*, 265.
- (173) Baiker, A.; Marti, P. E.; Kreuzsch, P.; Fritsch, E.; Reller, A. *J. Catal.* **1994**, *146*, 268.
- (174) Milt, V. G.; Spetz, R.; Ulla, M. A.; Lombardo, E. A.; Fierro, J. L. G. *Catal. Lett.* **1996**, *42*, 57.
- (175) Saracco, G.; Scibilia, G.; Iannibello, A.; Baldi, G. *Appl. Catal. B: Environ.* **1996**, *6*, 229.
- (176) Zhong, Z.; Chen, K.; Ji, Y.; Yan, Q. *Appl. Catal. A: General* **1987**, *156*, 29.
- (177) Stojanovic, M.; Mims, C. A.; Houdallal, H.; Yang, Y. L.; Jacobson, A. J. *J. Catal.* **1997**, *166*, 324.
- (178) Klvana, D.; Delval, J.; Kirchnerova, J.; Chaouki, J. *Appl. Catal. A: General* **1997**, *165*, 171.
- (179) Martínez-Ortega, F.; Batiot, C.; Barrault, J.; Ganne, M.; Tati-bouet, J. M. *Stud. Surf. Sci. Catal.* **1998**, *119*, 45.
- (180) Marchetti, L.; Forni, L. *Appl. Catal. B: Environ.* **1998**, *15*, 179.
- (181) O'Connell, M.; Noeman, A. K.; Huttermann, C. F.; Morris, M. A. *Catal. Today* **1999**, *47*, 123.
- (182) Song, K. S.; Cui, H. X.; Kim, S. D.; Kang, S. K. *Catal. Today* **1997**, *47*, 155.

- (183) Zwinkels, M. F. M.; Haussner, O.; Menon, P. G.; Jaras, S. G. *Catal. Today* **1999**, 47, 73.
- (184) Saracco, G.; Geobaldo, F.; Baldi, G. *Appl. Catal. B: Environmental* **1999**, 20, 277.
- (185) De, K. S.; Balasubramanian, M. R. *J. Catal.* **1983**, 81, 482.
- (186) Madhok, K. L. *React. Kinet. Catal. Lett.* **1986**, 30, 185.
- (187) Agarwall, D. D.; Goswami, H. S. *React. Kinet. Catal. Lett.* **1994**, 53, 441.
- (188) Arakawa, T.; Ohara, N.; Kurachi, H.; Shiokawa, J. *J. Colloid Interface Sci.* **1985**, 198, 407.
- (189) Shimizu, T. *Appl. Catal. A: General* **1986**, 28, 81.
- (190) Trikalitis, P. N.; Pomonis, P. J. *Appl. Catal. A: General* **1995**, 131, 309.
- (191) Ling, T. R.; Chen, Z. B.; Lee, M. D. *Catal. Today* **1995**, 26, 79.
- (192) Aghabozorg, H. R.; Sakakini, B. H.; Roberts, A. J.; Vickerman, J. C.; Flavell, W. R. *Catal. Lett.* **1996**, 39, 97.
- (193) Sumathi, R.; Johnson, K.; Viswanathan, B.; Varadarajan, T. K. *Appl. Catal. A: General* **1998**, 172, 15.
- (194) Fierro, J. L. G. *Catal. Today* **1990**, 8, 153.
- (195) Ten Elshof, J. E.; Bouwmeester, H. J. M.; Verweij, H. *Appl. Catal. A: General* **1995**, 130, 195.
- (196) Hibino, T.; Sato, T.; Ushiki, K.; Kuwahara, Y. *J. Chem. Soc., Faraday Trans. 1* **1995**, 91, 4419.
- (197) Wang, W.; Lin, Y. S. *J. Membr. Sci.* **1995**, 103, 219.
- (198) Iwahara, H.; Esaka, T.; Uchida, H.; Ogaki, K. *Solid State Ion.* **1981**, 3/4, 359.
- (199) Iwahara, H.; Uchida, H.; Ono, K.; Ogaki, K. *J. Electrochem. Soc.* **1988**, 135, 529.
- (200) Hamakawa, S.; Hibino, T.; Iwahara, H. *J. Electrochem. Soc.* **1994**, 141, 1720.
- (201) Chiang, P. H.; Eng, D.; Tsiakaras, P.; Stoukides, M. *Solid State Ion.* **1995**, 77, 305.
- (202) Marnellos, G.; Sanopoulou, O.; Rizou, A.; Stoukides, M. *Solid State Ion* **1997**, 97, 375.
- (203) Slagtern, A.; Olsbye, U. *Appl. Catal. A: General* **1994**, 110, 99.
- (204) Hayakawa, T.; Andersen, A. G.; Shimizu, M.; Suzuki, K.; Takehira, K. *Catal. Lett.* **1993**, 22, 307.
- (205) Hayakawa, T.; Harihara, H.; Andersen, A. G.; Suzuki, K.; Yasuda, H.; Tsunoda, T.; Hamakawa, S.; York, A. P. E.; Yoon, Y. S.; Shimizu, M.; Takehira, K. *Appl. Catal. A: General* **1997**, 149, 391.
- (206) Yamada, T.; Hiei, Y.; Akbay, T.; Ishihara, T.; Takita, Y. *Solid State Ion.* **1998**, 113, 253.
- (207) Provendier, H.; Petit, C.; Estoumes, C.; Kiennemann, A. *Stud. Surf. Sci. Catal.* **1998**, 119, 741.
- (208) Nam, J. W.; Chae, H.; Lee, S. H.; Jung, H.; Lee, K. Y. *Stud. Surf. Sci. Catal.* **1998**, 119, 843.
- (209) Suzuki, S.; Hayakawa, T.; Hamakawa, S.; Suzuki, K.; Shishido, T.; Takehira, K. *Stud. Surf. Sci. Catal.* **1998**, 119, 783.
- (210) Balachandran, U.; Dusek, J. T.; Sweeney, S. M.; Poeppel, R. B.; Mieville, R. L.; Maiya, P. S.; Kleefisch, M. S.; Pei, S.; Kobylinski, T. P.; Udovich, C. A.; Bose, A. C. *Am. Ceram. Soc. Bull.* **1995**, 75, 71.
- (211) Ma, B.; Balachandran, U.; Park, J. H. *J. Electrochem. Soc.* **1996**, 143, 1736.
- (212) Ma, B.; Hodges, J. P.; Jorgensen, J. D.; Miller, D. J.; Richardson, J. W. Jr.; Balachandran, U. *J. Solid State Chem.* **1998**, 141, 576.
- (213) Tsai, C. Y.; Dixon, A. G.; Moser, W. R.; Ma, Y. H. *AIChE J. Chem. Proc.* **1997**, 43, 2741.
- (214) Gellings, P. J.; Bouwmeester, H. J. M. *Catal. Today* **2000**, 58, 1.
- (215) Jin, W.; Gu, X.; Li, S.; Huang, P.; Xu, N.; Shi, J. *Chem. Eng. Sci.* **2000**, 55, 2617.
- (216) Schwartz, M.; Link, B. F.; Samells, A. F. *J. Electrochem. Soc.* **1993**, 140, L62.
- (217) Samells, A. F.; Schwartz, M.; McKay, R. A.; Barton, T. F.; Peterson, D. R. *Catal. Today* **2000**, 56, 325.
- (218) Hayakawa, T.; Andersen, A. G.; Orita, H.; Shimizu, M.; Takehira, K. *Catal. Lett.* **1992**, 16, 373.
- (219) Yi, G. H.; Hayakawa, T.; Andersen, A. G.; Suzuki, K.; Hamakawa, S.; York, A. P. E.; Shimizu, M.; Takehira, K. *Catal. Lett.* **1996**, 38, 189.
- (220) Dai, H. X.; Ng, C. F.; Au, C. T. *Catal. Lett.* **1999**, 57, 115.
- (221) Kiessling, D.; Schneider, R.; Kraak, P.; Haftendorn, M.; Wendt, G. *Appl. Catal. B: Environ.* **1988**, 19, 143.
- (222) Schneider, R.; Kiessling, D.; Wendt, G.; Burckhardt, W.; Winterstein, G. *Catal. Today* **1999**, 47, 479.
- (223) Swamy, C. S.; Christopher, J. *Catal. Rev.-Sci. Eng.* **1992**, 34, 409.
- (224) Muralidhar, G.; Vijayakumar, K. M.; Swamy, C. S.; Srinivasan, V. *Prepr. 7th Can. Symp. Catal.*; Edmonton: Alberta, 1980; p 289.
- (225) Srinivasan, V.; Swamy, C. S.; Muralidhar, G.; Raj, S. L.; Pitchai, R.; Vijayakumar, K. M. In *New Horizons in Catalysis, Part B*; Seiyama, T., Tanabe, K., Eds.; Kodansha-Elsevier: Tokyo, 1980; p 1458.
- (226) Kameswari, N.; Swamy, C. S. In *Advances in Catalysis Science and Technology*; Rao, T. S. R., Ed.; Wiley: New York, 1985; p 259.
- (227) Gunasekaran, N.; Rajadurai, S.; Carberry, J. J. *Catal. Lett.* **1995**, 35, 373.
- (228) Nakamura, T.; Misono, M.; Yoneda, Y. *Chem. Lett.* **1981**, 1589.
- (229) Ladavos, A. K.; Pomonis, P. J. *J. Chem. Soc., Faraday Trans. 1* **1991**, 87, 3291.
- (230) Armor, J. N. *Appl. Catal. B: Environ.* **1992**, 1, 221.
- (231) Armor, J. N. *Catal. Today* **1995**, 26, 99.
- (232) Iwamoto, M. *Catal. Today* **1996**, 29, 29.
- (233) Shimada, H.; Miyama, S.; Kuroda, H. *Chem. Lett.* **1988**, 1797.
- (234) Teraoka, Y.; Harada, T.; Furukawa, H.; Kagawa, S. *Stud. Surf. Sci. Catal.* **1993**, 75, 2649.
- (235) Yasuda, H.; Mizuno, N.; Misono, M. *J. Chem. Soc., Chem. Commun.* **1990**, 1094.
- (236) Teraoka, Y.; Fukuda, H.; Kagawa, S. *Chem. Lett.* **1990**, 1.
- (237) Happel, J.; Hnatow, M.; Bajars, L. in *Base Metal Oxide Catalysts*; Dekker: New York, 1977; p 117.
- (238) Yasuda, H.; Nitadori, T.; Mizuno, N.; Misono, M. *Bull. Chem. Soc. Jpn.* **1993**, 66, 604.
- (239) Bontchev, R.; Cheshkova, K.; Mehandjiev, D.; Darriet, J. *React. Kinet. Catal. Lett.* **1998**, 63, 121.
- (240) Teraoka, Y.; Harada, T.; Kagawa, S. *J. Chem. Soc. Faraday Trans.* **1998**, 94, 1887.
- (241) Fierro, J. L. G.; de la Banda, J. F. G. *Catal. Rev. Sci. Eng.* **1986**, 28, 265.
- (242) Yokoi, Y.; Uchida, H. *Preprints, J. Am. Chem. Soc., Div. Pet. Chem.* **1997**, 37, 795.
- (243) Belessi, V. C.; Trikalitis, P. N.; Ladavos, A. K.; Bakas, T. V.; Pomonis, P. J. *Appl. Catal. A* **1999**, 177, 53.
- (244) Simonot, L.; Garin, F.; Maire, G. *Appl. Catal. B* **1997**, 11, 181.
- (245) Ocal, M.; Oukaci, R.; Marcelin, G.; Agarwal, S. K. *Ind. Eng. Chem. Res.* **1994**, 33, 2930.
- (246) Barton, J. *Collect. Czech. Chem. Commun.* **1990**, 55, 1935.
- (247) Mizuno, N.; Tanaka, M.; Misono, M. *J. Chem. Soc., Faraday Trans.* **1992**, 88, 91.
- (248) Lindstedt, A.; Strömberg, D.; Abul Milh, M. *Appl. Catal. A* **1994**, 116, 109.
- (249) Shen, S. T.; Weng, H. S. *Ind. Eng. Chem. Res.* **1998**, 37, 2654.
- (250) Skoglundh, M.; Löwendahl, L.; Jansson, K.; Dahl, L.; Nygren, M. *Appl. Catal. B* **1994**, 3, 259.
- (251) Teraoka, Y.; Nii, H.; Kagawa, S.; Jansson, K.; Nygren, M. *J. Mater. Chem.* **1996**, 6, 97.
- (252) Ladavos, A. K.; Pomonis, P. J. *Appl. Catal. B: Environ.* **1992**, 1, 101.
- (253) Ladavos, A. K.; Pomonis, P. J. *Appl. Catal. A: General* **1997**, 165, 73.
- (254) Forni, L.; Oliva, C.; Barzetti, T.; Selli, E.; Ezerets, A. M.; Vishniakov, A. V. *Appl. Catal. B: Environ.* **1997**, 13, 35.
- (255) Peter, S. D.; Garbowski, E.; Guilhaume, N.; Perrichon, V.; Primet, M. *Catal. Lett.* **1998**, 54, 79.
- (256) Harada, T.; Teraoka, Y.; Kagawa, S. *Appl. Surf. Sci.* **1997**, 121/122, 505.
- (257) Ferri, D.; Forni, L.; Dekkers, M. A. P.; Nieuwenhuys, B. E. *Appl. Catal. B: Environ.* **1998**, 16, 339.
- (258) Ward, T. R.; Alemany, P.; Hoffmann, R. *J. Phys. Chem.* **1993**, 97, 7691.
- (259) Peter, S. D.; Garbowski, E.; Perrichon, V.; Primet, M. *Catal. Lett.* **2000**, 70, 27.
- (260) Sorenson, S. C.; Wronkiewicz, J. A.; Sis, L. B.; Wirtz, G. P. *Ceram. Bull.* **1974**, 53, 446.
- (261) Guilhaume, N.; Primet, M. *J. Catal.* **1997**, 165, 197.
- (262) Teraoka, Y.; Nakano, K.; Kagawa, S.; Shangguan, W. F. *Appl. Catal. B: Environ.* **1995**, 5, L181.
- (263) Hong, S. S.; Yang, J. S.; Lee, G. D. *React. Kinet. Catal. Lett.* **1999**, 66, 305.
- (264) Yao, Y. F. Y. *J. Catal.* **1975**, 36, 266.
- (265) Bazes, J. G. I.; Caretto, L. S.; Nobe, K. *Ind. Eng. Chem., Prod. Res. Dev.* **1975**, 14, 264.
- (266) Hibbert, D. B.; Tseung, A. C. C. *J. Chem. Technol. Biotechnol.* **1979**, 29, 713.
- (267) Tanaka, H.; Takahashi, Y.; Kimura, M.; Sobukawa, H. In *Science and Technology in Catalysis*; Kodansha: Tokyo, 1995; p 457.
- (268) Anderson, R. B. *Catalysis*; Emmett, P. H., Ed.; Reinhold: New York, 1956; Vol. 4.
- (269) Vannice, M. A. *Catal. Rev.-Sci. Eng.* **1976**, 14, 153.
- (270) Rofer-de Poorter, C. K. *Chem. Rev.* **1981**, 81, 447.
- (271) Weatherbee, G. D.; Bartholomew, C. H. *J. Catal.* **1984**, 87, 352.
- (272) Fierro, J. L. G. *Catal. Rev.-Sci. Eng.* **1993**, 36, 255.
- (273) Broussard, J. A.; Wade, L. E. *Preprints, Am. Chem. Soc., Div. Fuel Chem.* **1986**, 31, 75.
- (274) Sheffer, G. R.; King, T. S. *J. Catal.* **1989**, 115, 376.
- (275) Brown-Bourzutschky, J. A.; Homs, N.; Bell, A. T. *J. Catal.* **1990**, 124, 52.
- (276) Rojas, M. L.; Fierro, J. L. G.; Tejuca, L. G.; Bell, A. T. *J. Catal.* **1990**, 124, 41.
- (277) Rojas, M. L.; Fierro, J. L. G. *J. Solid State Chem.* **1990**, 89, 299.
- (278) Van Grieken, R.; Peña, J. L.; Lucas, A.; Calleja, G.; Rojas, M. L.; Fierro, J. L. G. *Catal. Lett.* **1990**, 8, 335.
- (279) Klier, K. *Adv. Catal.* **1982**, 31, 243.
- (280) Erdöhelyi, A.; Pasztor, M.; Solymosi, F. *J. Catal.* **1986**, 98, 166.

- (281) Diagne, C. H.; Idriss, H.; Pepin, I.; Hindermann, J. P.; Kienne-mann, A. *Appl. Catal.* **1989**, *50*, 43.
- (282) Watson, P. R.; Somorjai, G. A. *J. Catal.* **1982**, *74*, 282.
- (283) Somorjai, G. A. *Chem. Soc. Rev.* **1984**, *13*, 321.
- (284) Gysling, H. J.; Monnier, J. R.; Apai, G. *J. Catal.* **1987**, *103*, 407.
- (285) Monnier, J. R.; Apai, G. *Preprints, Div. Pet. Chem. Am. Chem. Soc.* **1986**, *31*(2), 239.
- (286) Ichikawa, A.; Fukushima, T. *J. Chem. Soc., Chem. Commun.* **1985**, 321.
- (287) Karwaci, E. J.; Anewalt, N. R.; Brown, D. M. *Preprints, Div. Fuel. Chem. Am. Chem. Soc.* **1984**, *29*, 210.
- (288) Broden, G.; Rhodin, T. N.; Brucker, C.; Brendow, R.; Hurych, Z. *Surf. Sci.* **1976**, *59*, 593.
- (289) Ulla, M. A.; Migone, R. A.; Petuchi, J. O.; Lombardo, E. A. *J. Catal.* **1987**, *105*, 107.
- (290) Weatherbee, G. D.; Bartholomew, C. H. *J. Catal.* **1982**, *77*, 460.
- (291) Ichimura, K.; Inoue, Y.; Kojima, I.; Miyazaki, E.; Yasumori, I. in *New Horizons in Catalysis*; Seiyama, T., Tanabe, K., Eds.; Kodansha-Elsevier: 1981; p 1281.
- (292) Ichimura, K.; Inoue, Y.; Yasumori, I. *Bull. Chem. Soc. Jpn.* **1982**, *55*, 2313.
- (293) Ichimura, K.; Inoue, Y.; Yasumori, I. *Properties and Applications of Perovskite-Type Oxides*; Tejuca, L. G., Fierro, J. L. G., Eds.; Marcel Dekker: New York, 1993; p 235.
- (294) Petunchi, J. O.; Ulla, M. A.; Marcos, J. A.; Lombardo, E. A. *J. Catal.* **1981**, *70*, 356.
- (295) Ulla, M. A.; Lombardo, E. A. *Bull. Chem. Soc. Jpn.* **1982**, *55*, 2311.
- (296) Sinfelt, J. H. *Adv. Catal.* **1973**, *23*, 91.
- (297) Wrighton, M. S.; Ellis, A. B.; Wolczanski, P. T.; Morse, D. L.; Abrahamson, H. B.; Ginley, D. S. *J. Am. Chem. Soc.* **1976**, *98*, 277.
- (298) Kutty, T. R. N.; Avudathai, M. In *Properties and Applications of Perovskite-Type Oxides*; Tejuca, L. G., Fierro, Eds.; Marcel Dekker: New York, 1993; p 307.
- (299) Lehn, J. M.; Sauvage, J. P.; Ziessel, R. *Nouv. J. Chem.* **1980**, *4*, 62.
- (300) Maglizzo, R. S.; Krasna, A. I. *Photochem. Photobiol.* **1983**, *38*, 15.
- (301) Lehn, J. M.; Sauvage, J. P.; Ziessel, R.; Hilaire, L. *Israel J. Chem.* **1982**, *22*, 168.
- (302) Domen, K.; Naito, S.; Onishi, T.; Tamura, K.; Soma, M. *J. Phys. Chem.* **1982**, *86*, 3657.
- (303) Domen, K.; Kudo, A.; Onishi, T.; Kosugi, N.; Kuroda, K. *J. Phys. Chem.* **1986**, *90*, 292.
- (304) Brus, L. E. *J. Phys. Chem.* **1986**, *90*, 2555.
- (305) Thampi, K. R.; Subba Rao, M.; Schwarz, W.; Grätzel, M.; Kiwi, J. J. *Chem. Soc. Faraday Trans. 1* **1988**, *84*, 1703.
- (306) Kudo, A.; Tanaka, A.; Domen, K.; Onishi, T. *J. Catal.* **1988**, *111*, 296.
- (307) Mitsui, C.; Nishiguchi, H.; Fukamachi, K.; Ishihara, T.; Takita, Y. *Chem. Lett.* **1999**, 1327.
- (308) Kudo, A.; Kato, H. *Chem. Phys. Lett.* **2000**, *331*, 373.
- (309) Kudo, A.; Kato, H.; Nakagawa, S. *J. Phys. Chem. B* **2000**, *104*, 571.
- (310) Takata, T.; Tanaka, A.; Hara, M.; Kondo, J. N.; Domen, K. *Stud. Surf. Sci. Catal.* **2000**, *130B*, 1943.
- (311) Trinquier, G.; Hoffman, R. *J. Phys. Chem.* **1984**, *88*, 6696.
- (312) Kim, H. G.; Hwang, D. W.; Kim, J.; Kim, Y. G.; Lee, J. S. *Chem. Commun.* **1999**, 1077.
- (313) Hwang, D. W.; Kim, H. G.; Kim, J.; Cha, K. Y.; Kim, Y. G.; Lee, J. S. *J. Catal.* **2000**, *193*, 40.
- (314) Sato, S.; Kadowaki, T. *J. Catal.* **1987**, *106*, 295.
- (315) van Damme, H.; Hall, W. K. *J. Catal.* **1981**, *69*, 371.
- (316) Miyama, H.; Fujii, N.; Nagac, Y. *Chem. Phys. Lett.* **1980**, *74*, 523.
- (317) Li, Q. S.; Domen, K.; Naito, S. *Chem. Lett.* **1983**, 321.
- (318) Yamazoe, N.; Miura, N. *IEEE Trans. Compon. Packag. Manuf. Technol. Part A* **1995**, *18*, 252.
- (319) Huang, K.; Lee, H. Y.; Goodenough, J. B. *J. Electrochem. Soc.* **1998**, *145*, 3220.
- (320) Señaris-Rodríguez, K. A.; Goodenough, J. B. *J. Solid State Chem.* **1993**, *118*, 323.
- (321) Raccach, P. M.; Goodenough, J. B. *Phys. Rev.* **1967**, *155*, 932.
- (322) Arakawa, T.; Kurachi, H.; Shiokawa, J. *J. Mater. Sci.*, **1985**, *20*, 1207.
- (323) Obayashi, H.; Sakurai, Y.; Gejo, T. *J. Solid State Chem.* **1979**, *17*, 299.
- (324) Rao, C. N. R.; Bhide, B. G. *Am. Inst. Phys. Conf. Proc.* **1974**, *18*, 504.
- (325) Arakawa, T. *Properties and Applications of Perovskite-Type Oxides*; Tejuca, L. G., Fierro, J. L. G., Eds.; Marcel Dekker: New York, 1993; p 361.
- (326) Arakawa, T.; Tsuchi-ya, S.; Shiokawa, J. *Catal.* **1982**, *74*, 317.
- (327) Gaur, K.; Verma, S. C.; Lal, H. B. *J. Mater. Sci.* **1988**, *23*, 1725.
- (328) Arakawa, T.; Tsuchi-ya, S.; Shiokawa, J. *Mater. Res. Bull.* **1981**, *16*, 97.
- (329) Tripathi, A. K.; Lal, H. B. *Mater. Res. Bull.* **1980**, *15*, 233.
- (330) Carotta, M. C.; Martinelli, G.; Sadaoka, Y.; Nunziante, P.; Traversa, E. *Sens. Actuators B* **1998**, *48*, 270.
- (331) Ford Motor Co., *European Patent*, G001-10, 1982.
- (332) Park, K.; Logothetis, E. M. *J. Electrochem. Soc.* **1977**, *124*, 1443.
- (333) Tien, T. Y.; Stadler, N. L.; Gibbons, E. F.; Zacmanidis, P. J. *Am. Ceram. Soc. Bull.* **1975**, *54*, 280.
- (334) Logothetis, E. M.; Park, K.; Meitzler, A. H.; Land, K. R. *Appl. Phys. Lett.* **1975**, *28*, 209.
- (335) Arai, H.; Yu, C.; Fukuyama, Y.; Shimizu, Y.; Seiyama, T. *Proceedings 2nd International Meeting on Chemical Sensors*; Bordeaux, 1986; p 142.
- (336) Yu, C.; Shimizu, Y.; Arai, H. *Chem. Lett.* **1986**, 563.
- (337) Heffler, J.; Bohm, H. *Metallberflache-Angew. Elektrochem.* **1973**, *27*, 77.
- (338) Bockris, J. O'M.; McHardy, J. *J. Electrochem. Soc.* **1973**, *120*, 61.
- (339) Matsumoto, Y.; Yoneyama, H.; Tamura, H. *J. Electroanal. Chem.* **1977**, *80*, 115.
- (340) Matsumoto, Y.; Yoneyama, H.; Tamura, H. *Bull. Chem. Soc. Jpn.* **1978**, *51*, 1927.
- (341) Obayashi, H.; Kudo, T. *Mater. Res. Bull.* **1978**, *13*, 1409.
- (342) Meadowcroft, D. B. *Nature* **1970**, *226*, 847.
- (343) Bockris, J. O'M.; Otagawa, T. *J. Phys. Chem.* **1983**, *87*, 2960.
- (344) Bockris, J. O'M.; Otagawa, T. *J. Electrochem. Soc.* **1984**, *131*, 290.
- (345) Wolf, J. F.; Soled, S. L.; Damjanovic, A. *Extended Abstracts*; Electrochem. Soc. Princeton: New Jersey, 1979; Vol. 79-1, p 893.
- (346) Falcon, H.; Carbonio, R. E. *J. Electroanal. Chem.* **1992**, *339*, 69.
- (347) Falcon, H.; Goeta, A. E.; Punte, G.; Carbonio, R. E. *J. Solid State Chem.* **1997**, *133*, 379.
- (348) Carbonio, R. E.; Fierro, C.; Tryk, D.; Scherson, D.; Yeager, E. *J. Power Sources* **1988**, *22*, 387.
- (349) Latimer *Oxidation States of the Elements and their Potentials in Aqueous Solutions*; Prentice-Hall: New Jersey, 1952; p 44.
- (350) Weston, M.; Metcalfe, I. S. *Solid State Ionics* **1998**, *113-115*, 247.
- (351) Doutsvarzidis, S.; Dimoulas, G.; Tsiakaras, P. *Stud. Surf. Sci. Catal.* **1998**, *119*, 93.
- (352) Tsiakaras, P.; Athanasiou, C.; Marnellos, G.; Stoukidis, M.; ten Elshof, J. E.; Bouwmeester, H. *J. M. Appl. Catal. A: General* **1998**, *169*, 249.
- (353) Sfeir, J.; van Herle, J.; McEvoy, A. J. *J. Eur. Ceram. Soc.* **1999**, *19*, 897.
- (354) Tu, H. Y.; Takeda, Y.; Imanishi, N.; Yamamoto, O. *Solid State Ion.* **1999**, *117*, 277.
- (355) Subbarao, E. C. *Solid Electrolytes and their Applications*; Plenum Press: New York, 1980.
- (356) Stoukides, M. *Ind. Eng. Chem. Res.* **1988**, *27*, 1745.
- (357) Kuo, J. H.; Anderson, H. U.; Sparlin, D. M. *J. Solid State Chem.* **1990**, *87*, 55.
- (358) van Rosmalem, J. *Some Thermodynamic Properties of (Ln, Sr)-MnO_{3±δ} as a cathode material for Solid Oxide Fuel Cells*; Netherlands Energy Research Foundation ECN: Petten, The Netherlands, 1990.
- (359) Feng, M.; Goodenough, J. B.; Huang, K.; Milliken, C. *J. Power Sources* **1996**, *30*, 110.
- (360) Huang, K. Q.; Feng, M.; Goodenough, J. B.; Milliken, C. *J. Electrochem. Soc.* **1997**, *144*, 3650.
- (361) Ishihara, T.; Kudo, T.; Matsuda, H.; Takita, Y. *J. Electrochem. Soc.* **1995**, *142*, 1519.
- (362) Ishihara, T.; Honda, M.; Shibayama, T.; Minami, H.; Nishiguchi, H.; Takita, Y. *J. Electrochem. Soc.* **1998**, *145*, 3177.
- (363) Ishihara, T.; Matsuda, H.; Takita, Y. *J. Am. Chem. Soc.* **1994**, *116*, 3801.
- (364) Huang, P. N.; Petric, A. *J. Electrochem. Soc.* **1996**, *143*, 1644.
- (365) Stevenson, J. W.; Armstrong, T. R.; McCready, D. E.; Pederson, L. R.; Weber, W. J. *J. Electrochem. Soc.* **1997**, *144*, 3613.
- (366) Ishihara, T.; Shibayama, T.; Honda, M.; Nishiguchi, H.; Takita, Y. *J. Electrochem. Soc.* **2000**, *147*, 1332.
- (367) Ishihara, T.; Akbay, T.; Furutani, H.; Takita, Y. *Solid State Ion.* **1998**, *113*, 585.
- (368) Voorhoeve, R. J. H. *Advanced Materials in Catalysis*; Burton, J. J., Garten, R. L., Eds.; Academic Press: New York, 1977; p 129.
- (369) Sazonov, L. A.; Moskvina, Z. V.; Artamonov, E. V. *Kinet. Katal.* **1974**, *15*, 100.
- (370) Clark, A. *The Theory of Adsorption and Catalysis*; Academic Press: New York, 1970; p 360.
- (371) Voorhoeve, R. J. H.; Johnson, D. W. Jr.; Remeika, J. P.; Gallagher, P. K. *Science* **1977**, *195*, 827.
- (372) Shimizu, T. *Chem. Lett.* **1980**, 1.
- (373) Greenwood, N. N.; Earnshaw, A. *Chemistry of the Elements*; Butterworth-Heinemann, Ltd.: Oxford, 1994.

